Modelling exciton dynamics in light-harvesting molecules

by

Leonard Ruocco

M.Phys, The University of Sussex, 2012

A THESIS SUBMITTED IN PARTIAL FULFILLMENT OF THE REQUIREMENTS FOR THE DEGREE OF

DOCTOR OF PHILOSOPHY

in

THE FACULTY OF GRADUATE AND POSTDOCTORAL STUDIES

(Physics)

The University of British Columbia

(Vancouver)

February 2019

The following individuals certify that they have read, and recommend to the Faculty of Graduate and Postdoctoral Studies for acceptance, the dissertation entitled:

Modelling exciton dynamics in light-harvesting molecules

submitted by Leonard Ruocco in partial fulfillment of the requirements for the degree of Doctor of Philosophy

in Physics

Examining Committee:

Prof. Philip Stamp

Supervisor

Prof. Ian Affleck

Supervisory Committee Member

Prof. Gordon Semenoff

Supervisory Committee Member

Prof. Roman Krems

University Examiner

Prof. George Sawatzky

University Examiner

Additional Supervisory Committee Members:

Prof. Robert Kiefl

Supervisory Committee Member

Supervisory Committee Member

Abstract

I investigate the dynamics of multi-state central systems coupled bilinearly to an external oscillator bath within the noninteracting-blip approximation. I focus on both a 3-site configuration, as well as a 2-site model for the central systems of interest. The 2-site model, dubbed the dual-coupling spin-boson (DCSB) model, includes both diagonal and non-diagonal system-bath couplings, whereas the 3-site model considers only diagonal couplings. The bath spectral densities considered in this work include both Ohmic and super-Ohmic forms, as well as single optical phonon peaks. This work is motivated by the recent observance of long-lived quantum coherence effects in the photosynthetic organism known as the Fenna-Matthews-Olson (FMO) complex. The models investigated in this thesis are applied to this system in an attempt to explain its remarkably efficient exciton transfer mechanism, as well as to shed light on the functionality of coherence. The DCSB model is shown to reproduce the rapid exciton transfer times as well as the relatively long coherence times observed in the FMO complex. The non-diagonal system-bath coupling is shown to play a crucial role in this process. This can be attributed to the inelastic phonon-assisted tunnelling (IPAT) mechanism arising from the presence of significant non-diagonal system-bath interactions. Conversely, the 3-site model predicts rapid but incoherent exciton transfer. This can be attributed to the presence of a resonant state in the 3-site architecture, resulting in a relatively slow exciton transfer mode in the system. Therefore efficient exciton transfer requires a careful configuration of the chromophore energy landscape to avoid a resonant 3-site-V configuration. Furthermore, I conclude that coherence effects arising from excitons delocalised across multiple chromophores, promotes IPAT processes arising from non-diagonal system-bath couplings, producing rapid exciton transfer between chromophores. This offers a potential explanation as to the functional role that coherence plays in the energy transfer mechanism of photosynthesis.

Lay summary

A number of landmark experiments in the last decade have suggested that quantum mechanics may be responsible for the remarkably efficient energy transfer in photosynthesis. Theoretical research has ensued hoping to explain the role of quantum mechanics in this process; however, the exact mechanism responsible for these observations remains unexplained. In this thesis I investigate certain mathematical models that could potentially explain this mechanism. I compare the results of these calculations with those determined experimentally on certain photosynthetic organisms. In doing so I manage to closely reproduce the observed coherence times with a model that incorporates critical physical features that, as of yet, have not been applied to the photosynthesis theoretical modelling process. Nature has managed to produce remarkably efficient light harvesting organisms. A better understanding of the underlying mechanisms responsible for this may enable us to harness this knowledge towards the improvement of our own light-capturing technologies.

Preface

This thesis includes both original work, as well as introductory material based upon a summary of the relevant literature. The work presented in Chapters 3, 4 and 5 is original, unpublished work, carried out by the author, Leonard Ruocco, under the guidance of supervisor Prof. Philip Stamp. The work presented in Chapters 4 and 5 is under preparation for publication in the near future.

Contents

List of Tables

List of Figures

Glossary

Antenna complex: A system containing many individual chromophores which acts as the first point of entry for photon absorption in photosynthesis.

Bacteriochlorophyll A (BChla): The principle light harvesting molecule present in green sulfur bacteria. Contains a magnesium atom at its centre, surrounded by 4 nitrogen atoms. A delocalised π-electron spans the entire molecule.

Bath correlation function: Determines how the environment fluctuations affect the central system through the system-environment coupling λ. This tells us how a perturbation of the environment caused by the central system through λ, affects the system at a later time through λ. Fluctuations of the bath coupled to the central system at some time are correlated with fluctuations at some later time.

Boson: A particle with integer spin that obeys Bose-Einstein statistics, so there is no restriction of the number of them occupying the same quantum state.

Coherence: Describes a degree of correlation between physical quantities of a single wave, or between several waves. In in the context of wave mechanics, and by extension the wave-like aspect to quantum mechanics, coherence describes the constructive interference of waves (wavefunctions). Therefore coherence depends on the relative phase of the two waves. Temporal/spatial coherence describes the correlation beween waves observed at different moments in time/points in space. Therefore coherence between energy states in a quantum mechanical system describes the overlap of the wavefunctions corresponding to each state. A particle tunnelling coherently between states is said to be 'delocalised' across the states involved in the tunnelling process.

Central system: In the language of open quantum systems, the central system describes the system of interest. It usually contains only a few degrees of freedom

compared to its environment which contains many. We are usually interested in observing physical quantities pertaining to the central system under the influence of its environment. Therefore the variables pertaining to the environment are 'integrated out', leaving our dynamical equations in terms of variables corresponding to the central system only.

Chromophore: A light-absorbing-conjugated molecule that contains extended π-orbitals, the energy difference of which falls within the visible spectrum. Often interchanged with 'pigment'.

Cut-off frequency ω_c: A high frequency mode of the bath that regularises the bath spectral density to negligibly small values for $\omega \gg \omega_c$. This fixes the ultra-violet divergences present in power-law spectral densities and represents a physical limit to the frequency of bath fluctuations.

Dark state: A term coined in quantum optics, a dark state, represents an atom or molecule that cannot absorb or emit photons. In the molecular context, a dark-state represents an eigenstate of a molecular system (or interacting molecules), that doesn't couple to any external bath. Therefore an exciton that occupies the dark-state will remain 'trapped'. The external bath does not 'see' the dark-state, as it does not couple to it, and therefore offers the exciton no means of leaving that state within the system.

Decoherence: The loss of quantum coherence from a central system of interest due to interactions with an external environment. In the language of quantum measurement theory, decoherence represents the process of wavefunction collapse within the central system due to measurements made by an external environment.

Density matrix: A quantum mechanical operator, or matrix, that describes the statistical state of a system. The density matrix is capable of describing a statistical mixture of states whereas the quantum mechanical state vector can only describe a 'pure state' with no mixture. Mixed states arise in situations where the experimenter does not know which particular states are being manipulated. Therefore the density matrix contains information regarding superpositions of states and therefore quantum mechanical coherences. The diagonal elements of the density matrix represent the probability of finding the system in a particular state, and are therefore dubbed the 'populations'. The off-diagonal elements on the other hand contain

information regarding interference effects and are correspondingly dubbed 'coherences'. A particularly illuminating form for the density matrix comes by way of the path-integral formalism of quantum mechanics. In this case the density matrix represents two independent paths including possible interference effects between them. Therefore the diagonal elements represent both paths starting and ending in the same state, whereas the off-diagonal elements represent different endpoints of the paths and therefore superpositions between states.

Diagonal coupling: A system-environment interaction that couples the environment to the diagonal elements of the Hamiltonian. Therefore the diagonal coupling corresponds to fluctuations in the on-site (or kinetic energies) of the central system. Often referred to as 'local' coupling due to the environment coupling to quantities pertaining to individual states in the system..

Dimer: A molecular aggregate containing two constituent molecules, one acting as the 'donor' and the other the 'acceptor'.

Direct-Coulomb interaction: A pair interaction term in the Hamiltonian. It describes the classical Coulomb interaction between charge densities due to electrons occupying orbitals on different molecules. For the long range Coulomb interaction, the point-dipole approximation is invoked which results in the dipole-dipole approximation of pair interactions. In molecular transport theory, retention of only this potential term in the Hamiltonian results in Förster theory.

Donor/acceptor molecules: A donor molecule represents the point of entry of an exciton to the system. The acceptor molecule, coupled to the donor, represents the additional state in the two-level system that the exciton can tunnel to.

Dual-coupling-spin-boson model (DCSB): An extension to the well known Spin-boson (SB) model that includes both diagonal and non-diagonal system-bath couplings. The SB model only includes diagonal couplings.

Environment (bath): The environment surrounding the central system of interest, usually composed of a very large number of degrees (d.o.f) of freedom with respect to the central system d.o.f. When coupled to the central system, the bath d.o.f influence the dynamics, and quantum properties like coherence, of the central system d.o.f. Usually one is concerned with the time-evolution of the central system d.o.f only, so the bath d.o.f are 'integrated out'.

Exciton: A bound state of an electron-hole pair. The electron and hole interact via the Coulmomb interaction forming a charge-neutral quasiparticle that has less energy than the unbound electron and hole. Exciton's can be highly delocalised due to the screening force of surrounding electrons. However, in amorphous biosystems, exciton delocalisation is suppressed due to disorder by way of Anderson localisation.

Exchange interaction: A pair interaction term in the Hamiltonian that includes an appreciable overlap of neighbouring molecular wavefunctions. Inclusion of this term permits inelastic tunnelling processes involving particle exchange. Unlike the direct-Coulomb interaction, this term has no classical analog. With the inclusion of an external bath coupled to the system, this term permits tunnelling processes involving particle exchange with the bath.

Fenna-Matthews-Olson complex: A water-soluble light-harvesting complex that exists in green sulfur bacteria. It is composed of BChla molecules and mediates the energy transfer from light-harvesting chlorosomes in the antenna complex to the reaction center.

Fermion: A half-integer-spin particle that is subject to the Pauli exclusion principle and therefore obeys Fermi-Dirac statistics.

Fermi's Golden Rule (FGR): A formula describing the transition rate from one energy eigenstate of a quantum system to a continuum of energy eigenstates. The formula is derived using time-dependent perturbation theory in the tunnelling matrix element between initial and final states. Therefore it is assumed that the tunnelling time is much longer than the transition time to the continuum which puts the theory in the regime of very strong system-bath coupling.

Förster theory: A molecular theory of energy transport between two chromophores. A donor molecule may transfer an exciton to an acceptor molecule via the direct-Coulomb interaction (dipole-dipole coupling). With the inclusion of spectral broadening to the spectral lineshapes of the donor and acceptor molecule, the equations of motion are derived with use of a FGR approach, treating the exciton tunnelling term as a perturbation. Förster theory therefore describes incoherent hopping of an exciton between chromophores.

Green sulfur bacteria: Photosynthetic organisms that contain the FMO complex as part of their light-harvesting mechanism. They can be found living in the low-

est light intensity regions of any known photosynthetic organism and exhibit a remarkably efficient energy transfer process, from the point of photon capture to photochemsitry.

Green's function: See *Propagator*.

Hamiltonian: A quantum mechanical operator, or matrix, corresponding to the total energy of the system.

Highest-occupied-molecular orbital (HOMO): A molecular orbital representing the highest energy state of the molecule occupied by an electron.

Ideal-dipole approximation: An approximation valid when the wavelength associated with the energy of the dipole is much larger than the size of the atom. Therefore the dipole is considered to be a point in space.

Inelastic scattering process: A scattering process in which the kinetic energy of a particle is not conserved. The energy can be lost or increased by exchange with its environment.

Instanton: A semi-classical solution to the equations of motion regarding tunnelling between potential wells. In the path integral formalism, the instanton solution describes instantaneous jumps between potential wells, hence the name.

Light-harvesting complex/molecule (LHC): A photosynthetic complex of subunit proteins that may be part of a larger supercomplex. A LHC therefore forms part of the functional process of photosynthesis. They contain a number of chromophores, used to capture a photon of light and/or shuttle an exciton through the complex to the next part of the photosynthesis process.

Localisation: The process by which an atomic or molecular wavefunction is confined to the atom or molecule due to wavefunction collapse. This is the opposite of the delocalised limit where a wavefunction spans several or more atoms or molecules and retains coherence effects. Localisation therefore reflects the incoherent limit of particle hopping.

Lowest-unoccupied-molecular orbital (LUMO): A molecular orbital representing the lowest energy state of the molecule's excited states. The LUMO state is unoccupied in the ground state of the molecule, and occupied by an electron in the 1st-excited state.

Markovian approximation: An approximation used to simplify the equations of motion for an open quantum system. It assumes that the correlation time of the bath dynamics is much smaller than the characteristic timescale of central system dynamics. Therefore 'memory effects' induced by the bath are neglected. In other words a bath mode excited by the central system immediately relaxes to its ground state, from the perspective of the central system, and does not affect the central system dynamics at a later time.

Monomer: A single molecule that is classified in this way as it can undergo 'polymerisation' in certain circumstances leading to polymer formation involving multiple monomers.

Non-diagonal coupling: A system-environment interaction that couples the environment to the off-diagonal elements of the central system Hamiltonian. Therefore fluctuations in the environment modulate the tunnelling matrix elements (potential energy terms/transfer integrals) of the central system. Often referred to as 'nonlocal' coupling due to the environment coupling to quantities pertaining to transitions between states in the system.

Non-interacting-blip approximation (NIBA): An approximation used to simplify the equations of motion (e.o.m) of a central system interacting with its environment (bath). A general e.o.m will include bath correlations that extend to $t \to \infty$. In a diagrammatic language this means that all higher order system-bath interaction diagrams as well as bath-bath interaction diagrams are considered. NIBA uses the assumption that the system spends vastly more time in diagonal states of the reduced density matrix for the system, than off-diagonal states. In a path integral language, it permits the system to spend one 'time block' in an off-diagonal state before returning to a diagonal state. In a diagrammatric language NIBA retains only the self-interaction term of the bath correlation function and excludes any higher order bath-bath interaction diagrams. The approximation also retains the system-bath interaction diagram pertaining to neighbouring interactions only. Since these diagrams are exponentiated in the propagator describing the central system dynamics, they are still considered to all orders in the system-bath coupling energy. Therefore NIBA represents a non-perturbative, quasi-coherent limit to the dynamics of the system.

Ohmic/super-Ohmic/Optical phonon spectral density: Ohmic and super-Ohmic de-

scribe algebraic frequency dependence of the spectral density with linear order and powers higher than one respectively. A regularisation function with a high-frequency cut-off is required to avoid the ultraviolet divergences. An optical spectral density represents a peak in the profile. The peak is centered around a particular frequency and therefore represents a collection of bath excitations with just one frequency. Hence the application to optical phonon spectral densities.

On-site (bias) energy ϵ: The kinetic energy term in the Hamiltonian. For interacting molecules in the two-state limit, the on-site energy represents the energy difference between the two molecules LUMOs, which form the basis for the interacting system.

Open quantum system: A global quantum system that involves some 'central system' of 'interest', and a classical or quantum environment that may be coupled to the central system.

Oscillator bath: An environment (bath) surrounding a central system, comprised of a large number of simple-harmonic oscillators.

Path-integral: An alternative to the classical single trajectory of a system. Instead the trajectory involves a sum, or functional integral, over an infinite number of possible trajectories permitted by quantum mechanics.

Perturbation theory: An approximate solution to a system where the full, complex, system has a small quantity relative to other comparable quantities. The small quantity is considered separately first, with the remaining part of the system containing a known solution. Then the small quantity is reintroduced, and the approximate solution to the full problem is calculated using the fact that correction is a 'perturbation' from the known solution.

π-bond/π-electron: A covalent bond where two 'lobes' of an orbital on one atom is shared with two lobes on another atom. π-bonds tend to be much weaker than other covalent bonds and can result in a delocalised π-electron across the molecule.

Pigment: See *Chromophore*

Phonon: acoustic: An 'in-phase' collective motion of atoms out of their equilibrium position. Acoustic phonons exhibit a linear relationship between frequency and phonon wavevector for long wavelengths which tends to zero for the longest wavelengths; the limit relevant to amorphous materials.

Phonon: optical: An 'out-of-phase' collective movement of atoms where one atom moves in the opposite direction to its neighbour. Optical phonons show no dispersion, and therefore constant energy, in the long-wavelength limit which is the limit relevant to amorphous materials. In molecular theory, optical phonons interacting with a molecule, usually come from intramolecular bonds. For e.g. BChla molecules contain a Carbon-Carbon bond that oscillates within the optical range and couples strongly to delocalised π-electron over the molecule.

Phonon-assisted tunnelling (PAT): A tunnelling process that is assisted by interactions with phonons in the environment. PAT is usually characterised as elastic or inelastic phonon-assisted tunnelling. Elastic PAT results from only diagonal system-bath couplings in a certain parameter space where the tunnelling rate is facilitated by the bath. Inelastic PAT arises from non-diagonal system-bath couplings which permits a tunnelling process via phonon exchange.

Polaron: A quasi-particle formed from an electron and phonon 'cloud'. As an electron moves through a solid, it displaces the atoms around it from their equilibrium positions, dragging them along with it. This results in a bound state of the electron-phonon cloud, lowering the energy compared to the non-interacting system.

Propagator: A function that specifies the probability amplitude of a particle to go from one state to another. State in this case is purely general and could describe anything from position to abstract energy eigenstates. Propagators in the context of quantum field theory are often referred to as Green's functions.

Quantum beating signal: Time-dependent oscillations in the cross-peak correlations measured using 2D-spectroscopy. Quantum beating signals are interpreted as measuring coherence in a system.

Quantum master equations (QME): A completely general QME simply represents the dynamics of the density matrix as opposed to just a quantum state vector. This way coherences, as well as site populations, can be tracked over time. The term QME are often however used interchangeably with Lindblad, or Redfield, equations and therefore represents a restricted class of equations subject to the secular and Markovian approximations.

Reaction center (RC): A sub unit of the photosynthesis mechanism of Green sulfur bacteria. It is situated after the FMO complex, harvesting the exciton to create a charge separation. This provides the energy required for the photochemistry pertaining to photosynthesis. The RC therefore represents the target destination of the exciton.

Redfield equation: An approximate QME that utilises the Markovian and secular approximations.

Relaxation time: The timescale associated with the inverse of a decay rate. The pure relaxation time refers to the inverse of the decay rate out of the high-energy state to the lower-energy state. Dephasing time is the timescale associated with the decay rate of oscillatory terms in the exciton dynamics.

Reorganisation energy: The energy associated with the bath reconfiguration back to equilibrium. This is a measurable quantity in many cases, and is the energy emitted by the bath upon relaxing to its ground state after excitation due to interaction with an exciton.

Resonance/exciton-energy transfer (RET/EET): A process describing energy, or exciton, transfer from one (donor) molecule to an (acceptor) molecule in biological light-harvestin complexes.

Resonant states: A condition when two energy eigenstates are equal.

Secular approximation: An approximation to the dynamics of a central system in which rapidly oscillating terms in the Markovian quantum master equation are disregarded.

Solvent: The liquid solution that permeates the surrounding regions of the chromophores in photosynthetic organisms. Usually constitutes water and electrolytes giving the solvent dialectic properties.

Spectral broadening: The broadening of an unphysical delta function peak in a spectrum to a physical peak with some finite linewidth. The linewidth comes from interaction processes with external systems, representing an exchange of energy with the environment. A delta function peak is said to be unphysical in principle because a quantum system can never completely isolated from its environment.

At the very least, there will also exist some broadening due to the Heisenberg uncertainty principle.

Spectral density: A function that maps out the system-environment interactions across the range of bath frequencies. It therefore depends on the distribution of bath frequencies, the density of states, and the system-bath interaction energy to each bath mode.

Spin-boson model (SB): A mathematical model that includes a spin-1/2 particle (two-state system) coupled non-perturbatively to an oscillator bath. NIBA is invoked to close the system of equations of motion and achieve results in various limits, and for various bath spectral densities. The spin-boson mode is valid in large regions of the parameter space due to the non-perturbative path-integral techniques employed. However, for arbitrary system-bath couplings, it can generally be said that the SB model is valid for large bias energies relative to tunnelling energies.

Three-site-V system: A quantum mechanical central system that contains three states, two of which permit tunnelling between them. Configured in a V shape, the upper two sites are non-interacting and no tunnelling can occur between them. The lower site is coupled to a continuum of states, or in the context of quantum optics, a laser field. In either case the lower site can be depleted due to its interaction with an external source.

Transition dipole moment: An electric dipole moment associated with the transition between two states. Molecular orbitals have different charge distributions and thus two orbitals, or states, will have a transition dipole moment associated with them.

Trimer: A molecular aggregate containing three units, each unit containing one or more molecules.

Tunnelling matrix element Δ: A term in the central system Hamiltonian representing a coupling between different states. Often used interchangeably with *transfer integral* or *inter-state coupling*.

Two-dimensional spectroscopy: Correlates excitation and emission energies of a sample as a function of delay time between events. Spectra are plotted as a function of absorption and emission where diagonal peaks represent on-site energies and cross-peaks represent transitions. This essentially measures the Hamiltonian.

The time-dependence of cross-peak rephasing can be observed to measure coherence. This essentially measures the density matrix and the off-diagonal components identified as 'quantum beating signals'.

Chapter 1

Introduction

1.1 Background and motivation

Understanding the role of quantum coherence effects in molecular systems has been the subject of intensive research for a number of decades. The obvious applications to quantum computing [1] and energy-transport mechanisms at the nanoscale [2] have been a primary motivating factor, not to mention the general interest that physicists have in understanding the quantum-to-classical transition. Quantum coherence effects are well understood at the atomic scale, and it is generally accepted that they can manifest at the molecular scale under optimum conditions. However for most systems comprised of a large number of molecules, in contact with a densely packed local environment at physiological temperatures, we expect quantum coherence effects to be absent. The 'hot' and 'messy' environments that characterise many molecular systems involve a large number of rapidly fluctuating degrees of freedom which overall lead to a relatively strong system-environment interaction. These are far from optimal conditions for quantum coherence effects and one would expect molecular wavefunctions to be fairly well localised on each molecule, representing the incoherent regime of energy transport. In other words, the timescale for coherence effects should be relatively short compared to the timescale of dynamics of energy transport and thus coherence effects are not expected to play a significant role in the process. This is indeed the case for systems such as betaine dye molecules [3] and charge transport in trans-polyacetylene [4], which see coherence times of the order of femtoseconds, in line with inter-molecular transfer times. As a result, a classical description of the energy transfer mechanisms usually suffices in such systems and the role of quantum coherence effects can largely be ignored.

A landmark experiment performed by Engel et al. in 2007 [5] reported the discovery of relatively 'long-lived quantum-beating signals' in the prototypical photosynthetic system *Chlorobaculum tepidum* (green sulfur bacteria) at cryogenic temperatures. Other experiments found similar coherence effects in the system *Rhodobacter sphaeroides* [6], also at cryogenic temperatures, and furthermore, subsequent experiments [7, 8] found coherence effects persisted even at physiological temperatures. To this date, the functional role of quantum mechanics in the energy transport process of these particular photosynthetic systems remains unclear [9], and considering the delicate nature of quantum coherence effects at such scales and temperatures, it is a surprising discovery to find the presence of these so-called 'quantum-beating signals' in biomolecules.

It has long been known that certain photosynthetic organisms can harvest sunlight with near perfect efficiency; however, the application of classical energy-transport models has proven unsuccessful at reproducing the observed efficiencies [10, 11, 12, 13, 14]. The question remains, to what degree do quantum effects play a functional role in optimising the photosynthesis process?

Since the publication of the experiments mentioned above, a plethora of theoretical work has ensued aiming to understand these findings. However, the degree to which quantum coherence effects actually facilitate the energy transfer process in photosynthesis remains controversial. Recently a number of theoretical studies have suggested that quantum effects might actually play a key role in optimising the efficiency of energy transfer in biomolecules [15, 16, 17, 18, 19, 20, 21, 22, 23]. Most theoretical work to date has relied upon a number of assumptions that are arguably invalid when it comes to the specific systems of interest: the mathematical models employed have either been perturbative, or assumed incoherent energy transfer dynamics from the outset. Neither are able to predict the relatively long coherence times observed in experiment.

The task of including the full breadth of coherence effects in such a complex system is formidable, and most studies so far have resorted to fairly extreme approximations in order to make the problem tractable. These approximations tend to exclude any possibility of coherent dynamics from the outset, producing models that are ill-equipped to find coherent behaviour. Attempts to go beyond these limiting models have had promising results [24, 25, 26, 27], and the predicted coherence times are now comparable to those seen in experiments. However, much of this progress has so far been facilitated to a greater or lesser extent by numerics, and a rigorous analytical framework of understanding is lacking. While the numerical results are in accordance with observation, the underlying physical mechanisms remain elusive and a deeper analytical understanding is required.

One mathematical model that treats the interaction of a central spin-half system with its environment non-perturbatively is the spin-boson (SB) model. Originally introduced by Emery and Luther [28] to shed light on the Kondo problem, they demonstrated that the phase space of the low-temperature Kondo model can be understood with the use of the equivalent SB model. Caldeira and Leggett [29, 30, 31, 32], as well as a number of contemporaries [33, 34, 35, 36], used the model to study the effects of dissipation in the dynamics of a particle hopping between two states. The model used the influence functional technique developed by Feynman and Vernon [37] to analyse the effects of the environment non-perturbatively on the central two-state system. Functional integral methods were also employed to study a particle tunnelling in a periodic potential interacting with its environment [38].

Quantum coherence effects are retained up to a certain degree in the SB model, and it has been a powerful tool for modelling 2-state systems interacting with their environments. The model has had many applications ranging from quantum computation [39] to condensed matter and solid-state physics [40]. It has also seen some cursory applications to the photosynthesis mechanism [41, 42, 43, 27]. Here, certain 2-level systems with appreciable wavefunction overlap and the appropriate parameters were selected from specific photosynthetic systems. It was also found recently that in a slight extension to the SB model, where certain higher order coherence effects were taken in to account, decoherence times calculated in the system matched those observed experimentally [27].

Such a direct application of the results of the SB model to photosynthesis is of course restricted to just two states interacting with a shared environment. The energy-transport structure in photosynthesis generally involves more than just two sites and the larger, more representative structure, has generally been approached numerically due to its complexity. It has however been argued that for the photosynthetic systems of interest, the full multi-level structure effectively reduces to a 3-site model [44, 45]. Furthermore, exciton wavefunctions in the FMO complex have been shown to be delocalised across two to three molecules at a time [46]. Therefore in the interest of accurately modelling the energy transport mechanism in photosynthesis analytically, we propose the extension of the SB model to three sites for one model of study in this thesis. This will not only model coherent effects analytically in photosynthesis, but will give a more accurate representation of the structure of the photosynthesis mechanism.

Another limiting aspect of the SB model is the fact that it only considers 'diagonal' system-environment couplings. This kind of system-environment interaction couples the environment to the diagonal elements of the central system Hamiltonian only. In other

words, the diagonal interaction induces fluctuations in the potential energy terms of the two-state system, but not the kinetic energy terms, which constitute the non-diagonal components of the Hamiltonian. In the original theoretical treatment of the SB model, it was argued that one can ignore couplings to the non-diagonal-Hamiltonian elements, provided the tunnelling matrix elements–the kinetic energy terms–are small compared to the on-site energies–the potential energies. These non-diagonal couplings were first introduced by Holstein in 1959 [47] in the context of polaron motion within a one-dimensional crystal lattice. Later they would be discussed in the context of the Peierls transition [48] and subsequently in the Su-Schrieffer-Heeger model of polyacetylene [49]. These non-diagonal couplings correspond to transitions in the central system that involve an absorption or emission of a boson from the environment. As the non-diagonal system-environment coupling energy should be proportional to the tunnelling energy [50], one expects these couplings to be relatively small in the limit of small tunnelling energy. Indeed, the limit of large on-site energy to tunnelling energy is also the limit in which the noninteracting-blip approximation—one of the key approximations used to solve the SB model—is valid.

The problem with this heuristic justification for the exclusion of the non-diagonal couplings in the original SB model is that, while the tunnelling energy is indeed small relative to the bias energy, it is not negligibly small. In fact, the SB model is considered such a powerful model because it retains coherence effects (up to a degree), and contributing to this, is a small but significant tunnelling energy. Numerical studies modelling polaron formation on a lattice, with the inclusion of both non-diagonal as well as diagonal couplings, demonstrated how even small values of the non-diagonal coupling strength greatly alter the polaron properties [50]. Experimental evidence for significant non-diagonal exciton-phonon couplings in photosynthetic systems has also surfaced [51]. Despite this, the inclusion of non-diagonal couplings in theoretical modelling of photosynthesis has largely been ignored. As Mahan [52] remarked, the system-environment couplings of this type are usually excluded due to the difficulty of obtaining reliable solutions with them [53].

Some preliminary theoretical work has been done exploring the role that non-diagonal couplings play in photosynthesis [18, 53]. However, in these cases, some fairly limiting assumptions were employed. In [18] each state in the system was assumed to interact only with its own local, and independent, environment–meaning that the possibility of environment induced transitions between states was ignored. For the effects of non-diagonal couplings on coherent dynamics to be truly resolved, one needs to consider a

shared environment between the states in the system, as is done in this work. In [53], a shared environment was included, however a quantum-master-equation approach was used, assuming that the system-environment interaction could be treated perturbatively. A perturbative approach has been argued to be valid for strong diagonal system-bath couplings modelling the residual system-bath interaction for a system transformed into the polaron frame [54]. However, the inclusion of non-diagonal system-bath couplings– which can be much smaller than diagonal couplings–can render this approach invalid. Therefore a non-perturbative approach, even in the polaron transformed frame, is necessary. The importance of non-diagonal couplings in the photosynthesis modelling process is apparent now, however a proper treatment of the system-environment interaction including these couplings is still lacking.

Aside from the general interest that one might have in the inclusion of non-diagonal couplings to the SB model and photosynthesis, the need for such an extension to the model has found applications in other areas too, for example in the modelling of charge transfer in polymeric solar cells (PSC) [55]. Non-diagonal couplings have also been shown to play an important role in charge trasnfer modelling of organic semiconductors [56]. Recent experiments performed on PSC's have found 'ultrafast quantum beating signals' with surprisingly short periods [57] not unlike those found in photosynthesis. It has been suggested that phonon-assisted transfer may be responsible for this, as the tunnelling energies present in the system cannot account for the ultrafast oscillation frequencies alone [58]. Perhaps the same mechanism is responsible for the long-lived coherence effects observed in photosynthesis too?

One major question that arises from all these considerations is: to what degree does coherence play a functional role in exciton transport in biomolecules? While it is desirable to explain the emergence of coherence in photosynthesis, the coherent nature of transport in these systems could be just a coincidence unless a specific functional role is identified. Coherence-enhanced functionality in biological systems has been discussed previously involving constructive interference of exciton pathways through molecules, leading to improved transfer efficiency [59]. However, how these phenomena apply to photosynthesis remains unclear. In this work, the importance of non-diagonal couplings in modelling exciton transfer is demonstrated. Since couplings of this nature arise when there is appreciable exciton wavefunction overlap across neighbouring molecules, the functional role of coherent exciton dynamics is possibly due to this effect. In other words, the propagation of coherent excitons through the system, facilitates the process of phonon-assisted-transport between molecules, greatly improving transport efficiency.

In summary, the original work presented in this thesis primarily constitutes the following: a new analytical model for the photosynthesis mechanism involving a dimer non-perturbatively coupled both diagonally and non-diagonally to an oscillator bath, and a 3-site model non-perturbatively coupled diagonally to an oscillator bath. Both models shed light on important processes present in the photosynthesis mechanism. The dual coupling dimer model, where both diagonal and non-diagonal system-bath couplings are included, reveals the importance of non-diagonal couplings in not only assisting exciton transfer through the system, but also retaining coherence effects at the same time. The 3-site model demonstrates the potential importance of the dark-state in the photosynthesis mechanism. The dark-state is a state intrinsic to the 3-site-V configuration, and the application of this model to the FMO complex reveals this state to have the longest relaxation times in the system.

Relaxation times in both models are found to be comparable to those observed experimentally. The inclusion of non-diagonal couplings is shown to have a particularly strong influence on both the rate of exciton transfer through the system, as well as the coherence of the exciton. Three different spectral densities, that characterise the environment, are used and their effects on exciton dynamics explored. These constitute two low-frequency distributions of the environment oscillator modes: known as Ohmic and super-Ohmic, and one discrete optical mode with spectral broadening. The inclusion of optical phonons in the environment is shown to be especially important for the FMO complex, which exhibits an experimentally determined spectrum with multiple discrete peaks. Both optical and acoustic phonons are shown to aid in exciton transfer through a photosynthetic dimer system. The non-diagonal system-bath coupling is shown to not only decrease exciton transfer times for relatively large coupling strengths, but also introduce a further decoherence mechanism in to the system. However, while the exciton coherence is shown to decrease with increasing non-diagonal coupling, the coherence time remains longer than the exciton transfer time. This indicates that the exciton motion through the dimer remains coherent for its full duration.

An additional novel feature of the present work involves the retention of the on-site energies in modelling the photosynthesis mechanism with a dual coupling approach. The spin-boson model, with diagonal couplings only, is often simplified to the resonant case where the energy difference between the two central system states is zero [33, 60, 61]. Resonant two-level systems, coupled diagonally to the bath, produce a simple, quadratic pole structure to the propagator which is easily dealt with analytically. Dual coupling models for photosynthesis have also looked at the resonant case [53], however the validity

of such a simplification is dubious. The non-diagonal coupling serves to renormalise the on-site energies in the polaron frame, and setting these energies to zero after the polaron transformation trivialises the non-diagonal interaction. In this work, the on-site energy is retained, and the cubic pole structure of the propagator evaluated analytically. The cubic formalism also serves as the solution to the pole structure of the 3-site configuration in this work.

This thesis is organised as follows: the rest of the introduction chapter will introduce the biological system of interest, the FMO complex, and review some of the ways it has been modelled so far. I discuss why they are lacking in their application to photosynthesis and motivate a more advanced approach. Finally I motivate the study of a 3-site system to model the photosynthesis mechanism and discuss the experimental signatures for a dominant 3-site system operating within the larger seven-site system. In Chapter 2 I introduce the mathematical models to be used in later chapters, and the path integral techniques used to analyse their dynamics. In Chapter 3 I analyse first the 'bare' 3-site model i.e. just 3-sites and their respective tunnelling terms, isolated from any environment; and I then incorporate the environment perturbatively. In Chapter 4, I treat the system-environment interaction non-perturbatively, producing my general results for the 3-site-boson model. In Chapter 5 I look at the inclusion of non-diagonal system-bath couplings to a 2-site model. At the end of each results chapter, I apply my results to the case of photosynthesis. This involves identifying the parameters relevant to the respective model and calculating the relevant relaxation times, decay rates and coherent-incoherent phase spaces of the system. In Chapter 6 I summarise my findings, draw some conclusions and suggest avenues of future work. Appended at the end of this thesis is a section on nomenclature. Due to the interdisciplinary nature of this thesis and the many esoteric concepts introduced and referenced later on, an alphabetical list where each term is summarised is included to assist the reader.

1.2 Quantum phenomena in photosynthesis

One of the key motivations of this thesis is to understand the emergence of quantum effects in photosynthetic biological systems. While there have been a number of photosynthetic organisms shown to exhibit quantum effects at the molecular scale, I focus my study on one such organism, namely that of green-sulfur bacteria *Chlorobaculum tepidum*. Green-sulfur bacteria has been extensively studied using state-of-the-art spectroscopy measurements and much is known about its internal energetic structure therefore. It is

also one of the key photosynthetic organisms known to exhibit very high energy-transfer efficiency as well as long-lived quantum coherence effects in certain parts of its exciton transfer pathway.

1.2.1 Light-harvesting molecules

Every photosynthetic organism contains light-harvesting complexes (LHC) comprised of chromophores: light-absorbing molecules attached to a protein structure holding them in place. These molecules typically consist of a small collection of atoms with separations between molecular-orbital energy levels that fall within the visible spectrum [46, 62, 11, 12]. There are various photosynthetic organisms with different structural arrangements; however, the general process starts with the absorption of light by a chromophore in an antenna-like structure consisting of many individual chromophores. In Figure 1.1 one important chromophore—the bacteriochlorophyll A (BChla) molecule—and its molecular arrangement are depicted.

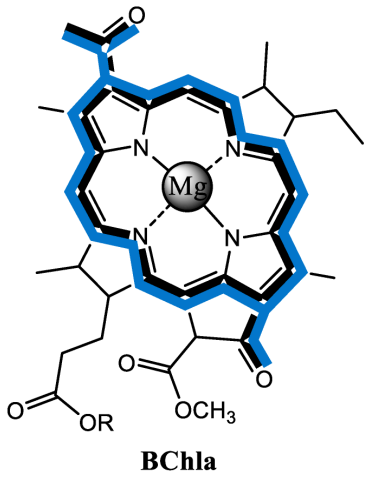

Figure 1.1: Single BChla chlorophyll molecule. Adapted and reprinted with permission from [63]. © 2018 DOAJ

BChla is the principle chlorophyll-type pigment in the majority of photosynthetic bacteria [12]. Spanning around 10Å on its side, it contains a magnesium atom in the center and is surrounded by four nitrogen atoms. An extensive delocalised π-electron system extends over the molecule. The chlorophyll contains two major absorption bands, one in the near ultra-violet region and one in the near infra-red region. These absorption bands come from the molecular transitions within the molecule. Each transition arises due to

different electron density distributions across the molecule, resulting in different dipole moments. In BChla these charge density distributions are primarily governed by the acetyl group at the C-3 position in the molecule, and the single bond in ring B between C-7 and C-8 [12]. This reduces the degree of conjugation as well as the symmetry of the molecule.

The spectra are understood theoretically using a 4-molecular-orbital model. These are made up from the two highest occupied molecular orbitals (HOMOs) and the two lowest unoccupied molecular orbital (LUMOs). While this picture is an approximation of a complex relationship between electronic states and orbital energies, it is generally understood that two dominant transitions arise from these states [12]. Associated with each transition is a transition dipole moment with different strengths. Spectroscopic data of the BChla molecule resolves two fairly dominant peaks for intramolecular transitions corresponding to the HOMO and LUMOs of the molecule and hence form the basis for the 2-state model considered for each chromophore [12, 64].

The photons absorbed in the antennae chromophores create a molecular excitation known as an exciton [65]. The exciton is a bound state created from the transition from one molecular orbital to another; an electron found in the LUMO and an electron hole found in the HOMO, bound together via the Coloumb interaction [66, 67]. After its creation by photon absorption in the antenna complex, the exciton travels through a number of structures, eventually reaching its target destination where it creates a charge separation used for the biochemistry of photosynthesis [11]. This final destination is usually known as the Reaction Center (RC) and the biological structures preceding it serve to 'funnel' the captured photon energy to the RC in as efficient a manner as possible.

Molecular excitons typically have characteristic lifetimes on the order of nanoseconds, after which relaxation to the ground state of the molecule occurs with photon or phonon emission. Associated with each molecular state is a specific electronic density and thus different charge distributions across the molecule. This gives rise to a transition dipole moment that interacts with either the photon of light incident on a LHC or with the dipole moment of a neighbouring chromophore. The chromophore can therefore be modelled as a two-level system and for example, two interacting chromophores would comprise a 4-D Hilbert space with states $|\mathrm{LUMO}\rangle_1, |\mathrm{HOMO}\rangle_1, |\mathrm{LUMO}\rangle_2, |\mathrm{HOMO}\rangle_2$ corresponding to the ground (HOMO) and excited (LUMO) states of chromophores 1 and 2. Typical relaxation times of chromophore excited states (radiative lifetime) are of the order $\tau_{\mathrm{rad}} \sim 10\mathrm{ns}$ whereas inter-chromophore excitation transfer $\tau \sim 10\mathrm{ps}$ happens on the order of picoseconds for BChla molecules in the light harvesting complex LH-2 [68]. Therefore

the ratio $\tau_{\text{rad}}/\tau \gg 1$ tells us that we can exclude the ground states and consider only the interactions between excited states, effectively truncating the Hilbert space to include only the LUMOs of each chromophore.

It turns out that almost every exciton created in the antennae complex by photon absorption eventually makes it to the RC [12]. This is the 'quantum efficiency' usually quoted in the literature pertaining to photosynthesis; the ratio of excitons that reach the RC over the number created by photons. This is simply reflected in the fact that the radiative lifetime (or recombination time) of the exciton τ_{rad} is very large compared to the exciton transfer time. In this sense, we can see that the quantum efficiency of photosynthesis is facilitated by the processes that lead to making the ratio τ_{rad}/τ so large. We will see in this thesis that the presence of non-diagonal couplings is one of the driving mechanisms in reducing the exciton transfer time τ. Perhaps a more meaningful measure of the efficiency of photosynthesis is the percentage of energy absorbed by a photosynthetic organism that is eventually stored in the RC. This number is actually around 27% [12], which is comparatively low compared to the 'near unity quantum efficiencies' quoted in the literature. Therefore the results of this thesis make progress towards explaining the quantum efficiency of photosynthesis more so than the energy efficiency.

1.2.2 The Fenna-Matthews-Olson complex

One such example of an intermediate sub-system that exhibits remarkably efficient exciton transfer in photosynthesis is the Fenna-Matthew-Olson (FMO) complex, named after the researchers who discovered and determined its structure [69]. Forming part of the full light-harvesting infrastructure of *Chlorobaculum tepidum*, it essentially serves as a 'molecular wire', transferring an exciton created by photon absorption in the antenna complex to the RC (see Figure 1.2). The FMO complex has long been known to exhibit near unity exciton transfer efficiency[1] [12] to the RC; however our understanding of exactly how this high efficiency is achieved is lacking.

[1]The 'near unity' quantum efficiency usually quoted in the literature refers to the ratio of photons absorbed to excitons that reach the RC. The amount of energy that reaches the RC compared to that absorbed is actually much lower, reflecting the dissipative effects that happen along the way. This can be anywhere from 30%-50% in the literature [12], however this is still remarkably high and unexplained by the exciton transfer modeling techniques to date.

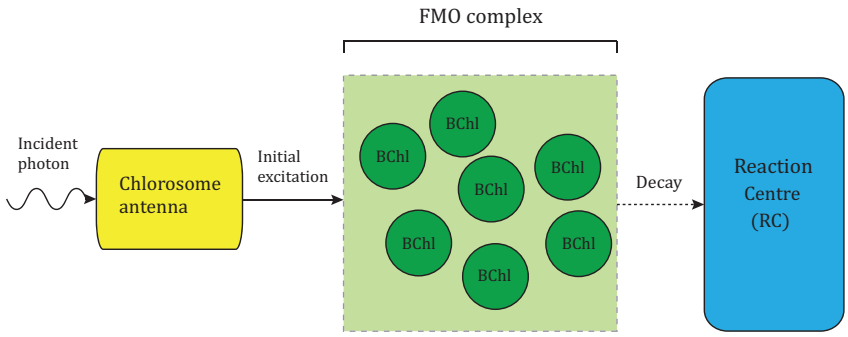

Figure 1.2: Composition of light harvesting systems within *Chlorobaculum tepidum*

The FMO complex consists of a trimer, formed of three identical monomers, each containing seven BChla molecules as depicted in Figure 1.3. An eighth site has recently been identified with energy $\sim 500\text{cm}^{-1}$, which sits close to the antenna complex and possibly acts as the entry point to the system [70].

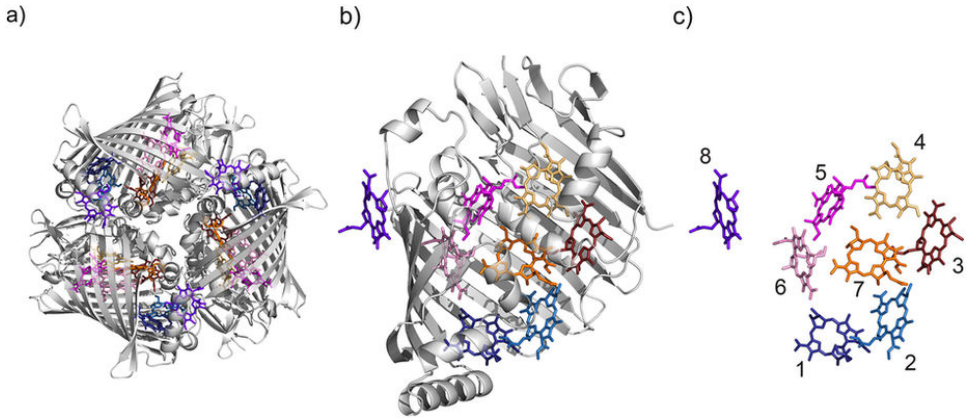

Figure 1.3: Structural depiction of the Fenna-Matthew-Olson complex from *Chlorobaculum tepidum*. (a) Full view of FMO trimer including 3 monomer subunits. (b) Single view of monomer sub unit plus surrounding proteins (grey lines). (c) Single monomer of 8 BChla pigments excluding surrounding protein scaffold. Reprinted with permission from [71].

As the couplings between BChla molecules in neighbouring monomers are negligible compared to couplings between chromophores in the same monomer, exciton transfer is only modelled through an individual monomer [72, 46]. The trimer therefore is considered to contain 3 independent paths of energy transfer to the RC complex.

We see in Figure 1.3 how the eight chromophores in the FMO complex are situated

inside a protein scaffold indicated by the grey lines surrounding the chromophores. This protein structure surrounding the chromophores serves to hold the chromophores at the right distances and orientations for efficient energy transfer [46]. In addition to this local environment of proteins is a surrounding aqueous solvent that permeates the whole structure [73].

It is the FMO complex that was investigated in the landmark 2007 paper by Engel and Fleming [5], which reported on experimental observations of long-lived coherence effects in the exciton transfer pathways. Here, using 2D femtosecond nonlinear spectroscopy, they observed quantum coherence effects in the energy transfer process to persist for ~ 660fs at $T = 77$K [5] and 300fs at $T = 300$K [7, 8].

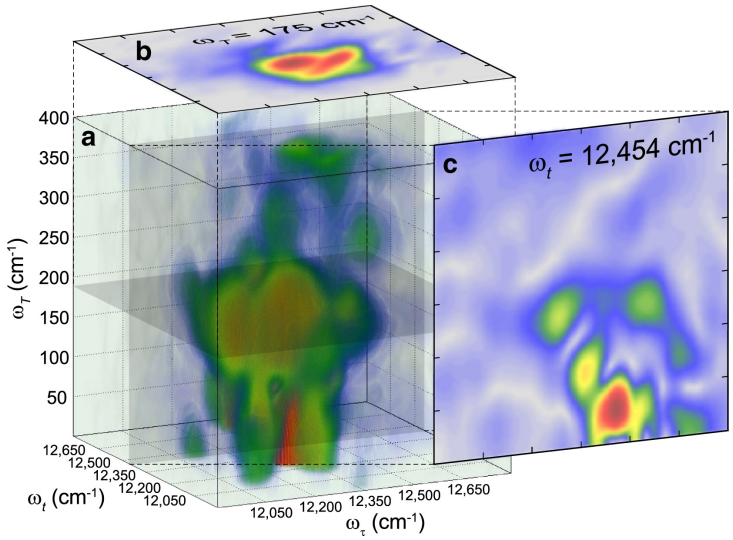

Figure 1.4: Quantum beating signatures for a 77 K FMO 2D spectrum. Axes ω_τ and ω_t represent the Fourier transformed excitation and detection pulses respectively, of a pump and probe laser directed on the FMO sample. The third, vertical axis, ω_T, represents the Fourier transform of the signals evolving over time. The presence of cross-peak frequencies, evolving over time indicates exciton delocalisation across pigments, and thus coherence. Reprinted with permission from [74].

In Figure 1.4 we see an example of 2D spectroscopic FMO data that is interpreted as evidence of coherence in the system. The ω_τ and ω_t axes represent the Fourier transformed excitation and detection pulses respectively, of a pump and probe laser directed on the FMO sample. Frequencies where $\omega_\tau = \omega_t$ are associated with chromophore on-site energies and the cross-peaks $\omega_\tau \neq \omega_t$ represent tunnelling energies in the system. The

plane ω_τ, ω_t therefore maps out the Hamiltonian of the FMO complex. The third axis, ω_T, represents the Fourier transform of the signals evolving over time. Time evolution of the cross-peaks is interpreted as a 'quantum beating' signal and thus evidence of exciton delocalisation across chromophores.

1.3 Microscopic origin of chromophore-environment interactions

The BChla molecules of the FMO complex exist not only in an aqueous solution but are also embedded in a protein scaffold. The effect of this is to shift the excitation energies of the BChla molecules as well as modulate the distance between the molecules. For the solution surrounding the molecule, it is the solvent's dialectric that changes its energy, and for the protein scaffold it is predominantly charged amino acids that interact with the molecule [46]. The interaction of the chromophores with the various parts of their local environment leads to fluctuations of not only the excitation energies, but the couplings between chromophores too. On the one hand, environmental changes induce fluctuating local electric fields that induce a Stark shift in the excitation energies and thus the transition dipoles of the chromophores to fluctuate. This results in the diagonal system-environment coupling. On the other hand, changes in the environment will affect the relative spacing of the chromophores, introducing a fluctuating component to the inter-chromophore couplings. This results in the non-diagonal system-environment coupling.

While most studies to date have focused on the diagonal couplings, a number of recent studies have indicated the importance of including both types of coupling in photosynthesis [75, 76]. While it should be noted that some experiments have found the non-diagonal couplings to be small compared to the diagonal ones [77], it has nonetheless been demonstrated that even small non-diagonal couplings can have a considerable impact on the exciton dynamics [78, 53]. Furthermore, in the study of polaron dynamics, Marchand et al found similarly strong effects arising from non-diagonal couplings to phonons [79, 50].

It is worth remarking at this point that determining the exact size of the system-environment coupling parameters from experiments of the FMO complex is difficult. Analysing spectroscopic data requires complex fitting algorithms based upon models of system-environment interactions [46, 14]. The size of the parameters obtained are highly dependent on the models employed. Furthermore, non-diagonal couplings are usually

excluded from these models meaning that the magnitudes of these couplings are undetermined. This also highlights an issue with the sizes of the diagonal coupling parameters determined to date. If non-diagonal couplings should be present in the models, and the two types of couplings distinguished, then the models that assume only diagonal couplings have presumably determined the size of a composite diagonal and non-diagonal coupling parameter instead.

1.3.1 Diagonal and non-diagonal couplings in chromophores

Two interacting chromophores will have associated with them: excitation energies pertaining to each molecule and tunnelling energies between the molecules. The effect of the environment induces fluctuations in the chromophore's energies, which leads to a dynamical modulation of these parameters. Therefore we can think about two distinct types of system-environment interactions. The first type of interaction is one that modulates the excitation energies of the chromophores. This is known as a 'diagonal' interaction as the environment is coupling to the diagonal elements of the central system's Hamiltonian. The second type of interaction is the 'non-diagonal' interaction, where the environment modulates the tunnelling energies between chromophores. In this section I discuss the microscopic origin of these two types of interaction in the context of biomolecules.

As I discussed in Section 1.2.1, chromophores contain two dominant molecular states: the HOMO and LUMO, which form the basis for their ground and excited states respectively. We recall that the radiative lifetime of the excited (LUMO) state of each chromophore relaxing to their ground (HOMO) state is orders of magnitude smaller than the interchromophore transfer time. Therefore we only consider the interaction of two chromophores' LUMO states. Associated with each chromophores' LUMO states is a dipole moment. If the chromophore's surrounding environment, comprised of a solvent and protein scaffolding, is sufficiently far away, we can treat the chromophore within the dipole approximation. This leads to a central assumption in the Förster picture of energy transfer between chromophores, which we discuss below. Charges present in the chromophore's environment, coming from the surrounding solvent or amino acid residues in proteins, produce an electric field. This leads to a fluctuating energy term for the exciton of the form

$$\Delta E_\alpha = \frac{1}{\epsilon} \sum_j \frac{q_j \vec{\mu}_i \cdot \vec{x}_{ij}}{R_{ij}^3} \tag{1.1}$$

where $\vec{\mu}_i$ is the dipole moment of an exciton on the ith chromophore, ϵ is the optical dialetric constant, R_{ij} the distance from the center of the chromophore to the environmental charge, and x_{ij} is the fluctuation about the equilibrium position of the chromophore. Since the fluctuating energy shift depends on the relative distance between chromophores and amino acid residues, we see how phonon vibrations present in the surrounding protein structure couple to the system as they modulate this distance. In a second quantised language the site displacement operator for the phonon $x_q = \sqrt{\hbar/2M\omega_q}(b_q + b_q^\dagger)$ (see Mahan [52]) gives

$$\Delta E_\alpha = \sum_q \lambda_{\alpha,q}(b_q + b_q^\dagger) \tag{1.2}$$

where α here labels a chromophore and q a phonon mode of the bath. The chromophore-bath coupling $\lambda_{\alpha,q}$, is a function of the charges present in the surrounding medium and is therefore thought of as a backreaction resulting from the polarisation of the environment by the chromophore (see section 2.5.1.2 in [64]). This is the origin of the diagonal couplings.

We now turn to the microscopic origin of the non-diagonal chromophore-environment couplings. Provided the interchromophore spacing is large compared to the width of a chromophore i.e. more than several Angstroms [12], then the exciton transfer between chromophores can be considered a long range dipole-dipole interaction. This leads to the ideal-dipole approximation of molecular interactions often employed in the literature, where non-diagonal couplings can be excluded. If however the interchromophore spacing is such that there exists appreciable wavefunction overlap between molecular orbitals then this approximation breaks down.

Calculations performed using the ideal-dipole approximation of chromophore-chromophore interaction, compared to experiment, demonstrate the failure of the ideal-dipole approximation for BChla molecules [80]. The sizes of the chromophores in this case are ~ 9Å, which is comparable to the inter-chromophore distance determined to be ~ 15Å, which puts the system out of the range of applicability of the ideal dipole approximation.

Wavefunction overlap of neighbouring chromophores contains an exponential dependence on separation distance. Vibrations in the local environment can cause the two chromophores to move closer or further away from each other, thereby modulating the separation distance. For an environment with quantised vibrations, this introduces a process by which an exciton can hop between chromophores by way of an inelastic scattering process [52]. Phonons are not conserved in this case and an exciton can tunnel

between chromophores by absorption or emission of phonons. Since the tunnelling term depends exponentially on separation now due to the molecular wavefunction overlap of the two interacting chromophores, it follows that the tunnelling frequency between donor d and acceptor a molecules Δ_{ad} is modulated by

$$\tilde{\Delta}_{ad} = \Delta_{ad} \exp\left[-\sum_q \frac{F_{ad,q}}{\hbar\omega_q} x_q\right] \tag{1.3}$$

where $F_{ad,q}$ is the force between the two chromophores due to the displacement x_q, and q labels the phonon mode. In a second quantised language the site displacement operator for the phonon position $x_q = \sqrt{\hbar/2M\omega_q}(b_q + b_q^\dagger)$ gives us

$$\tilde{\Delta}_{ad} = \Delta_{ad} \exp\left[-\sum_q \frac{V_q}{\hbar\omega_q}(b_q + b_q^\dagger)\right] \tag{1.4}$$

with V_q representing the product of the force applied by the phonon mode q and the distance between the two chromophores, with ω_q the frequency of phonon mode q, and $b_q, b_q^\dagger$ the destruction/creation operators for the phonons. We can expand this to linear order in $V_q/\hbar\omega_q$, provided the phonons modulate the distance between chromophores only slightly. In this case we have

$$\tilde{\Delta}_{ad} = \Delta_{ad} - \sum_q \lambda_{ad,q}(b_q + b_q^\dagger) \tag{1.5}$$

where the coupling strength $\lambda_{ad,q}$ is now a function of the tunneling matrix element between the donor and acceptor molecules and the phonon frequency. So we see that the phonons modulate the distance between chromophores, thereby modulating the tunneling amplitude. This is the origin of the non-diagonal coupling between chromophores.

1.4 Exciton dynamics in photosynthetic systems: traditional theories and their limitations

I now discuss the conventional theories of excitation energy transfer (EET) that use the molecular parameters described above to obtain rate constants determining dynamics within FMO and associated relaxation effects. There is of course no general theory (yet) that applies across the whole parameter space, but the choice of theory depends on the relative strength of pigment-pigment and pigment-environment couplings.

Traditionally, EET in FMO has been modelled in two limits. One limit, known as Förster theory, considers small chromophore-chromophore couplings Δ compared to chromophore-environment couplings Λ (I define the coupling here to be Λ in anticipation of its relationship to the experimentally determined reorganisation energy of the bath). In this case the exciton is localised on each chromophore and Δ can be treated perturbatively. In the opposite limit, the exciton-bath coupling Λ is treated perturbatively, leading to Redfield theory. Associated with each of these couplings are therefore two separate timescales. One is the inverse of the bath coupling $1/\Lambda$, which describes the timescale over which energy is transferred to the environment. The other is the inverse of the exciton-exciton coupling $1/\Delta$, which describes the timescale of exciton transfer between chromophores. Therefore in the Forster limit $1/\Lambda \ll 1/\Delta$ we have a rapid energy loss to the environment occurring over a timescale much shorter than the inter-chromophore transfer. Conversely in the opposite limit, exciton transfer occurs at a much faster rate than dissipation to the environment.

In the case of FMO the tunnelling energies are of order $\Delta \sim 1$meV corresponding to a transfer time $\tau \sim 4$ps, while reorganisation energies are found to be around $\Lambda \sim 4$meV corresponding to a dissipation time $\tau_\Lambda \sim 1$ps[62]. The reorganisation energy is an experimentally determined value related to the system-bath coupling strength (see Section 2.3) So we see that in FMO the size of these parameters are actually similar and one must therefore go beyond the limiting cases and utilise a non-perturbative theory. It was shown by Sharp et al. [81] as well as Ishizaki et al. [24] that a calculation of the 2D optical spectrum assuming weak coupling to the environment fails to reproduce the oscillations seen by Engel et al. [5]. Therefore the application of these models to date has been arguably inappropriate to the FMO complex, and a non-peturbative analysis such as the one I have employed here is warranted. Nonetheless I briefly summarise some of these traditional methods before discussing the results of my non-perturbative methods and their application to FMO.

1.4.1 Resonance Energy Transfer

First I will describe the process of exciton couplings across different chromophores. This is known as resonance energy transfer (RET) and describes the transfer of energy from one molecule (the Donor) to another (the Acceptor) in biological chromophores. A molecule (or chromophore) is initially excited by a laser pulse in a lab setting or a monochromatic light source in a natural setting, creating an exciton on the first molecule. Splitting the

chromophore coupling into its long and short range components, i.e. dipole-dipole V_c and exchange terms V_{ex} respectively, reads

$$V = V_c + V_{ex}. \tag{1.6}$$

It is assumed in RET that the exciton is transferred between molecules via a dipole-dipole interaction, therefore $V \approx V_c$ where

$$V_c = \frac{1}{4\pi\epsilon_0}\frac{\kappa\mu_D\mu_A}{R^3} \tag{1.7}$$

where $\kappa = \mu_D \cdot \mu_A - 3(\mu_D \cdot R)(\mu_A \cdot R)$ is an orientation factor that reflects the fact that no interaction is observed between perpendicularly oriented chromophores. $\vec{R}$ is the separation vector between the molecule's centres and $\vec{\mu}_d$ and $\vec{\mu}_a$ are the donor and acceptor transition dipole moments respictively. The transition probability is proportional to $|\Delta|^2$ and therefore goes as $1/R^6$. The dipole-dipole interaction expression is obtained from the expansion of the Coulomb interaction in the acceptor-donor distance parameter to get a multipole series, while retaining only the dominant term.

1.4.2 Forster theory

Forster theory presented a key step in the understanding of EET at the molecular scale when it was introduced in the last century [82]. Its applications have had success not only in understanding light-harvesting mechanisms in biochemistry but also in the development of artificial organic-based light-emitting diodes [83]. Its application to the experimental sphere facilitated the development of fluorescence-resonance-energy transfer (FRET) [67], a technique that has been widely used to detail the structure of biological systems. Central to the theory, however, is the approximation of weak inter-chromophores coupling Δ_{da} (between donor and accepter chromophores) compared to environmental couplings γ. Forster therefore derived his EET rate expression with the use of the Fermi-Golden-rule approach, treating Δ as the perturbation in time-dependent perturbation theory. The rate of exciton transfer between donor and acceptor states was derived by Forster [82] to be

$$k_{d\to a} = \Delta_{da}^2 \int \frac{d\omega}{2\pi}\mathrm{Re}\{A_d\}\mathrm{Re}\{F_a\} \tag{1.8}$$

where A_d and F_a are the absorption and fluorescence lineshapes of the donor and acceptor chromophores. The resulting rate expression is expressed as the overlap integral between

the fluorescence spectrum of a donor and the absorption spectrum of an acceptor [84].

The limitations of this approach to modeling EET rest upon some key, rather limiting assumptions. The donor and acceptor molecule must be coupled sufficiently weakly compared to chromophore-bath coupling such that Fermi's Golden Rule applies. This leads to incoherent hopping between donor-acceptor molecules such that the dissipation to the bath is one-way. No feedback to the system from the bath is permitted and the theory excludes possible coherence effects in principle due to the assumption of very strong system-bath coupling relative to the tunnelling energy.

1.4.3 Quantum master equations in molecular systems: the Redfield equation

In the opposite limit to Forster theory, quantum master equations are used to describe exciton dynamics. The fundamental assumptions here are that the exciton-environment coupling is small compared to inter-molecular interactions and so the system-environment coupling is treated perturbatively. The most commonly used version of this approach in the context of biomolecules is the Redfield equation [64, 85]. Master equations have also seen widespread application in the field quantum optics [86].

Derivations of quantum master equations for specific systems usually start from the Liouville equation [87]

$$\partial_t \rho(t) = -\frac{i}{\hbar}[H, \rho] \tag{1.9}$$

where $\rho(t)$ is the time-dependent density matrix of the entire system: central system S plus bath B such that the Hamiltonian is $H = H_S + H_B + H_I$ where H_I is the system-bath interaction. The Liouville equation is essentially the density matrix form of the Schrodinger equation and so allows the time-evolution of a statistical mixture of states. One is generally interested in the dynamics of the central system so we trace over the bath degrees of freedom

$$\rho_S(t) = \mathrm{Tr}_B[\rho(t)]. \tag{1.10}$$

In deriving the Redfield equation one starts from the assumption that the initial system and bath states factorise

$$\rho(0) = \rho_S(0) \otimes \rho_B \tag{1.11}$$

This assumption is valid in the context of exciton dynamics as the creation of the exciton in the system at $t = 0$ is incredibly fast compared to the inverse bath couplings. We recall that in light-harvesting complexes, an exciton is created either by the sudden absorption of light, or the injection of an exciton from the antenna complex. Another key assumption in Redfield theory takes the system-environment coupling to be weak and second-order perturbation theory is used accordingly. In addition to these assumptions is the use of the Markov approximation, which makes the master equation local in time. This latter simplification, it should be noted, removes any possibility for feedback in to the central system from the bath i.e. any energy transfer to the bath is one way and cannot re-enter the central system at a later time. The relevant physical condition for the Markov approximation is when the memory timescale τ_B of the bath is very small compared to the timescale t of the dynamics of the central system. This means that the bath correlation function decays sufficiently during an appreciable timescale over which the central system evolves, removing the possibility for bath memory effects [88]. The resulting Redfield equation is [24]

$$\partial_t \rho_{\alpha\beta}(t) = -i\omega_{\alpha\beta}\rho(t) + \sum_{\alpha',\beta'} R_{\alpha\beta,\alpha'\beta'}\rho_{\alpha'\beta'}(t) \tag{1.12}$$

where $\hbar\omega_{\alpha\beta} = \epsilon_\alpha - \epsilon_\beta$ describes the energy gap between chromophores and the indices α, β run over chromophore sites. The second term describes the relaxation dynamics where the Redfield tensor is given by

$$R_{\alpha\beta,\alpha'\beta'} = \Gamma_{\beta'\beta,\alpha\alpha'} + \Gamma^*_{\alpha'\alpha,\beta\beta'} - \delta_{\beta\beta'}\sum_\mu \Gamma_{\alpha\mu,\mu\alpha'} - \delta_{\alpha\alpha'}\sum_\mu \Gamma^*_{\beta\mu,\mu\beta'} \tag{1.13}$$

The damping terms are given by

$$\Gamma_{\alpha\beta,\alpha'\beta'} = \frac{1}{\hbar^2}\sum_{qq'} \lambda_{\alpha\beta,q}\lambda_{\alpha'\beta',q'}C_{qq'}(\omega_{i'j'}) \tag{1.14}$$

where $\lambda_{\alpha\beta,q} = \langle\alpha|\,\lambda_q\,|\beta\rangle$ are the chromophore-bath couplings. The Fourier transformed bath correlation function is defined as

$$C_{qq'}(\omega) = \int_0^\infty dt e^{i\omega t}C_{qq'}(t) \tag{1.15}$$

where the time-domain correlation function is

$$C_{qq'}(t) = \frac{\hbar}{\pi}\int_{\infty}^{\infty} d\omega J_{qq'}(\omega)[n(\omega)+1]e^{-i\omega t} \tag{1.16}$$

and $n(\omega) = 1/(e^{\beta\hbar\omega}-1)$ is the Bose-Einstein distribution function and $J_{qq'}(\omega)$ the spectral density of the bath (see Section 2.3). An additional approximation applied to equation 1.12, which casts it in the quantum master equation form commonly used in the literature [88, 64], is known as the secular approximation. This amounts to neglecting the rapidly oscillating terms that contain $e^{i(\omega_i-\omega_{i'})}$, which effectively amounts to a Rotating Wave approximation. This is generally justified under the Riemann-Lebesgue-Lemma that states that the integral of a rapidly oscillating function goes to zero in the limit when in this case $\omega_i - \omega_{i'} \to \infty$.

Along with the fundamental assumption that the system-bath interaction is perturbative to second order, we see that the Redfield equation describes a fairly restricted class of systems. Despite the popularity of quantum master equation approaches to modelling photosynthesis [15, 23, 16, 17], a number of studies have shown explicitly the failure of this approach [24, 84, 89] in the context of photosynthesis.

There have been some attempts to go beyond the traditional theories described however, often these changes have involved small deviations from the master equations models [21, 84]. In this case non-Markovian effects are reintroduced, however the system-bath coupling is still treated perturbatively. Some analytical studies on photosynthetic systems have utilised non-perturbative methods. The spin-boson model, with just diagonal system-bath couplings, was applied to the FMO complex and found persistent oscillations in the exciton dynamics in accordance with the experimentally determined values [27]. However, this model assumes a relatively large tunnelling energy between chromophores which can account for the predicted rapid exciton transfer rates. Furthermore, the model assumes just an Ohmic form for the bath spectral density in order to utilise the results from the spin-boson literature. Despite these limitations the initial success of utilising non-perturbative methods in studying the FMO system is promising.

In the next chapter, I set up the path-integral approach to analysing exciton dynamics. In subsequent chapters, this will be used to model the FMO system in photosynthesis with the intention of accurately predicting relaxation rates compared to experiment as well as providing a better understanding of the underlying physics.

1.5 3-site configurations in the Fenna-Matthew-Olson complex

I now turn to the motivation behind studying a 3-site model in the context of photosynthesis in more detail. I begin with some preliminary, qualitative considerations: looking at the energy structure of the FMO system and how the branched nature of the system leads to an intuitive 3-site reduced model. I also look at some spectroscopic data, which has hinted at the presence of a dominant 3-site structure in the system. While there have been a number of studies investigating a 3-site-ladder model for the FMO complex [44, 90], where the site energies are therefore different, here we focus on the 3-site-V configurations [45].

To see how a 3-site-V configuration can be effective at modelling the dynamics of the full FMO system, we first look at the on-site energies and transition matrix elements between sites (dipole-dipole couplings between chromophores), established from spectroscopic data [46].

$$H_{FMO} = \begin{pmatrix} 26.7 & -12.9 & 0.6 & -0.5 & 4.7 & -0.58 & -1.0 \\ -13.0 & 27.3 & 4.0 & 0.9 & 0.7 & 1.0 & 0.1 \\ 0.6 & 4.0 & 0 & -5.8 & 0.12 & -1.0 & 0.63 \\ -0.5 & 0.9 & -5.8 & 15.5 & -8.8 & -1.8 & -7.6 \\ 0.58 & 0.7 & 0.12 & -8.8 & 55.8 & 89.7 & -2.5 \\ -15.1 & 8.3 & -8.1 & -14.7 & 11.1 & 41 & 4.1 \\ -1.0 & 0.1 & 0.63 & -7.6 & -0.31 & 4.1 & 34.7 \end{pmatrix} \text{(meV)} \tag{1.17}$$

In Figure 1.5 we see a pictorial representation of the FMO Hamiltonian equation 1.17, including only dominant couplings greater than 3.7meV.

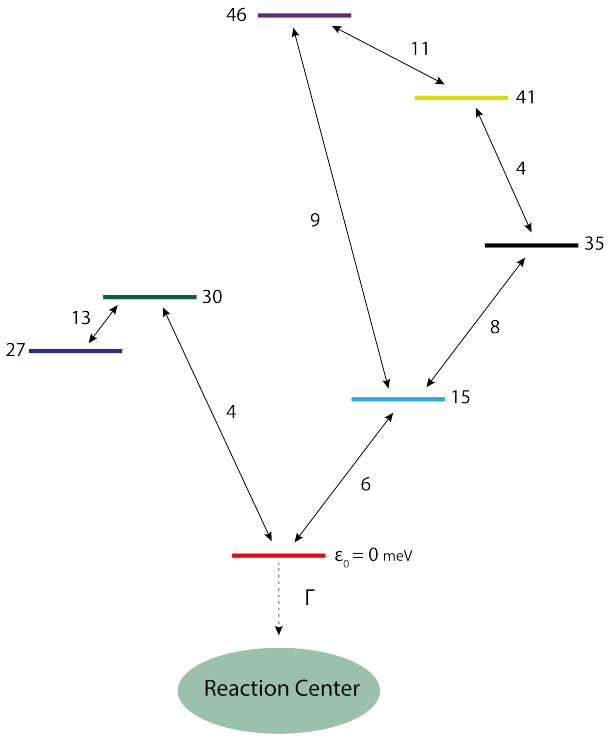

Figure 1.5: Pictorial representation of Hamiltonian for FMO complex, taken from spectroscopic studies [46], in units of meV. Coloured lines indicate excitation energies of different chromophores (diagonal Hamiltonian entries). Arrows indicate inter-chromophore couplings (off-diagonal Hamiltonian entries). Numbers included next to lines and arrows indicate the associated energy with that excitation energy of coupling respectively. Only dominant energy transfer pathways included; couplings > 4meV

Having only included dominant energy transfer pathways above 4meV we hope to demonstrate the branched nature of the system. It's clear that there are two dominant branches in the system with relatively small tunnelling energies between them. One connects states $|1\rangle \leftrightarrow |2\rangle \leftrightarrow |3\rangle$ and the other connects states $|3\rangle \leftrightarrow |4\rangle \leftrightarrow |5\rangle \leftrightarrow |6\rangle \leftrightarrow |7\rangle$. If the states that comprise the excited state portion of each branch can be described by a single 'effective' state, with some correponding 'effective' tunneling energy with the ground state at $|3\rangle$, then the remaining system would be of the 3-site-V form depicted in Figure 1.6.

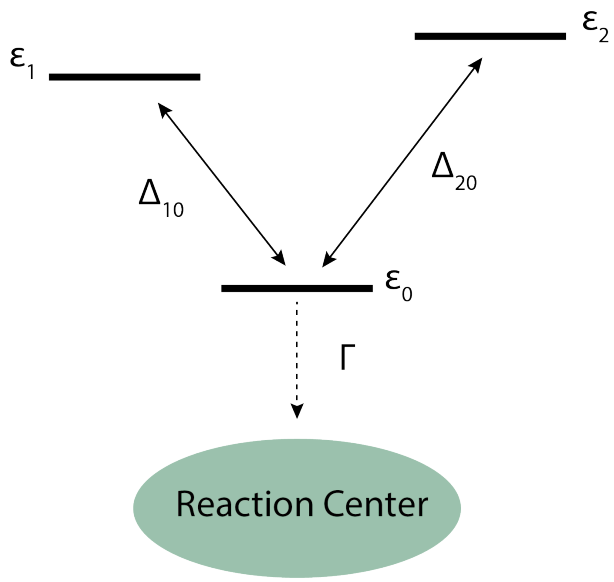

Figure 1.6: Effective 3-site-V configuration for FMO complex.

Schmidt and Renger, in fact, demonstrated that there is no qualitative difference in the site-population dyamics between the full FMO Hamiltonian and an 'effective' 3-site model [90].

After some qualitative considerations of the possible 3-site nature of the FMO system, I look now at some spectroscopic data suggestive of a dominant 3-site structure in FMO. The energy spacing of excitonic levels is relatively small compared to the inhomogenous broadening present in the optical transitions, so much so that the resulting linear absorption spectrum is almost entirely featureless at physiological temperatures [91]. At cryogenic temperatures of $\sim 77K$ however, 3 distinct peaks emerge in the spectra of FMO. Simulations performed in the literature [46, 91, 71] suggest exciton delocalisation across combinations of 2-3 chromophores in FMO. If coherence effects are to play a role in efficient energy transfer in the FMO complex, then it is across at most three chromophores that this effect will be present. Beyond that the system presumably evolves according to the Forster limit corresponding to incoherent hopping between chromophores. The various 3-chromophore delocalisation configurations are shown in Figure 1.7. Here we see the results of experimental spectroscopic data on FMO showing the emergence of three distinct peaks at cryogenic temperatures. We also see the extent of wavefunction delocalisation across the various chromophores.

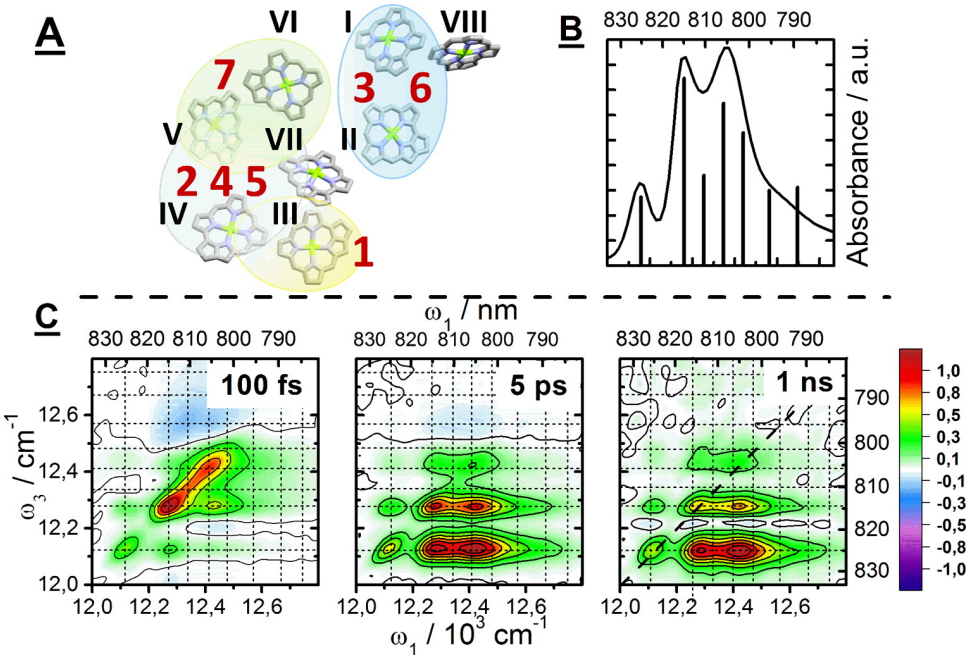

Figure 1.7: (A) Arrangement of BChla pigments within the FMO units. BChla site numbering according to Fenna is in black Roman numerals. Schematic representation of spatial extent of the excitons according to Adolphs et al. [46] is shown by shaded areas. Exciton numbering (red numbers) is given in order of increasing energy. (B) Linear absorption spectrum of FMO at 77 K with excitonic transitions (vide infra) represented by vertical bars. (C) Normalized absorptive 2D spectra at increasing population delays with dashed lines indicating excitonic transition energies. All spectra were recorded in 1:2 aqueous buffer:glycerol mixture at 77 K. Reprinted with permission from [91].

The central 3-site-V system parameters to be used in our analysis we take from [46], where the electronic energies and couplings between them were determined from a time-dependent density functional theory (DFT) on the chromophores with an electrostatic Poisson-Boltzmann type calculation. Similar studies have also used a DFT approach to determine the chlorophyll energies immersed in organic solvents to great effect, comparing their results to experimentally observed spectra [92]. The calculated diagonal site energies and tunneling terms in [46] are shown in Table 1.1.

BChl site	On-site energy (meV)	BChl-BChl transition	Tunneling (meV)
Ground state: $\|0\rangle$	0	$\|0\rangle \rightarrow \|1\rangle$	1.8
Site 1: $\|1\rangle$	20	$\|0\rangle \rightarrow \|2\rangle$	3.2
Site 2: $\|2\rangle$	20		

Table 1.1: Tuned V-system parameters. From Adolphs et al [46]

We see in Table 1.1 how the on-site energies are large compared to the tunnelling energies, putting us within the strong-localisation region. Just based upon these numbers one would expect the wavefunctions of each chromophore to be fairly-well localised around their respective BChla molecules, with possibly some delocalisation spreading out to neighbouring chromophores. This is somewhat in line with the data presented in Figure 1.7, however there is clearly still some delocalisation across chromophores.

Chapter 2

A path-integral approach to exciton transfer

In this chapter, I set up the 3-site model in a path-integral formalism. While I will primarily focus on the 3-site application here, the resulting formalism will be applicable to the 2-site model used in Chapter 5 with the appropriate modifications. Indeed, the 2-site path integral formalism has been described extensively in the literature and so in this chapter I will focus on the extensions of the 2-site formalism to the 3-site case.

While my final results will be non-perturbative in the system-bath coupling, the auxiliary approximations made along the way will build upon a number of techniques employed in the famous spin-boson model. The spin-boson model [31], considered a spin-1/2 system coupled to an oscillator bath, developed in the path integral formalism along with the noninteracting-blip approximation (NIBA). While this approach is fully non-perturbative in the system-bath coupling, and permits memory effects in the system, the underlying approximation restricts the longevity of coherences in the central system. My 3-site-boson model will involve an extension to this model, by way of the addition of not only a third site to the system but an extra tunnelling matrix element. Although this extended mathematical model will also share many of the varied applications that the spin-boson model has, it is the recent surge of theoretical physics research in the area of quantum transport phenomena in photosynthesis that primarily motivates the development of this model.

There have been a few preliminary studies, looking at the role that 3-level systems might potentially play in photosynthesis [45, 44]. However they have so far relied upon numerical techniques that assume one-way dissipation to the bath, which are insufficient

at modelling coherence effects. Therefore in order to model the photosynthesis mechanism more accurately, such that the possibility of relatively long-lived coherences can be established, one must adopt a more advanced approach to modelling the system-environment interaction—one that retains the desired coherence effects. A number of numerical approaches are suited to this; however, in this thesis we are interested in the possibility of obtaining analytic results and ultimately applying them to the case of photosynthesis.

2.1 Truncation procedure for the 3-site-boson model from an extended system

Prior to performing any analysis I must set up the problem, and like most physical systems of interest, I am considering an approximation of some more general system. In my case this amounts to the truncation of a more general potential energy landscape, with three distinct potential wells that permit tunnelling between them, down to three distinct, interacting ground states of each potential well. The problem that I wish to investigate therefore involves a quantum-mechanical system that occupies a 3-dimensional Hilbert space.

In the more general case, the system has a continuous degree of freedom q with a corresponding potential energy function $V(q)$, that forms three separate potential wells. Each well supports multiple quantum mechanical states, but if we assume that the barrier heights between wells are large compared to the energy separation between the ground and first excited state of each well, then the states should localise within each well. Moreover if I assume that the temperature of the system k_BT, as well as bias energies separating the ground states of the potential minima, are small compared to the excited state energies, then states in each well should still be restricted to just their ground states. In other words, the bias energies are small enough such that the system does not localise in any one well, and the temperature k_BT is not too large so as to thermally excite any higher energy states. In effect, the system is now described by a 3D Hilbert space spanned by these three ground states. In this regime, the dynamics of the system is governed by tunnelling between the wells associated with a tunnelling matrix element $\hbar\Delta$, which must also be small compared to the energy level spacings within wells so as not to mix the ground and excited states.

Isolated systems like this are known to exhibit quantum mechanical interference effects between wells. Realistically though any physical realisation of such a system is not

isolated, and exists in the presence of some environment. So far I have only considered a 3-level system isolated from any environment. I refer to this as the 'central system' for which the truncated Hamiltonian is

$$H_0 = \epsilon_1 |1\rangle\langle 1| + \epsilon_2 |2\rangle\langle 2| + \epsilon_0 |0\rangle\langle 0| + \Delta_{10}(|1\rangle\langle 0| + h.c.) + \Delta_{20}(|2\rangle\langle 0| + h.c.) \tag{2.1}$$

where the lower site energy $\epsilon_0 = 0$.

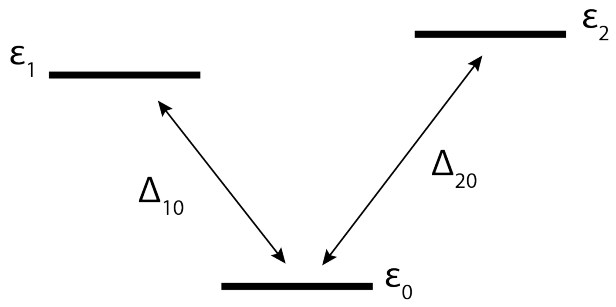

The complete 3-state central system would of course include a tunnelling term between the upper two levels as well. We exclude this term here due to our interest in this particular configuration of the 3-site system, often referred to as a V-system in the quantum optics literature where it sees widespread application [86]. Our interest in this particular 3-site-V-system configuration is motivated by its application to the photosynthesis mechanism discussed in Chapter 1.

2.2 Modelling the environment as a macroscopic harmonic oscillator bath with linear system-bath coupling

I now discuss the interaction of the central system with an external environment. Here I am considering a central system that contains only a few degrees of freedom with respect to the environment, which is assumed to be large with many modes. As the interaction between the central system and each environmental mode is inversely proportional to the size of the bath, for a macroscopic environment we can assume weak coupling to each individual mode. However, the total coupling to the bath can be strong since the full coupling is due to a summation over the couplings to each bath mode. Therefore we can assume that the coupling is linear in bath coordinates, since each individual coupling is

small, but the total coupling can be arbitrarily large [61].

Any linear system composed of a distribution of interacting oscillators can be represented by an equivalent set of independent oscillators [37]. In other words, a linear transformation of the coordinates of the interacting oscillators, recasts the system in terms of its eigenmodes. Since we're assuming that the bath is comprised of a set of simple harmonic oscillators, perturbed only slightly from their equilibrium position, then it is permissible to consider the equivalent set of independent oscillators. Since the bath coordinates will ultimately be summed over, and therefore appear as dummy variables as part of the path-integral measure, it is inconsequential whether the coordinates represent positions or otherwise. The linear transformation coefficients will of course introduce some new normalisation term due to the path-integration measure, however, this is taken in to account in the path integral formalism [37]. I therefore write the Hamiltonian as

$$H = H_S + H_B + H_I \tag{2.2}$$

where H_S is the Hamiltonian of the central system, the 3-site system, H_B is the Hamiltonian describing the environment and H_I the coupling between the two. In the state space the central system is a function of the state label α and for a bath of N Harmonic oscillators

$$H_B = \sum_{q=1}^{N} \left(\frac{p_q^2}{2m_q} + \frac{1}{2} m_q \omega_q^2 x_q^2 \right) \tag{2.3}$$

and

$$H_I = -\sum_{\alpha\beta} \sum_{q=1}^{N} F_{\alpha\beta,q} \left|\alpha\right\rangle\!\left\langle\beta\right| x_q(t) \tag{2.4}$$

where the interaction is linear in bath coordinate $x_q(t)$ and we have excluded a counter-term in the interaction that offsets the renormalisation of the potential in H_S. $F_{\alpha\beta,q}$ is the state-dependent force between state $\alpha\beta$ and an oscillator mode q. Therefore we have associated with this force some state-dependent fluctuating energy $E_{\alpha\beta}(t)$. We have kept H_I general for now, permitting both diagonal $\alpha = \beta$ and non-diagonal $\alpha \neq \beta$ couplings. Second quantising the bath and interaction terms gives

$$H_B + H_I = \sum_{q=1}^{N} \omega_q b_q^\dagger b_q + \sum_{\alpha\beta} \left|\alpha\right\rangle\!\left\langle\beta\right| \sum_{q=1}^{N} \lambda_{\alpha\beta,q} (b_q + b_q^\dagger) \tag{2.5}$$

where $F_{\alpha\beta,q} = \sqrt{2m_q\omega_q}\lambda_{\alpha\beta,q}$. For the case of just diagonal couplings $\alpha = \beta$ in the 3-site model the state-dependent couplings would be $\lambda_{\alpha,q} \in \{\lambda_{1,q}, \lambda_{2,q}, \lambda_{0,q}\}$. Physically, we have described here a bath that is sensitive to the degrees of freedom of the central system. In the polaron literature for example, this usually describes phonons in the environment that are sensitive to the spatial coordinate of the central system particle of interest; i.e. as the particle moves through the environment of phonons, the environment and the particle experience a force between them as a function of their spatial separation [52]. Here, since we're considering a central system in state space, the environment couples individually to each state in the system and there exists a force between each state and each oscillator mode corresponding to a coupling constant $\lambda_{\alpha\beta,q}$.

2.3 The oscillator bath spectral density

I have so far only stipulated that the environment is comprised of a large set of harmonic oscillators and restricted the system-bath coupling to a linear form. However the environment, being the large, complicated structure that it often is, requires further specification as to the distribution of its modes across frequency space. For the case where a thermal equilibrium statistical average is taken over the initial and final states of the environment, then the system-environment coupling can be completely characterised by the spectral density [31, 61]

$$J_\alpha(\omega) = \frac{\pi}{2}\sum_q \frac{\lambda_{\alpha,q}^2}{\omega_q}\delta(\omega - \omega_q) \tag{2.6}$$

which contains the density of states of the bath weighted by the state-dependent system-bath coupling $\lambda_{\alpha,q}$. So we have a spectral density corresponding to each state in the central system with the bath mode part of the coupling summed over. When considering both diagonal and non-diagonal bath couplings we will also have to differentiate between diagonal and non-diagonal coupling strengths. If one is considering some vibronic degrees of freedom in the environment, such as phonons, then to linear order, the bath modes couple to some coordinate in the central system. In the standard literature this is usually derived as a particle, moving with a geometrical coordinate interacting with its environment by displacing the positions of the atoms around it. Therefore the interaction potential depends on the position of the particle from the atoms in the environment around it. To linear order in displacement one arrives at the Hamiltonian above. However since we're considering a state space for the central system, which does not necessarily

involve spatial coordinates, then we don't describe the coupling as being dependent on the central system coordinate, but instead dependent on the state α. In the original spin-boson model for the TSS, the system is said to suddenly jump between positions $\pm q_0/2$, where the bath is coupled to these relative positions. This arises as a coupling to $q_0\sigma_z$ in the interaction term of the Hamiltonian. In fact, the original motivator for Leggett et al. to work on the SB model was to apply it to the SQUID system where the central system coordinate was the flux φ and not at all a geometrical coordinate [93]. Nevertheless they used the coordinate q_0 throughout, along with that caveat. Here instead I consider a coupling $\lambda_{\alpha,q}$ which contains both the state dependence and bath mode dependence.

In the limit of a large number of bath oscillators, where the frequencies ω_q are sufficiently dense so as to form a continuous spectrum, it is appropriate to replace the discrete sum in $J_\alpha(\omega)$ by a continuous integral. In the low frequency limit of the spectral density the spectral density takes the general form

$$J_\alpha(\omega) = A_{\alpha,s}\omega^s\omega_{ph}^{1-s}e^{-\omega/\omega_c} \tag{2.7}$$

For $s = 1$ we have the Ohmic case, for $s > 1$ we are in the super-Ohmic regime. In the latter case we see that the bath frequency is defined in relation to some characteristic bath frequency ω_{ph} that fixes the dimensionality of the spectral density. The state dependence is now contained within the parameter $A_{\alpha,s}$, which will change depending on the value of s and which I will define explicitly in the next sections.

A quantitative measure of the system-bath coupling strength usually used in the literature is the reorganisation energy Λ [84, 27, 94]. This describes the energy released by the bath when relaxing to its equilibrium ground state [64].

$$\Lambda = \frac{1}{\pi}\int_0^\infty d\omega \frac{J(\omega)}{\omega} \tag{2.8}$$

This parameter can be determined experimentally using spectroscopy [95] and is found to be around $\Lambda = 4\text{meV}$ [24, 26]. The justification for quantifying the coupling strength with the measurable reoganisation energy is usually understood in the literature, by first considering the case of zero tunnelling matrix element [56]. Then the chromophore reduces to the well known Independent-boson model [52], an exactly diagonalisable model, which results in site energies shifted by the distortion of the local environment. Associated with this deformation is the reorganisation energy, and the system-environment coupling in this limit is clearly defined. Reintroducing small, but appreciable, tunnelling

matrix elements is then assumed to leave the reoganisation energy picture of system-bath couplings unaltered.

2.3.1 Ohmic damping: $s = 1$

For the special case of Ohmic spectral densities, which will be one form of $J(\omega)$ considered in this work, the damping in the system is independent of frequency [34, 29]. This situation is known to describe the environmental effects of conduction electrons in solids [40, 96] and has been argued to model dissipative energy transfer mechanisms in photosynthesis as well [42, 24, 27] (see also Section 2.3.4). In the Langevin equation this corresponds to a frictional force proportional to the velocity of the path (hence the term Ohmic) [61]. In the high temperature limit, the classical Langevin equation is recovered, which describes a heavy Brownian particle immersed in a fluid of light particles [61]. In this limit the power spectrum of the thermal fluctuations can be described by Johnson-Nyquist noise [97], and thus is of Ohmic form. that In this case the spectral density takes the form

$$J_\alpha(\omega) = \eta_\alpha \omega e^{-\omega/\omega_c} \tag{2.9}$$

which is valid for all frequencies much less than some cutoff frequency ω_c. As the spectral density is a function of both the density of states of the bath modes as well as the state-dependent system-bath coupling, the parameter η_α has an index corresponding to each chromophore. This parameter therefore has units of $Joule \cdot seconds$ and is often referred to as the viscosity coefficient [61]. At this point I can define a dimensionless coupling constant

$$\gamma_\alpha = \frac{\eta_\alpha}{\pi\hbar} \tag{2.10}$$

which will be used in proceeding calculations.

The measured value of the dimensionless coupling constant is measured to be $\gamma = 0.22$ for an Ohmic bath in the FMO complex [98]. The corresponding cut-off frequency was found to be $\hbar\omega_c = 21.1\text{meV}$.

2.3.2 Super-Ohmic damping (acoustic phonons): $s = 3$

For the case of $s = 3$ the spectral density is known as super-Ohmic. The physical basis for a spectral density of this form can be realised in the coupling of the system to

a 3-dimensional acoustic phonon bath [61, 31]. One can arrive at this cubic frequency dependence with a system-bath coupling $\lambda_q \propto \omega_q^{-1/2}$ for elastic waves and a Debye density of state $\sum_q \delta(\omega - \omega_q) \propto \omega^2$. Recall that, for low enough frequencies, it is assumed that phonons still have a well defined wavevector for amorphous solids. Further summation over the one longitudinal, and two transverse branches of the dispersion, results in a spectral density to the 3rd order in ω [99]. Therefore, for the low frequency distribution of the bath, the spectral density takes the form

$$J_\alpha(\omega) = \rho_\alpha \frac{\omega^3}{\omega_{ph}^2} e^{-\omega/\omega_c} \tag{2.11}$$

Once again the coefficient ρ_α has units of $Joule \cdot seconds$. I can therefore define a dimensionless coupling parameter that this time takes the form

$$\zeta_\alpha = \frac{\rho_\alpha}{\pi\hbar} \tag{2.12}$$

which is independent of the characteristic bath frequency ω_{ph}. Instead, we'll see that during the calculations in subsequent chapters, that I instead end up with a ratio of cut-off frequency to characteristic phonon bath frequency in our expressions. The dimensionless coupling constant and cut-off frequency were found to be $\zeta = 0.31$ and $\hbar\omega_c = 8.7$meV respectively [98].

It is worth briefly discussing the significance of phonons and super-Ohmic spectral densities in the context of amorphous solids. Phonons are normally discussed in the context of ordered lattices where there exists a well-defined translational symmetry. In this case we can describe the distribution of phonon modes with a dispersion relation according to a well-defined plane-wave excitation momentum. In disordered (amorphous) solids, despite the lack of translational symmetry, low-frequency vibrational modes similar to those of a crystalline lattice [100, 101] are present. This can be conceptually understood by first considering an ordered lattice with a phonon dispersion. Introducing disorder should affect the high-frequency modes first as the low-frequency modes do not 'see' the disorder due to their long wavelength. For higher, and higher disorders, we expect the high frequency phonons to be scattered and only very low frequency modes to survive.

The environment of a chromophore is of course not an ordered lattice but an amorphous one with some degree of disorder. Nevertheless it is clear that vibrational excitations exist in such amorphous systems arising from the protein structure that surrounds each chromophore [46, 102].

2.3.3 Optical phonon damping with spectral broadening

For the case of optical phonons the spectral density contains just one frequency ω_0 and the zero-temperature spectral density includes just a delta function. However for realistic applications we would like to add a small linewidth to simulate some damping by the environment. In this case I choose a Gaussian lineshape

$$J_\alpha(\omega) = \lambda_\alpha \exp\left[-\frac{(\omega-\omega_0)^2}{2\xi^2}\right] \tag{2.13}$$

with fullwidth-half-maximum ξ and coupling strength λ_α that determines the height of the peak and has units of *Joules*. In this case the coupling strength λ_α corresponds directly to the coupling strength in the system-bath interaction part of the Hamiltonian (see equation 2.5). The dimensionless coupling parameter in this case is

$$\nu_\alpha = \frac{\lambda_\alpha \xi}{\pi \hbar \omega_0^2} \tag{2.14}$$

where ξ and ω_o have units of frequency.

Optical phonon peaks appearing in the structured spectra of the FMO complex, tend to be relatively narrow and oscillate at very high frequency relative to the FMO system tunnelling frequencies. Linewdiths are of the order $\hbar\xi \sim 1 - 10$meV, and oscillation frequencies $\hbar\omega_0 \sim 50 - 250$meV. This range of values describes narrow peaks centered at relatively high energies.

2.3.4 Spectral density functions for light-harvesting molecules

Having introduced various general forms for spectral density functions, I now discuss their application to the case of photosynthesis. Previous analytical approaches to modelling chromophore dynamics have made various assumptions as to the nature of chromophore-environment interactions. Approaches by Gilmore [41, 42, 43], Ishizaki [21] and Cho [103] have assumed a Debye-solvent approximation to the susceptibility function of the environment. The resulting spectral density is of the Ohmic form with a Drude-Lorentz regularisation [87], which has the same low-frequency behaviour as the overdamped Brownian oscillator model [104, 105]. The Ohmic form for the spectral density describes a heavy Brownian particle immersed in a fluid of relatively light particles [61]. The model is linear in bath-mode-frequencies with a long-tail high frequency cut-off. For the case of a Debye-solvent, the model assumes that the environment is a homogeneous dielectric [41, 42] based upon the Onsager model of solvation [106, 107]. This combined with the

Debye-solvent approximation models the dielectric solvent well, provided it is highly dilute [108].

While this model is useful in considering a specific microscopic model, of given solute dimensions as well as solvent dielectrics, it is generally restricted to the class of solvents and excludes any rigid protein structure in the environment. In either case one would expect the influence of both acoustic and optical phonons to play a significant role in chromophore dynamics. Nonetheless, light-harvesting molecules are suspended in an aqueous solution and we expect the solvent to affect the solute dynamics as well as possibly explaining why the Ohmic form for the spectral density has had some success in modelling light-harvesting molecules [109, 110, 111].

Light-harvesting molecules are surrounded by a protein structure that contains a large number of degrees of freedom. We are often interested in the response of the system to the low-frequency portion of the spectrum and thus a super-Ohmic spectral density can be employed. A number of studies on these systems have used a super-Ohmic spectral density [112, 46, 113]. One can of course turn to experimentally determined spectra for an understanding of the nature of system-environment interactions. An accurate determination of the energetic structure and system-environment interactions present in a complex system such as FMO is difficult. As a result, the general method of determining these parameters is to perform complex fitting algorithms on experimentally determined optical spectra, and various approximations have been proposed and implemented on FMO.

One of the canonical works on FMO line-spectra calculations is that by Adolphs and Renger [46]. They estimated the exciton-environment coupling based on the fluorescence line-narrowing spectrum. The result was a spectral density of cubic form with a peak at around 0.02eV and an exponential cut-off for high frequencies. Nalbach et al. extended this to a ω^5 frequency dependence as well as the inclusion of a single optical transition peak. They found the inclusion of the peak to alter the exciton dynamics only slightly [26]. Flemming's group [21] calculated the exciton dynamics using a low-frequency Ohmic approximation for the spectral function that relies on the Drude approximation for the solvent environment [41]. Olbrich et al. [114] have calculated the spectral function based on a combination of exponential and damped oscillations for the correlation function. The resulting function is combination of a temperature-dependent function and Lorentzians. The number of peaks corresponds to the number of terms included in their fitting functions to experimental data. Depending on their algorithm, they find around 13 peaks with various spectral weights.

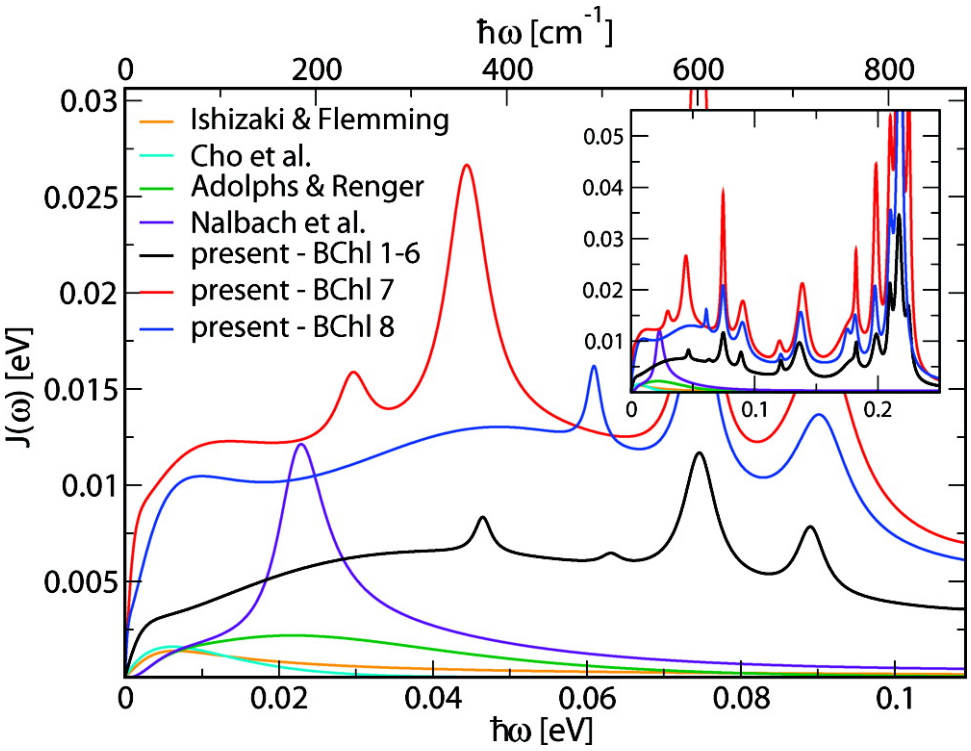

Figure 2.1: Spectral densities for the FMO trimer used in studies by Ishizaki and Fleming [21], Cho et al. [103], Adolphs and Renger [46], as well as Nalbach et al. [26]. Spectral densities fitted to experimental data by Olbrich [114] also included, indicated by the lines 'present - BChl 1-6', 'present - BChl 7', 'present - BChl 8', corresponding to the average over BChl molecules 1-6, 7 and 8 respectively. The inset shows an enlarged energy and spectral density range. Reprinted with permission from [114].

We see from Figure 2.1, where the results of the various approximation methods are compared, that they differ not only in qualitative features, but also in magnitude. The studies of Cho [103], Adolphs [46] and Ishizaki [21] assumed only low-frequency vibrational modes of either Ohmic or super-Ohmic form. Nalbach [26] included a single internal vibrational mode, evident by the single peak on top of the low-frequency distribution. However, the most up-to-date study by Olbrich et al. [114] not only found many more optical phonon transitions in the spectra, but found a much larger amplitude to the spectral density across frequencies, especially for the outlying BChla molecules 7 and 8 that sit on the peripheries of the FMO structure and are thus weakly bound. The core of the FMO structure, comprised of BChla 1-6, which were the focus of the other studies, are more relevant to compare. Olbrich et al. still finds an elevated amplitude across frequencies

but less significant optical phonon transitions. This is with the exception, however, of a strong peak at around 0.22eV. This peak has been attributed to several carbon-oxygen and carbon-carbon bonds, present in the BChla molecules internal structure that vibrate with similar frequencies [115, 114]. For low-energies below 0.01eV, Olbrich find system-bath interactions approximately 2-3 times larger than other studies. In Table 2.1, two optical phonon peaks are selected from the FMO spectra calculated by Olbrich [114], corresponding to the 0.22eV peak and a lower frequency peak at 0.075eV. We see how the dimensionless coupling parameter associated with these peaks is much less than one which suggests a perturbative approach to modelling the system-bath dynamics with these optical phonon peaks should be sufficient. This is done in Section 3.3. In the interest of investigating the non-perturbative effect of optical phonon peaks on the FMO dynamics, I also select peaks at $6, 8$ & 10meV

Optical phonons			
ν	$\lambda(meV)$	$\xi(meV)$	$\omega_0(meV)$
0.003	35	12.5	220
0.004	12.5	5	75
0.1	12.5	0.5	5

Table 2.1: FMO parameters for optical phonons characterised by their peak height λ, full-width-half-maximum ξ and dimensionless coupling parameter $\nu = \lambda\xi/\pi\omega_o^2$ in units of meV. Taken from Olbrich et al. [114].

In the interest of clarity I've converted all the parameters to units of meV (N.B. Planck's constant in the above units is $\hbar = 658\text{meV} \cdot \text{fs}$).

For the acoustic phonons I take the FMO values determined from Jang and Mennucci [98], which provides an up-to-date, comprehensive review of fitted spectral functions for the system-environment interactions in FMO. Here the spectral density function used is of the form

$$J_\alpha = \rho_\alpha \frac{\omega^3}{\omega_c^2} e^{-\omega/\omega_c} \tag{2.15}$$

where the corresponding dimensionless coupling is $\zeta_\alpha = 0.31$ and cut-off frequency $\omega_c = 8.7\text{meV}$.

For an Ohmic bath, the spectral density function used is of the form

$$J_\alpha = \eta_\alpha \omega e^{-\omega/\omega_c} \tag{2.16}$$

where the corresponding dimensionless coupling is $\gamma_\alpha = 0.22$ and cut-off frequency $\omega_c = 21.1\text{meV}$.

2.4 The path-integral approach to modelling open-quantum mechanical systems and the Feynman-Vernon influence functional

When investigating how a quantum mechanical system interacts with its environment, we are usually interested in tracking the degrees of freedom within the 'central' quantum mechanical system under the influence of the degrees of freedom within the environment. This ultimately means that the mathematical formalism I wish to work with must cast the effects of the external system only in terms of the coordinates of the central system. This way I can explore the free parameters of the central system of interest under the influence of its environment without having to track every degree of freedom in the problem, system-plus-environment at once. One of the most successful formalisms that achieves this is that of the Feynman-Vernon influence functional approach [37]. The resulting mathematical object that facilitates these calculations is known as the Feynman-Vernon influence functional. This method allows us to consider an arbitrarily strong coupling to the environment and retain 'memory effects', such that the system can feed energy to the bath and experience feedback as well.

2.4.1 The path integral formalism of quantum mechanics

Central to this method of modelling open quantum systems is the path-integral approach to quantum mechanics devised by Feynman [116]. When the formalism was introduced in the mid-20th century it provided physicists with the understanding that a quantum mechanical system can be thought of as exploring every possible path available to it, with each path weighted by a phase factor. The overall probability amplitude for a given process therefore amounts to integrating (or summing) over all possible paths the system might take. The resulting functional integral can be thought of as a sum over possible configurations of the system at each consecutive time. I briefly describe this concept below due to its relevance to our calculations in subsequent chapters.

Consider a time-independent Hamiltonian for a particle of mass M in a one-dimensional potential $V(x)$, with coordinate x

$$H = T + V, \quad T = \frac{p^2}{2M} \tag{2.17}$$

where p is the particle's momentum. The solution of the Schrödinger equation can be written in the form

$$|\Psi(t)\rangle = e^{-iHt/\hbar} |\Psi(0)\rangle \quad \langle x|\Psi(t)\rangle = \int dx' G(x,t;x',t'=0) \langle x'|\Psi(0)\rangle , t > 0 \tag{2.18}$$

with the introduction of the propagator (or Greens function)

$$G(x,t;x',0) = \langle x| e^{-iHt/\hbar} |x'\rangle \tag{2.19}$$

Dividing the time interval into infinitely small pieces and utilising the Trotter product (see Section 3.2 of [117]), which allows one to ignore the non-commutivity of the kinetic and potential operators in the Hamiltonian, leads to the path integral form of the propagator

$$G(x,t;x',0) = \int_{x'}^{x} Dx\, e^{iS_{cl}} \tag{2.20}$$

where

$$S_{cl} = \int_0^t dt' \frac{M\dot{x}^2}{2} - V \tag{2.21}$$

is the classical action and

$$Dx = \lim_{N\to\infty} \int dx_1 ... dx_{N-1} \left(\frac{MN}{2\pi i t}\right)^{\frac{N}{2}} \tag{2.22}$$

is the Feynman path integral measure. We see from equation 2.20 how the problem of calculating the Greens function for a system is reduced to 'summing over all possible paths'. In the case of our relatively simple system, where there are only a few degrees of freedom in the central system, this functional integral amounts to the product of time 'slices', where we sum over all possible configurations of the system at each time slice.

Such a formalism for the transition amplitude involves a single path integral. In the interest of modelling decoherence processes, one must consider a double path integral formalism for the density matrix. For the isolated case, where there is no environment

and just a central system, the two paths are independent. In realistic physical systems we have an environment interacting with our 'central system' and this couples the two paths. Therefore I must include some system-bath interaction term in the Hamiltonian and then deal with all the degrees of freedom introduced to the problem with the bath. The method I employ here to do so is the influence functional method.

2.4.2 The influence functional

I now include the environment by way of the influence functional method developed by Feynman and Vernon [37]. This method would later see application to the spin-boson model analysed by Leggett et al. [31]. Here I briefly summarise the technique.

Suppose that at time $t = 0$ the system and environment are uncoupled and the environment is in thermal equilibrium. In this case the density matrix of the composite system is in a product state

$$\rho(0) = \rho_S(0) \otimes \rho_E(0) \tag{2.23}$$

where ρ_S is the reduced density matrix for the central system and ρ_E that of the environment. It should be noted that this is of course a somewhat artificial situation but nonetheless one that can bear direct experimental relevance to a system if it is initially prepared in this state with sufficiently strong bias forces, which are subsequently switched off at $t = 0$. It's also worth noting, within the context of the applied model to photosynthesis, that this initial condition has been argued to be valid [21]. Since the electronic excitation process in EET corresponds to an excited (or ground) state prepared by photoexcitation in accordance with the Franck-Condon transition, this factorised initial state should be applicable. Incidentally the product initial state is the simplest starting point for these kinds of calculations and so is utilised in this work. I therefore assume that the system-bath coupling is suddenly switched on at $t = 0$ and I consider the dynamics of $\rho(t), \forall\, t > 0$. Feynman and Vernon found the resulting form for the reduced density matrix to be

$$\begin{aligned} \rho_S(x_f, x'_f; t) &= \sum_{x_i, x'_i} K_{FV}(x_f, x'_f; x_i, x'_i; t)\rho(x_i, x'_i; 0) \\ K_{FV}(x_f, x'_f; x_i, x'_i; t) &= \int_x^{x_f} Dx \int_{x'}^{x'_f} Dx' \exp\left\{ \frac{i}{\hbar} \left(S_S[x] - S_S[x'] \right) \right\} F_{FV}[x, x'] \end{aligned} \tag{2.24}$$

where K_{FV} is the propagating function determining the time evolution of the central system under the influence of the bath. The object $F_{FV}[x, x']$ is the Feynman-Vernon influence functional, which contains all the information about the bath as a function of the central system coordinates x, x'. Therefore the coordinates pertaining to the bath variables are integrated out within the influence functional itself and we are left with only the system coordinates as desired. One of the main results of the work of Feynman-Vernon was to calculate the exact form of the influence functional for a bath of harmonic oscillators coupled linearly to the central system. The result is

$$F_{\alpha\beta\gamma\delta}\big[x, x'\big] = \exp\Big\{ -\frac{1}{\pi\hbar}\int_{t_0}^{t} d\tau \int_{t_0}^{\tau} ds\big[-iL'(\tau - s)\big(x_\alpha(\tau) + x'_\beta(\tau)\big)\big(x_\gamma(s) - x'_\delta(s)\big) \tag{2.25}$$

$$+ L''(\tau - s)\big(x_\alpha(\tau) - x'_\beta(\tau)\big)\big(x_\gamma(s) - x'_\delta(s)\big)\big]\Big\} \tag{2.26}$$

where x_α, x'_α represent the two paths of the density matrix that can visit each state in the system [37, 61]. The full influence functional involves a sum over all possible paths

$$F = \sum_{\alpha\beta\gamma\delta} F_{\alpha\beta\gamma\delta} \tag{2.27}$$

The bath correlators

$$L'(\tau - s) = \int_0^\infty d\omega J(\omega) \sin\omega(\tau - s) \tag{2.28}$$

$$L''(\tau - s) = \int_0^\infty d\omega J(\omega) \cos\omega(\tau - s) \coth(\beta\hbar\omega/2) \tag{2.29}$$

describe the time evolution of the bath, and contain the bath spectral density $J(\omega)$. $L'(t)$ is related to the damping kernel in the classical Langevin equation [61] and physically describes the coherent exchange of energy with the environment. $L'(t)$ determines the loss of phase coherence in the system due to fluctuations in the environment. It is convenient to transform the double path integral over x and x', into a single path integral that visits all the possible states. For this I define ξ, χ to be the anti-symmetric and symmetric paths respectively

$$\xi_{\alpha\beta}(t) \equiv x_\alpha(t) - x'_\beta(t), \quad \chi_{\alpha\beta}(t) \equiv x_\alpha(t) + x'_\beta(t) \tag{2.30}$$

The state $\xi(t)$ represents the off-diagonal terms of the rotated density matrix–the quantum coherences of the state between different positions. The state $\chi(t)$ indexes how far down the diagonal of the density matrix we move and so tracks the incoherent hopping of the system. So $\xi(t)$ measures the difference in coordinates $x - x'$ and is zero whenever the system is in a diagonal (onsite) state and vice versa for χ. For a 3-site system, which allows the values $x_\alpha \in \{x_1, x_0, x_2\}$, we have for the density matrix therefore

$$\rho = \begin{pmatrix} \rho_{x_1,x_1} & \rho_{x_1,x_0} & \rho_{x_1,x_2} \\ \rho_{x_0,x_1} & \rho_{x_0,x_0} & \rho_{x_0,x_2} \\ \rho_{x_2,x_1} & \rho_{x_2,x_0} & \rho_{x_2,x_2} \end{pmatrix} \tag{2.31}$$

Which is reparameterised in terms of the functions χ, ξ as

$$\rho = \begin{pmatrix} \rho_{\chi_{11},0} & \rho_{\chi_{10},\xi_{10}} & \rho_{\chi_{12},\xi_{12}} \\ \rho_{\chi_{01},\xi_{01}} & \rho_{\chi_{00},0} & \rho_{\chi_{02},\xi_{02}} \\ \rho_{\chi_{21},\xi_{21}} & \rho_{\chi_{20},\xi_{20}} & \rho_{\chi_{22},0} \end{pmatrix} \tag{2.32}$$

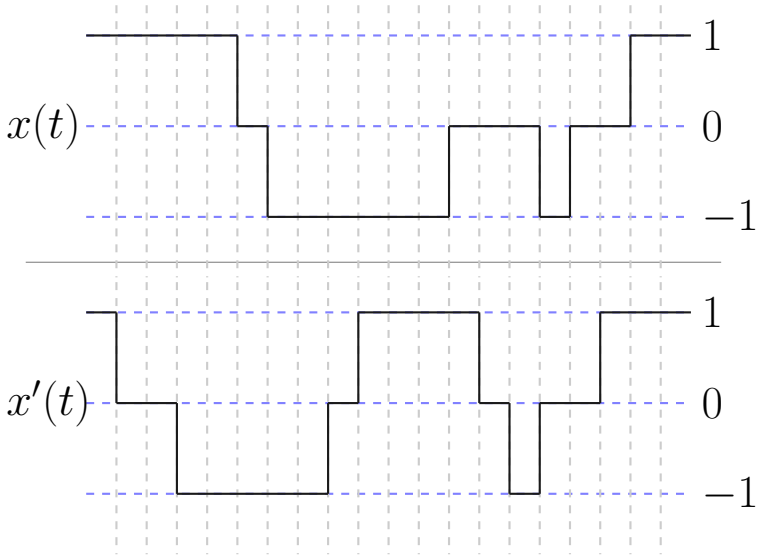

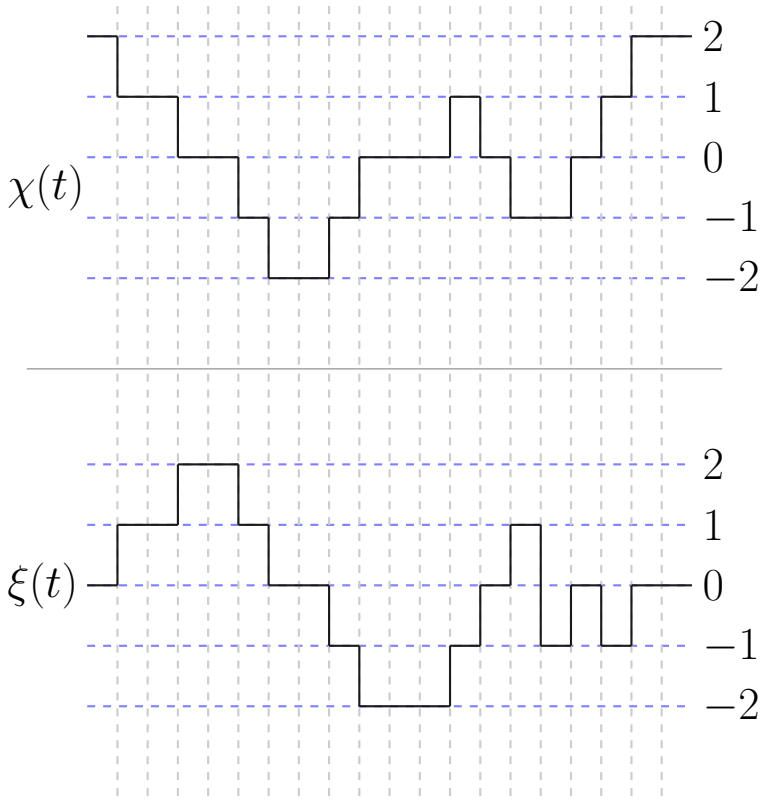

Figure 2.2: An example of possible paths $x, x' \in \{1, 0, -1\}$ for the general 3-site system and their corresponding symmetric/anti-symmetric paths $\chi \in \{2, 1, 0, -1, -2\}$, $\xi \in \{2, 1, 0, -1, -2\}$.

In Figure 2.2 we see an example of possible paths taken by x and x' for a general 3-site system and the corresponding symmetric and anti-symmetric paths χ, ξ.

Substituting the symmetric and antisymmetric paths into the influence functional gives

$$F_{\alpha\beta\gamma\delta}\big[\chi,\xi\big] = \exp\Big\{\frac{1}{\pi\hbar}\int_{t_0}^{t} d\tau \int_{t_0}^{\tau} ds\big[2iL'(\tau-s)\chi_{\alpha\beta}(\tau)\xi_{\gamma\delta}(s) - L''(\tau-s)\xi_{\alpha\beta}(\tau)\xi_{\gamma\delta}(s)\big]\Big\} \tag{2.33}$$

I assume here that the paths take the form of an instantaneous flip whereby the path jumps between the available locations instantly. Assuming the system begins in a sojourn state, and flips between successive sojourn states via blips in either transition $|1\rangle \leftrightarrow |0\rangle$ or $|2\rangle \leftrightarrow |0\rangle$, I can parameterise the symmetric/anti-symmetric paths according to the sudden-flip approximation [31]

$$\chi_{\alpha\beta}(t) \equiv \sum_{i=0} \chi_j^{\alpha\beta}\Big[\Theta(t-t_{2i}) - \Theta(t-t_{2i+1})\Big], \quad \xi_{\alpha\beta}(t) \equiv \sum_{j=1} \xi_j^{\alpha\beta}\Big[\Theta(t-t_{2j-1}) - \Theta(t-t_{2j})\Big] \tag{2.34}$$

This particular parameterisation in terms of the above combination of step functions produces sojourns that live for even-times $t_{2i+1} - t_{2i}$ and blips for odd-times $t_{2j} - t_{2j-1}$ N.b. I assume we start in a sojourn at $t = 0$. This way, the system moves from sojourn-blip-sojourn and so forth. We'll see below that the construction of the influence functional is such that the effect of the bath is to suppress time spent in the blip states, i.e. the coherent/off-diagonal states. And so in the classical limit, where the bath has fully suppressed the blips, the system hops incoherently between sojourns i.e. diagonal states within the system. Substituting into the influence functional and performing the integrals gives

$$F_{\alpha\beta\gamma\delta}[\chi,\xi] = \exp\Big\{\frac{1}{\pi\hbar}\Big[i\sum_{i=0}\sum_{j=1}\chi_i^{\alpha\beta}\xi_j^{\gamma\delta}X_{ij} - \sum_j\Big(\xi_j^{\alpha\beta}\Big)^2 Q''_{2j,2j-1} - \sum_{i=1}\sum_{j=2}\xi_i^{\alpha\beta}\xi_j^{\gamma\delta}\Lambda_{ij}\Big]\Big\} \tag{2.35}$$

where I have defined the bath correlations Λ_{ij} between blip-blip pairs $\{i,j\}$ and blip-sojourn correlations X_{ij} between a sojourn at i and a blip at j

$$\begin{aligned} X_{ij} &\equiv Q'_{2i,2j+1} + Q'_{2i-1,2k} - Q'_{2i,2k} - Q'_{2i-1,2k+1} \\ \Lambda_{ij} &\equiv Q''_{2i,2j-1} + Q''_{2i-1,2k} - Q''_{2i,2k} - Q''_{2i-1,2k-1} \end{aligned} \tag{2.36}$$

where I have used the compact notation

$$Q'_{i,j} \equiv Q'(t_{2i} - t_j) \quad Q''_{i,j} \equiv Q''(t_i - t_j) \tag{2.37}$$

and where

$$Q'(t-t') = \int_0^\infty d\omega \frac{j(\omega)}{\omega^2}\sin\omega(t-t') \tag{2.38}$$

$$Q''(t-t') = \int_0^\infty d\omega \frac{j(\omega)}{\omega^2}(1-\cos\omega(t-t'))\coth(\beta\hbar\omega/2) \tag{2.39}$$

So a sojourn at time interval i can interact with a blip at j and a blip can interact with itself as well as other blips.

It's worth noting that the prescription to sum over all paths in the path integral formalism involves an integration over each 'time-slice' as well as a sum over all the possible blip and sojourn states that are available within each transition. The first term in the influence functional represents interferences between sojourn-blip-sojourn paths, i.e. paths that start in some sojourn, undergo a blip, and return to the same sojourn. The second term is the self-interaction of the blips, so the same blip interacting with itself. The third term is the interaction between different blips, therefore a blip at some interval $t_j - t_k$ in one transition can interact at a later time with another blip from either transition.

The sojourns themselves represent the diagonal elements of the density matrix while the blips represent the off-diagonal elements. Therefore one should think of the blips as the coherences between states in the system. We see that the second term in the influence functional serves to suppress the weight of these coherent paths. Physically, this represents the bath 'measuring' the system and leading to the destruction of phase coherence between paths through the system. The effect of the bath therefore is to induce decoherence in the system, such that the paths eventually are restricted to the classical case of hopping between discrete sites.

2.5 The noninteracting-blip approximation (NIBA)

The full influence functional as it stands includes all possible pairings of blips and sojourns as well as blip-blip interactions. This means that all time-non-local interactions are included such that a blip-sojourn/sojourn-sojourn interaction can occur for blips and sojourns separated across the entire time domain. Not only does this include an inordinate number of pairings for large number of flips n, but the exponentiation of these, in the path integral formalism, creates all possible diagrams. Therefore in its general form, the influence functional presents a formidable mathematical object to evaluate and some approximations are required. In the interest of retaining a non-perturbative system-bath coupling, one approach to truncating the number of processes is to consider a system that dwells mostly in diagonal states of the density matrix. The system is still permitted to occupy the off-diagonal elements, and therefore we retain those quantum coherence effects; however, these excursions are infrequent and short-lived. This means that time-non-local interactions between these off-diagonal states with each other are suppressed

due to the fact that they are separated by large time-intervals, and the memory effects introduced via the bath are lost. This amounts to the well-known noninteracting-blip approximation (NIBA) [31].

The underlying assumption here is that the average time spent by the system in a diagonal element (sojourn) of the density matrix $\langle s \rangle$ is much larger than that spent in an off-diagonal element (blip) $\langle b \rangle$. This ultimately amounts to neglecting interactions between different blips except for the self-interaction of blips. This leads to a strong suppression of time spent in the off-diagonal terms of the density matrix as the bath is rapidly measuring the state of the central system and forcing it back to diagonal states. For the 3-site-system of interest, this mathematically corresponds to considering only the interaction between diagonal states $\chi_{11}, \chi_{22}, \chi_{00}$ and off-diagonal blips ξ_{10}, ξ_{20}.

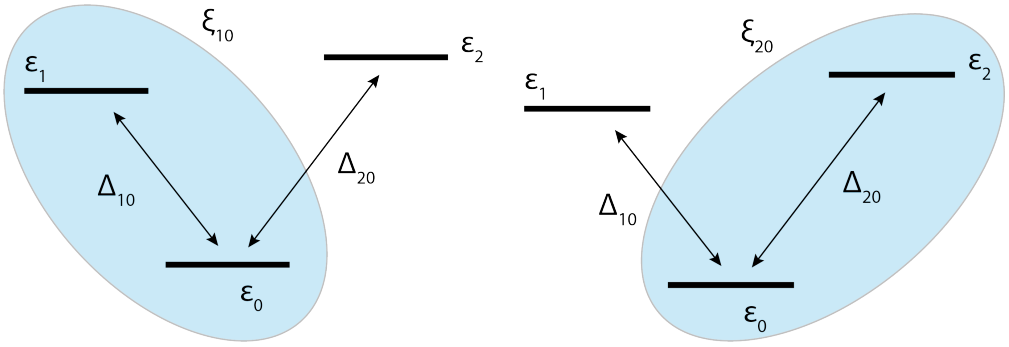

Figure 2.3: Diagrammatic depiction of possible coherent states (blips) permitted in 3-site-V model under NIBA. ξ_{10} represents a wavefunction overlapping with states $|1\rangle$ and $|0\rangle$, while ξ_{10} represents an overlap with $|2\rangle$ and $|0\rangle$

To see this we first inspect the term involving the bath correlator $Q'(t-t')$ in equation 2.39. In the influence functional, this term appears in the part involving sojourn-blip interactions. Upon inspection we see that the full function X_{ij} that contains all the bath correlators Q', reduces to just the single term $Q'(t_{2j} - t_{2j-1})$, in the limit of $\langle b \rangle / \langle s \rangle \to 0$ as the length of sojourns dominates. Terms that involve interactions between blips and sojourns and are not nearest-neighbours in time, contain arguments that are very large and they become rapidly oscillating functions. By the Riemann-Lebesgue lemma these terms go to zero with the integral over ω

$$\int_0^\infty d\omega \frac{J(\omega)}{\omega^2} \sin \omega(\tau) \to 0 \quad \text{as} \quad |\tau| \to \infty \tag{2.40}$$

The blip-blip interactions are handled in a less direct way within NIBA. The third term in equation 2.35 represents the interaction of non-time-local blips, and for this to be neglected, the blip-blip-propagators contained in $\Lambda_{j,k}\,\forall j \neq k$ must all be much less than the blip-sojourn propagators contained in $X_{j,j-1}$ as well as the blip-self-interaction term containing $Q''_{j,j-1}$. This amounts to minimising the ratio

$$\frac{Q''\langle s\rangle + \langle b\rangle)}{Q'(\langle s\rangle)} \tag{2.41}$$

where $\langle s\rangle, \langle b\rangle$ are the average sojourn and blip times respectively. $Q''\langle s\rangle + \langle b\rangle)$ contains as its argument the time between nearest-neighbour blips, separated by the sojourn interval. In order to better understand this part of NIBA, I pre-emptively quote the forms of the bath correlators $Q'(t), Q''(t)$ for an Ohmic spectral density so that I can justify the approximation in the appropriate regime. The Ohmic form of the correlators are [31]

$$Q'(t) = \arctan(\omega_c t) \tag{2.42}$$

$$Q''(t) = \frac{1}{2}\ln(1+\omega_c^2 t^2) + \ln\left[\frac{\hbar\beta}{\pi t}\sinh\left(\frac{\pi t}{\hbar\beta}\right)\right] \tag{2.43}$$

The length of a sojourn is of the order $1/\Delta$ and if one considers timescales in the problem $\omega_c/\Delta \gg 1$, then the blip-sojourn propagator $Q'(\langle s\rangle) = \arctan(\omega_c/\Delta) \sim \pi/2$. In the limit of $\langle s\rangle \gg \langle b\rangle$, the argument of the blip-blip-propagator term, which contains non-local interactions between blips, vanishes, i.e.

$$\lim_{\langle s\rangle \gg \langle b\rangle} \Lambda_{jk} \to 0 \tag{2.44}$$

This is because the propagators in Λ_{ij} involve non-local blip-blip interactions whose time arguments are of the order of $\langle s\rangle + \langle b\rangle \sim \langle s\rangle$ and therefore cancel. In Figure 2.4 we see a graphical representation of the nearest-neighbor contribution to the term $\sum_{i=1}\sum_{j=i+1}\xi_i\xi_j\Lambda_{ij}$, where the four propagators lines correspond to the four terms in the equation

$$\Lambda_{12} \equiv Q''(t_4-t_1) + Q''(t_3-t_2) - Q''(t_4-t_2) - Q''(t_3-t_1) \tag{2.45}$$

and all the terms in this function cancel when the resolution of the blips $\langle b\rangle$ vanishes.

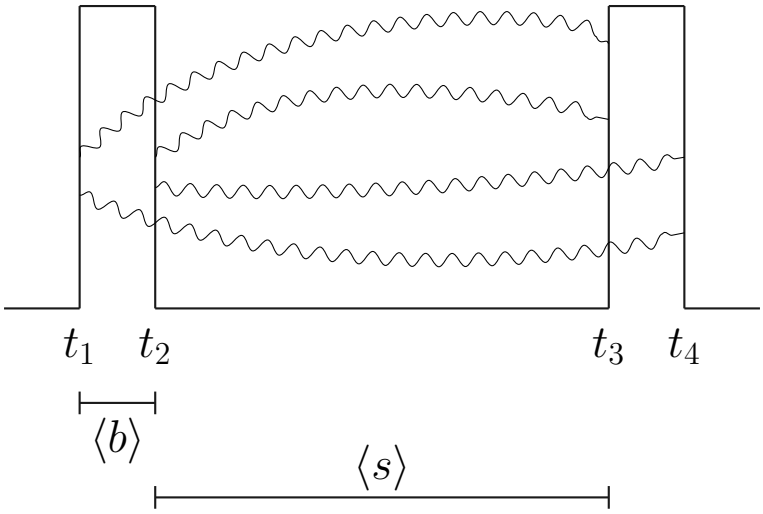

Figure 2.4: Diagrammatic representation of the interaction terms contributing to the blip-blip interaction propagators Λ_{jk}. The contribution depicted is a nearest-neighbor interaction of blips.

In summary, NIBA amounts to setting the factors $Q'_{i,j}$ to zero for $j \neq i-1$ such that we're just left with $Q'_{2j,2j-1} = Q'(t_{2j} - t_{2j-1})$. I also set all Q''_{ij} equal to zero as they represent blip-blip interactions.

As it stands, the full density matrix in equation 2.32 presents a fairly formidable combinatorics problem in terms of the possible paths that can be tracked through it. Since in NIBA we are permitted to spend only one time interval in an off-diagonal state of the density matrix, this greatly reduces the number of possible paths. In this case the states ξ_{12}, ξ_{21} become inaccessible and the intermediate states $\chi_{10}, \chi_{20}, \chi_{12}$ are neglected as well.

$$\rho = \begin{pmatrix} \rho_{\chi_{11}} & \rho_{\xi_{10}} & 0 \\ \rho_{\xi_{01}} & \rho_{\chi_{00}} & \rho_{\xi_{02}} \\ 0 & \rho_{\xi_{20}} & \rho_{\chi_{22}} \end{pmatrix} \tag{2.46}$$

So the blips and sojourns for the 3-site-V system within NIBA can take on the values

$$\xi_{\alpha\beta} \in \{\xi_{10}, \xi_{20}\}, \quad \chi_{\alpha\beta} \in \{\chi_{11}, \chi_{00}, \chi_{22}\} \tag{2.47}$$

Having established that NIBA corresponds to the situation where $\langle s \rangle \gg \langle b \rangle$, it is prudent to ask in what regions of the parameter space of the system is it valid. A general central system of interest can be parametrised by bias energy ϵ, tunnelling energy Δ, temperature

k_BT and system-environment coupling λ. The first intuitive limit to consider, which is most applicable to this thesis, is where $\epsilon \gg \Delta$. In this limit, one intuitively expects the system to spend more time in the diagonal elements of the density matrix as opposed to the off-diagonal elements. This can be appreciated as the limit where the central system is best described in the site basis as opposed to the eigenstate basis. In the latter case, where tunnelling energies dominate, states are hybridised and one would expect the system to spend relatively long time intervals in off-diagonal elements of the density matrix. However, NIBA is known to be applicable in other areas of the parameter space and is worth commenting on there.

When the bias energy is not necessarily large, long blips are known to be suppressed at long times in conjunction with large damping and/or high temperatures for Ohmic baths. Incidentally both of these criteria are actually met in this thesis when Ohmic baths are considered, indeed they are necessary assumptions to achieve analytic solutions. For super-Ohmic spectral densities, blip-blip interactions tend to be suppressed relative to intrablip interactions for large temperatures, and the NIBA condition is met [61]. Finally, for zero bias, NIBA is also known to be valid in the limit of weak system-bath coupling such that only one-phonon processes need be considered [31]. In fact it is exact in this limit, and can be used to evaluate the bath correlation functions when applying perturbation theory in the system-environment interaction.

2.6 Validity of NIBA: a quantitative measure

I established in the preceding section that the condition that must be met in order to ignore the time-non-local blip-sojourn and sojourn-sojourn interactions in the influence functional is $\langle s \rangle \gg \langle b \rangle$. How this condition is met depends upon the various parameters in the model, as discussed above, and will change depending on the limits I inspect. In order to quantify the validity of NIBA in each limit more precisely, I outline the mathematical condition that applies. As the influence functional contains all the bath parameters, including the system-bath coupling, it dictates the nature of the blips and sojourns in the system. I am interested specifically in the average length of a blip $\langle b \rangle$, and I can extract this quantity from a consideration of the various moments to the probability distribution that the influence functional represents. To see this I first expand the general influence functional in a power series about $\lambda = 0$

$$F(\lambda) = F_0 + F_1\lambda + ... \tag{2.48}$$

where

$$F_0 = \lim_{\lambda \to 0} F(\lambda), \quad F_1 = \lim_{\lambda \to 0} \frac{\partial}{\partial \lambda} F(\lambda) \tag{2.49}$$

The first term, F_0, in the expansion represents the purely incoherent decay rate from the system and the ratio, $F_1/F_0 = \langle b \rangle$, is the first moment of the system. To see this, recall that the expansion of the moment-generating function of a random variable X is

$$M_X(t) = 1 + m_1 t + m_2 \frac{t^2}{2!} + ..., \quad m_n = \lim_{t \to 0} \frac{d^n M_X}{dt_n} \tag{2.50}$$

where m_n is the nth moment. We further recall that the term in the influence functional that's a function of $Q''(t)$, controls the width of the blips. Therefore, aside from the additional cosine terms coming from the tunneling matrix element renormalisation, the first moment of the influence functional tells us the average blip width $\langle b \rangle$. NIBA is valid when $\langle b \rangle / \langle s \rangle = F_1 \ll 1$ since $\langle s \rangle = 1/F_0$ [31].

I have outlined above a prescription for calculating the mathematical condition for which NIBA is valid. This means that for a given central system, with certain spectral density function for the environment, one can calculate the quantity F_1 and inspect the regimes in which it is minimised for the various parameters in the model. In subsequent chapters I will perform this calculation explicitly each time NIBA is invoked. For the case of photosynthesis, I have already identified the values of all the relevant parameters, which means a calculation of F_1 will result in a final number for inspection.

Chapter 3

Limiting and perturbative analysis of the 3-site-boson model

Before entering into the full, non-perturbative calculations of the 3-site system plus oscillator bath, I first inspect some of the limiting cases of the model so as to better understand the system. To the same end I also then look at the inclusion of certain parameters perturbatively.

3.1 The central 3-site system

The first case that I look at in detail is that of the 'bare' 3-site system which comprises the central system of interest. It is described as 'bare' as I exclude the oscillator bath for now.

3.1.1 The 3-site-V configuration and population trapping

It is well understood that the addition of a perturbation to the degenerate two state system (with no coupling between states) , gives rise to an avoided crossing in the energy dispersion diagram. This is often discussed in terms of lowered energy eigenstates and thus more stable configurations in chemical physics [118], level repulsion and tunnelling. The fact that the eigenenergy dispersion lines avoid any crossing reflects the fact that an excitation in the system can tunnel between the available eigenstates. This is due to the introduction of a potential energy term that is present even if the states are brought into resonance at zero energy. In certain configurations of 3-level systems; however, the situation is more interesting. Let us consider the Hamiltonian

$$H_3 = \begin{pmatrix} \epsilon + \delta & \Delta_{10} & 0 \\ \Delta_{10} & 0 & \Delta_{20} \\ 0 & \Delta_{20} & \epsilon - \delta \end{pmatrix} \tag{3.1}$$

which describes a 3-site system with the zero energy set at the second site, two different couplings and some detuning between the upper levels. I'll refer to this configuration as a V-system [86, 119]. Finding the eigenvalue expressions for the general case of $\delta \neq 0$ requires solving a cubic equation and produces long, unilluminating expressions. If we set $\delta = 0$ however, one can easily find the eigenenergies to be

$$\lambda_{\pm} = \frac{1}{2}\left(\epsilon \pm \sqrt{\epsilon^2 + 4(\Delta_{10}^2 + \Delta_{20}^2)}\right), \quad \lambda_0 = \epsilon \tag{3.2}$$

With $\delta \neq 0$, a cubic polynomial provides the energies, the exact expressions of which I've chosen not to include here due to their lengthy nature; however, I've included them in Appendix C.

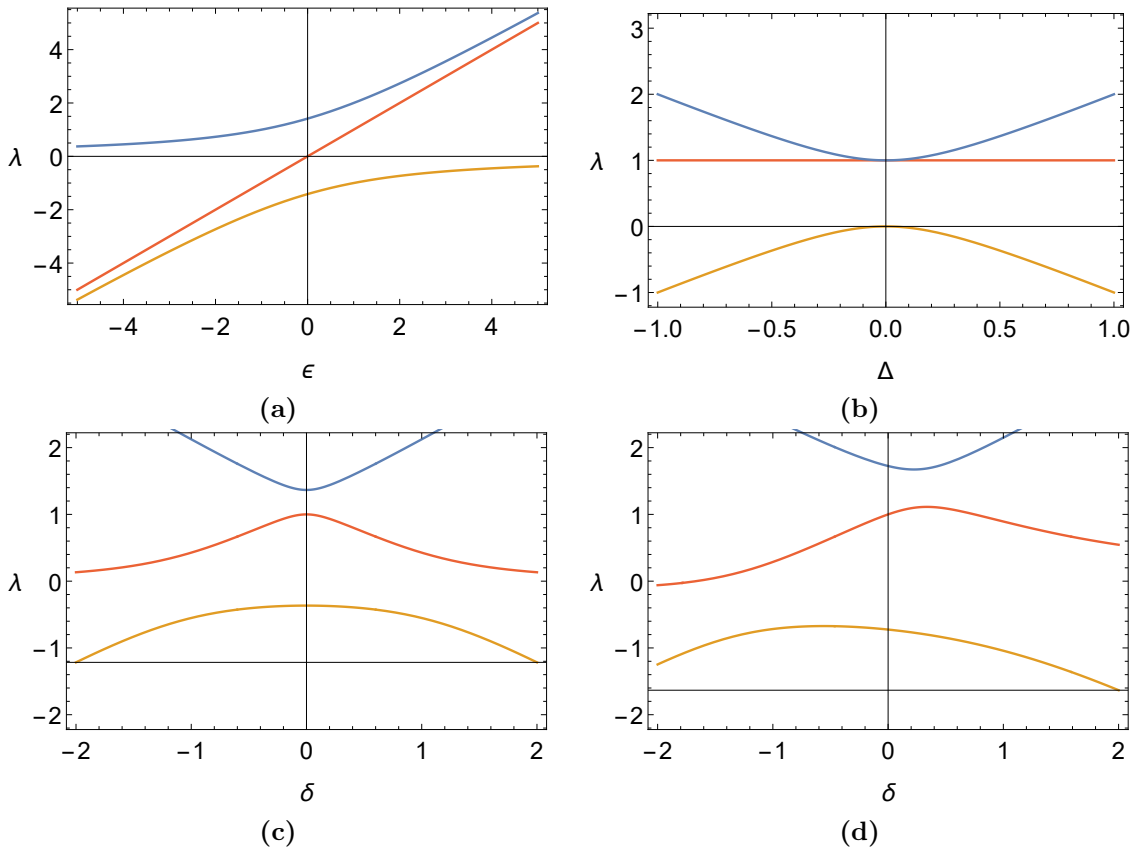

Figure 3.1: Eigenvalues λ_0(red), λ_+(blue), λ_-(orange), as a function of (a) bias energy ϵ for the tuned system where $\epsilon_1 = \epsilon - \delta/2, \epsilon_2 = \epsilon + \delta/2$, (b) tunnelling matrix element separation Δ where $\Delta_{10} = -\Delta/2, \Delta_{20} = \Delta/2$, (c) detuning δ where $\Delta_{10} = 0.5, \Delta_{20} = 0.5$, (d) detuning δ where $\Delta_{10} = 0.5, \Delta_{20} = 1$. In units of ϵ.

We see that the avoided crossing between the two eigenergies $\lambda_{1,2}$ is equal to $4(\Delta_{10}^2+\Delta_{20}^2)$ but there also exists an eigenenergy λ_0 with a linear dispersion. Considering that one could always make a shift in the zero energy, let us refer to this state as the zero energy, a concept often discussed within the field of quantum optics in terms of 2-photon resonance of dressed states [120]. This represents an anti-symmetric coherent superposition of the upper two states with eigenvector

$$\delta = 0: \quad |D\rangle = \frac{1}{\sqrt{\Delta_{10}^2 + \Delta_{20}^2}}\Big(\Delta_{20}\,|1\rangle - \Delta_{10}\,|2\rangle\Big) \tag{3.3}$$

and for completeness I will also include the symmetric combination, often referred to as the 'bright state'

$$\delta = 0: \quad |B\rangle = \frac{1}{\sqrt{\Delta_{10}^2 + \Delta_{20}^2}} \Big(\Delta_{10} |1\rangle + \Delta_{20} |2\rangle \Big) \tag{3.4}$$

The reason this has been ascribed the population trapping state (or dark state) moniker is because even if one considers some decay mode out of the ground state $|0\rangle$, the state $|D\rangle$ never actually 'sees' this decay mode. In other words, as equation 3.3 contains no overlap with the lower-decaying site, any excitation propagating through the system that enters in to this state will remain there. From equation 3.3 we see that, if we start the system of in one of the upper states, for e.g. state $|1\rangle$, then the final long-time population left in the system after $|\pm\rangle$ have decayed, is the overlap of state $|1\rangle$ with the dark-state

$$|\langle 1|D\rangle|^2 = \frac{1}{1 + \left(\frac{\Delta_{10}}{\Delta_{20}}\right)^2} \tag{3.5}$$

We see that the 'trapped' population is maximised for $\Delta_{10} = \Delta_{20}$.

As is the case with the 2-level system, the ratio of the tunnelling elements to bias energies Δ/ϵ describes the general nature of the dynamics. If this ratio is small, then the eigenstates are small deviations from the basis states $|\alpha\rangle$. In the opposite limit, where the bias energies go to zero, the eigenstates are mixtures of the basis states in the system. The resulting eigenstates include the dark-state $|D\rangle$ included above as well as the states

$$|\pm\rangle = \frac{1}{\sqrt{\Delta_{10}^2 + \Delta_{20}^2 + N_+^2}} \Big(\Delta_{10} |1\rangle - N_+ |0\rangle + \Delta_{20} |2\rangle \Big) \tag{3.6}$$

In equation 3.6 one notices the link between $|\pm\rangle$ and the bright-state $|B\rangle$. While the bright-state is not an eigenstate of the 3-site-V-system, it is an eigenstate of the unbiased 2-level system. As $|D\rangle$ remains unchanged upon the introduction of a 3rd state ($|0\rangle$) and a bias energy ϵ, it's the bright state that must split into $|\pm\rangle$ becoming a mixture of the basis states of the 3-basis-states. While in the limit $\epsilon/\Delta \ll 1$, it would be appropriate to cast the 3-site-boson Hamiltonian in the eigenstate basis $\{|D\rangle, |+\rangle, |-\rangle\}$ and solve the system from there. However because we're mostly concerned with the opposite limit, $\epsilon/\Delta \gg 1$, in the application to photosynthesis, we therefore remain in the state basis.

3.1.2 A path-integral formalism for the bare 3-site system

I now develop the path-integral formalism for the bare 3-site system–the isolated central 3-site system without any environment–by first calculating the transition amplitude, or

Greens function [121]. This will form the basis of my analysis using the path integral formalism to include the system-bath coupling both perturbatively and non-perturbatively.

As discussed in Section 2.4.1, the bare amplitudes in the Hamiltonian formalism can be related to the transition amplitudes for the bare system in the path integral formalism [61] by

$$A[\sigma_f, \sigma_i] = \int_{\sigma_i}^{\sigma_f} D\sigma e^{iS_0[\sigma]} = \langle \sigma_f | \, e^{-iH_0 t/\hbar} \, | \sigma_i \rangle \tag{3.7}$$

and then for an unbiased system I rewrite the exponential as an infinite sum

$$\langle \sigma_f | \, e^{-i\hat{H}_0 t} \, | \sigma_i \rangle = \langle \sigma_f | \left(\sum_{n=0}^{\infty} \frac{(-i\hat{H}_0 t/\hbar)^n}{n!} \right) | \sigma_i \rangle \tag{3.8}$$

where I've been careful to identify the fact that $\hat{H}_0$ is in fact an operator. Therefore I've avoided the power series expansion in terms of individual terms within the Hamiltonian due to the non-commutativity of the constituent operators $e^{A+B} \neq e^A e^B$ for $[A, B] \neq 0$. Instead we inspect the even and odd power contributions to equation 3.8,

$$A[\sigma_f, \sigma_i; t] = \langle \sigma_f | \left(\sum_{n=0}^{\infty} \frac{(-i\hat{H}_0 t/\hbar)^{2n}}{(2n)!} + \sum_{n=0}^{\infty} \frac{(-i\hat{H}_0 t/\hbar)^{2n+1}}{(2n+1)!} \right) | \sigma_i \rangle \tag{3.9}$$

I find

$$A[\sigma_f, \sigma_i; t] = \langle \sigma_f | \left(1 + \sum_{n=1}^{\infty} (\Delta_{10}^2 + \Delta_{20}^2)^{n-1} \frac{(-it)^{2n}}{(2n)!} (\hat{H}_0)^2 + \sum_{n=0}^{\infty} (\Delta_{10}^2 + \Delta_{20}^2)^n \frac{(-it)^{2n+1}}{(2n+1)!} \hat{H}_0 \right) | \sigma_i \rangle \tag{3.10}$$

where for the unbiased system

$$H_0 = \begin{pmatrix} 0 & \Delta_{10} & 0 \\ \Delta_{10} & 0 & \Delta_{20} \\ 0 & \Delta_{20} & 0 \end{pmatrix}, \quad (H_0)^2 = \begin{pmatrix} \Delta_{10}^2 & 0 & \Delta_{10}\Delta_{20} \\ 0 & \Delta_{10}^2 + \Delta_{20}^2 & 0 \\ \Delta_{10}\Delta_{20} & 0 & \Delta_{20}^2 \end{pmatrix} \tag{3.11}$$

The bare amplitude can then be rewritten as an infinite series of products of time-intervals. For the $A_{11}(t)$ element this reads

$$A_{11}(t) = 1 + \Delta_{10}^2 \sum_{n=1}^{\infty} (-i)^{2n} (\Delta_{10}^2 + \Delta_{20}^2)^{n-1} \int_0^t dt_{2n} \int_0^{t_{2n}} dt_{2n-1} ... \int_0^{t_2} dt_1 \tag{3.12}$$

Once I consider the full system, including the effects of the bath by way of the influence

functional, I'll proceed with the analysis by way of taking Laplace transforms. Here I preemptively take the Laplace transform of 3.12 and also check the method against a simple matrix inversion to calculate the Greens function

$$A_{11}(\lambda) = \frac{1}{\lambda} + \Delta_{10}^2 \sum_{n=1}^{\infty} (-i)^{2n} (\Delta_{10}^2 + \Delta_{20}^2)^{n-1} \mathscr{L} \left[\int_0^t dt_{2n} \int_0^{t_{2n}} dt_{2n-1} ... \int_0^{t_2} dt_1 \right] \tag{3.13}$$

which yields

$$A_{11}(\lambda) = \frac{1}{\lambda} + \Delta_{10}^2 \sum_{n=1}^{\infty} (-i)^{2n} \left(\Delta_{10}^2 + \Delta_{20}^2 \right)^{n-1} \frac{1}{\lambda^{2n+1}} \tag{3.14}$$

and the summation can be performed to give

$$A_{11}(\lambda) = \frac{\lambda^2 + \Delta_{20}^2}{\lambda^3 + \lambda(\Delta_{10}^2 + \Delta_{20}^2)} \tag{3.15}$$

The inverse-Laplace transform yields the dynamics

$$A_{11}(t) = \frac{\Delta_{20}^2 + \Delta_{10}^2 \cos\left(\sqrt{\Delta_{10}^2 + \Delta_{20}^2} t \right)}{\Delta_{10}^2 + \Delta_{20}^2} \tag{3.16}$$

It's worth remarking at this point that the $(\Delta_{10}^2 + \Delta_{20}^2)^{n-1}$ term arises due to the ambiguity as to whether the system flips in either branch. This is where we pick up the above superposition of Δ_{10}^2 and Δ_{20}^2 terms due to the summation over both outcomes, $n-1$ times, until we reach the final state.

To check our result here we can compare to the calculation of the bare 3-site Greens function by simple matrix inversion

$$A_{\sigma,\sigma'}(\lambda) = \langle \sigma | \left(\frac{1}{\lambda \mathbb{1} + i\hat{H}_0} \right) | \sigma' \rangle \tag{3.17}$$

where the $A_{11}(\lambda)$ element is given by

$$A_{11}(\lambda) = \begin{vmatrix} \lambda & -i\Delta_{10} & 0 \\ -i\Delta_{10} & \lambda & -i\Delta_{20} \\ 0 & -i\Delta_{20} & \lambda \end{vmatrix}^{-1} \begin{vmatrix} \lambda & -i\Delta_{20} \\ -i\Delta_{20} & \lambda \end{vmatrix} \tag{3.18}$$

which does indeed give equation 3.15 confirming the above formulation of the 3-site path

integral.

The simplest case, which is useful to note here for future calculations, is the ground-state propagator

$$A_{00}(\lambda) = \frac{1}{\lambda} + \sum_{n=1}^{\infty}(-i)^{2n}(\Delta_{10}^2 + \Delta_{20}^2)^n \mathscr{L}\left[\int_0^t dt_{2n}\int_0^{t_{2n}} dt_{2n-1}...\int_0^{t_2} dt_1\right] \tag{3.19}$$

which gives

$$A_{00}(\lambda) = \frac{\lambda}{\lambda^2 + (\Delta_{10}^2 + \Delta_{20}^2)} \tag{3.20}$$

and

$$A_{00}(t) = \cos\left(\sqrt{\Delta_{10}^2 + \Delta_{20}^2}t\right) \tag{3.21}$$

Now I would like to complete the bare-system by adding the biases ϵ_1 and ϵ_2. The introduction of the kinetic energy term is using the Suzuki-Trotter decomposition of the propagator [117]. The simplest way to proceed is to add the appropriate bias terms to equation 3.13 and explain the physical basis for each term

$$A_{11}(\lambda) = \frac{1}{\lambda + i\epsilon_1} + \Delta_{10}^2\sum_{n=1}^{\infty}(-i)^{2n}\mathscr{L}\Bigg[\int_0^t dt_{2n}e^{-i\epsilon_1(t-t_{2n})}\int_0^{t_{2n}} dt_{2n-1}$$
$$\int_0^{t_{2n-1}} dt_{2n-2}\left(\Delta_{10}^2 e^{-i\epsilon_1(t_{2n-1}-t_{2n-2})} + \Delta_{20}^2 e^{-i\epsilon_2(t_{2n-1}-t_{2n-2})}\right)\int_0^{t_{2n-2}} dt_{2n-3}...\int_0^{t_2} dt_1 e^{-i\epsilon_1(t_2-t_1)}\Bigg] \tag{3.22}$$

The first term represents the free-particle Greens function: the transition amplitude for the system to remain in state $|1\rangle$ stipulated by the initial conditions. The second term, which contains all higher order processes, begins with a transition matrix element Δ_{10}^2, coming from the initial and final conditions. The system starts and ends in state $|1\rangle$, therefore with one or more flips in the system, there will at least be two coming from the left branch so as to bring the system back again. So we see that the $n = 1$ term satisfies this condition, and only contains the propagator for state $|1\rangle$ integrated over one intermediate time interval that lets the system sit in state $|0\rangle$ for some time (weighted by unity since $\epsilon_0 = 0$) and then return to $|1\rangle$. All higher order terms contain $n - 1$ of the superposition $(\Delta_{10}^2\exp[-\epsilon_1(t_{2n-1} - t_{2n-2})] + \Delta_{20}^2\exp[-\epsilon_2(t_{2n-1} - t_{2n-2})])$. This comes

from the fact that whenever the system enters the lower site $|0\rangle$, it has the option to either subsequently flip in either branch. We also see that there will be n contributions from the number of times the system visits site $|3\rangle$, which will show up as a $1/\lambda^n$ term in the Laplace transform. A sum over all possible paths will include any combination of these processes, i.e. the system should be allowed to propagate as many times as it likes in either branch and with any possible combination of flips in both branches. Computing the Laplace transform I find

$$A_{11}(\lambda) = \frac{1}{\lambda + i\epsilon_1} + \Delta_{10}^2 \sum_{n=1}^{\infty} (-i)^{2n} \left(\frac{1}{\lambda + i\epsilon_1}\right)^2 \left(\frac{\Delta_{10}^2}{\lambda + i\epsilon_1} + \frac{\Delta_{20}^2}{\lambda + i\epsilon_2}\right)^{n-1} \frac{1}{\lambda^n} \tag{3.23}$$

and computing the series summation then gives

$$A_{11}(\lambda) = \frac{\lambda(\lambda + i\epsilon_2) + \Delta_{20}^2}{\lambda(\lambda + i\epsilon_1)(\lambda + i\epsilon_2) + (\lambda + i\epsilon_1)\Delta_{20}^2 + (\lambda + i\epsilon_2)\Delta_{10}^2} \tag{3.24}$$

For the case where the upper two levels are 'tuned' such that $\epsilon_1 = \epsilon_2$, the transition amplitude can be inverse Laplace transformed to give

$$\begin{aligned} A_{11}(t) = {} & \frac{\Delta_{20}^2 e^{it\epsilon}}{\Delta_{10}^2 + \Delta_{20}^2} + \frac{2\Delta_{10}^2 e^{\frac{it\epsilon}{2} - \frac{1}{2}it\sqrt{4\Delta_{10}^2 + 4\Delta_{20}^2 + \epsilon^2}}}{\sqrt{4\Delta_{10}^2 + 4\Delta_{20}^2 + \epsilon^2}\left(\sqrt{4\Delta_{10}^2 + 4\Delta_{20}^2 + \epsilon^2} + \epsilon\right)} \\ & + \frac{2\Delta_{10}^2 e^{\frac{1}{2}it\sqrt{4\Delta_{10}^2 + 4\Delta_{20}^2 + \epsilon^2} + \frac{it\epsilon}{2}}}{\sqrt{4\Delta_{10}^2 + 4\Delta_{20}^2 + \epsilon^2}\left(\sqrt{4\Delta_{10}^2 + 4\Delta_{20}^2 + \epsilon^2} - \epsilon\right)} \end{aligned} \tag{3.25}$$

Once again we can check this result against a simple matrix inversion which does indeed produce equation 3.24, confirming our procedure for the biased case as well.

I similarly calculate the ground state propagator

$$A_{00}(\lambda) = \frac{1}{\lambda} + \sum_{n=1}^{\infty} (-i)^{2n} \left(\frac{\Delta_{10}^2}{\lambda + i\epsilon_1} + \frac{\Delta_{20}^2}{\lambda + i\epsilon_2}\right)^n \frac{1}{\lambda^{n+1}} \tag{3.26}$$

which yields

$$A_{00}(\lambda) = \frac{(\lambda + i\epsilon_1)(\lambda + i\epsilon_2)}{\lambda(\lambda + i\epsilon_1)(\lambda + i\epsilon_2) + (\lambda + i\epsilon_1)\Delta_{20}^2 + (\lambda + i\epsilon_2)\Delta_{10}^2} \tag{3.27}$$

3.1.3 Population trapping in a 3-site-V system

In this section I would like to demonstrate the phenomenon of population trapping in the dynamics of the 3-site-V system. The simplest way to do this, is by considering a decay channel coupled only to the ground state $|3\rangle$ that manifests from an environment with a white-noise spectrum [61]. This represents a form of irreversible decay [120] from the system. For this, the Greens function is

$$A_{11}(\lambda) = \frac{(\lambda+\Gamma)(\lambda+i\epsilon_2)+\Delta_{20}^2}{(\lambda+\Gamma)(\lambda+i\epsilon_1)(\lambda+i\epsilon_2)+(\lambda+i\epsilon_1)\Delta_{20}^2+(\lambda+i\epsilon_2)\Delta_{10}^2} \tag{3.28}$$

and the configuration with the introduction of the sink is depicted in Figure 3.2

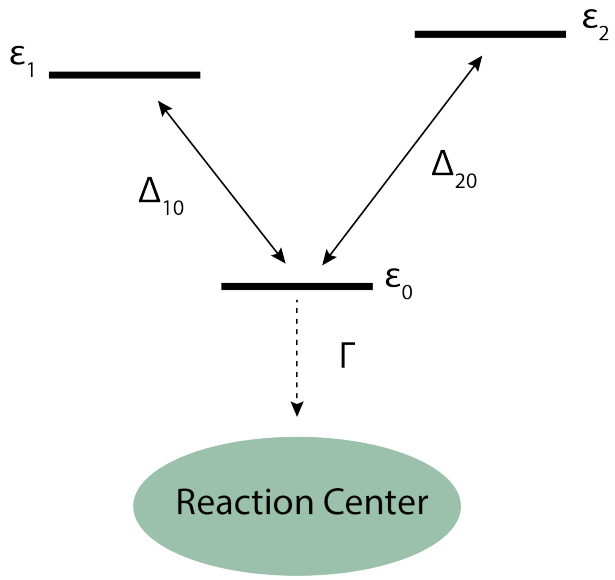

Figure 3.2: Diagrammatic representation of 3-site-V model coupled to a sink via an irreversible decay channel from the ground state

As before I calculate the inverse-Laplace transform to find the time-domain amplitude. Then the probability to start and return to site one can be calculated from

$$P_{11}(t) = K_{11;11}(t)\rho_{11}(0) \tag{3.29}$$

where the density matrix propagator is

$$K_{11;11}(t) = A_{11}^*(t)A_{11}(t) \tag{3.30}$$

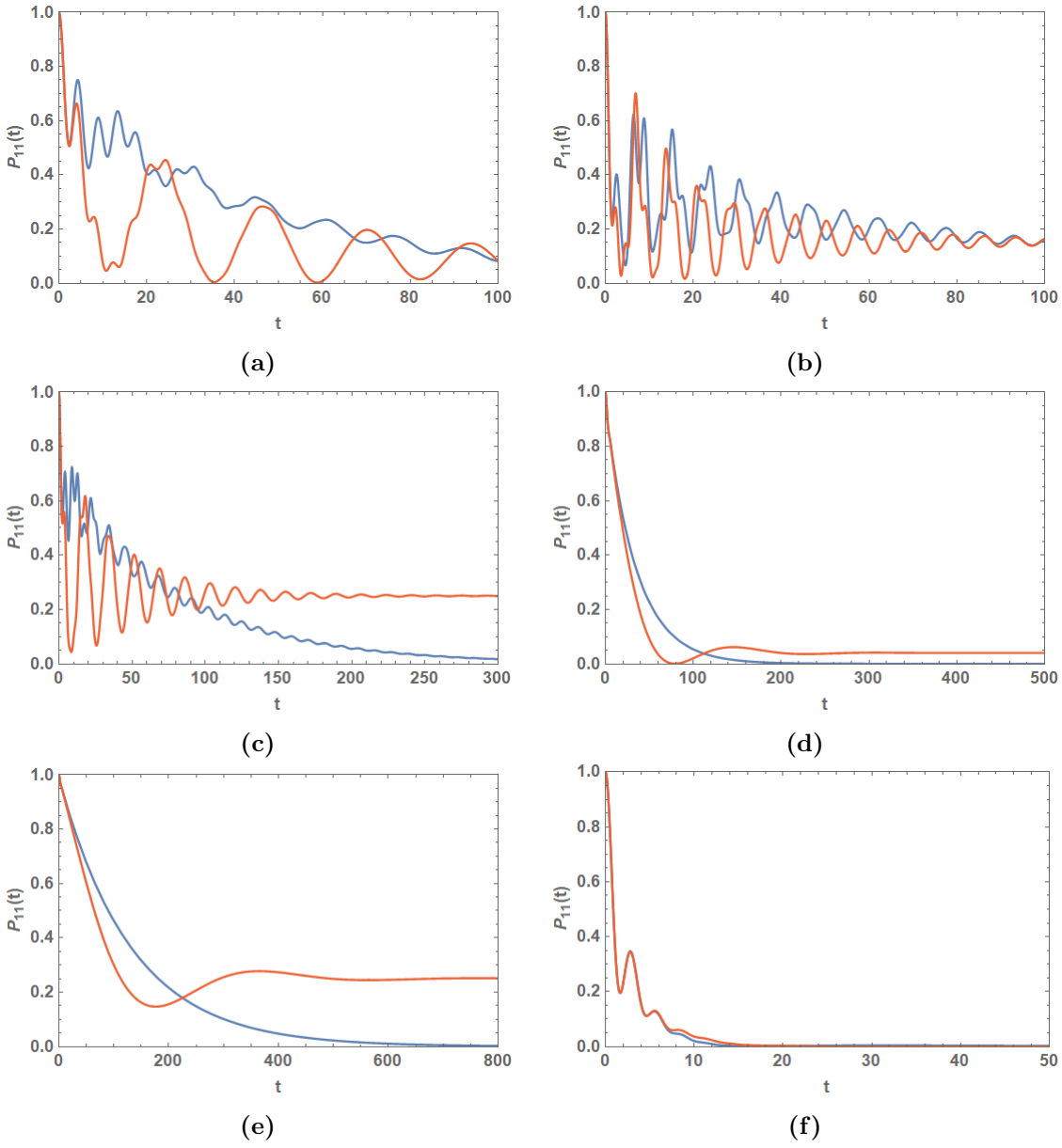

Figure 3.3: Return probability to site 1: $P_{11}(t)$, as a function of time for tuned (red) and detuned (blue) cases. In units of $\epsilon_1 = 1$. $\epsilon_2 = 1.5\epsilon_1$(blue), $\epsilon_2 = \epsilon_1 = 1$(red). (a): $\Gamma = 0.1$, $\Delta_{10} = 0.5$, $\Delta_{20} = 0.3$, (b): $\Gamma = 0.1$, $\Delta_{10} = 1$,$\Delta_{20} = 0.8$, (c): $\Gamma = 0.1$, $\Delta_{10} = 0.5$,$\Delta_{20} = 0.5$, (d): $\Gamma = 0.5$, $\Delta_{10} = 0.2$,$\Delta_{20} = 0.1$, (e): $\Gamma = 0.5$, $\Delta_{10} = 0.1$,$\Delta_{20} = 0.1$, (f): $\Gamma = 0.5$, $\Delta_{10} = 1$,$\Delta_{20} = 0.1$

In Figure 3.3 we see the return probabilities to site 1 for various areas of the parameter space. The blue line corresponds to the detuned system with a $\delta = 0.25$ and the red lines the tuned case with $\delta = 0$. The irreversible decay from state 0 is quantified in the rate Γ.

For the underdamped case, where Γ is sufficiently small to permit the system to execute various cycles, we see damped coherent oscillations in the dynamics. The beat signals characteristic of the two interfering frequencies in the 3-site system are present in the underdamped case and visible for a few cycles (see Figures 3.3b and 3.3c). However the beats are evidently suppressed after a few cycles. Population trapping is visible in the underdamped cases with the tuned (red) lines maintaining some asymptotic occupation probability for long times, while the detuned case (blue), decays eventually.

The efficacy of the population trapping effect is evident even in the overdamped case (see Figures 3.3d and 3.3e), where the system is unable to even complete one cycle in the detuned case, while the tuned case makes it through about one cycle before settling in to the 'dark state'. Furthermore we see the effect of tuned tunnelling matrix elements on the dynamics. In the underdamped case, Figure 3.3b, demonstrates the complimentary effect that the tuning of the tunneling energy has on population trapping. We see that it leaves the tuned system with increased occupation probability at long times. This effect is also clearly visible in the overdamped regime too (see Figure 3.3d). We can also see the destruction of the dark-state properties of the system when the second tunnelling matrix element Δ_{20} of the system is too small relative to the decay Γ out of site-3, and the system is unable to enter into dark-state. Here we see that the long-time population decays to zero in a similar fashion to the 2-state system where population trapping is absent.

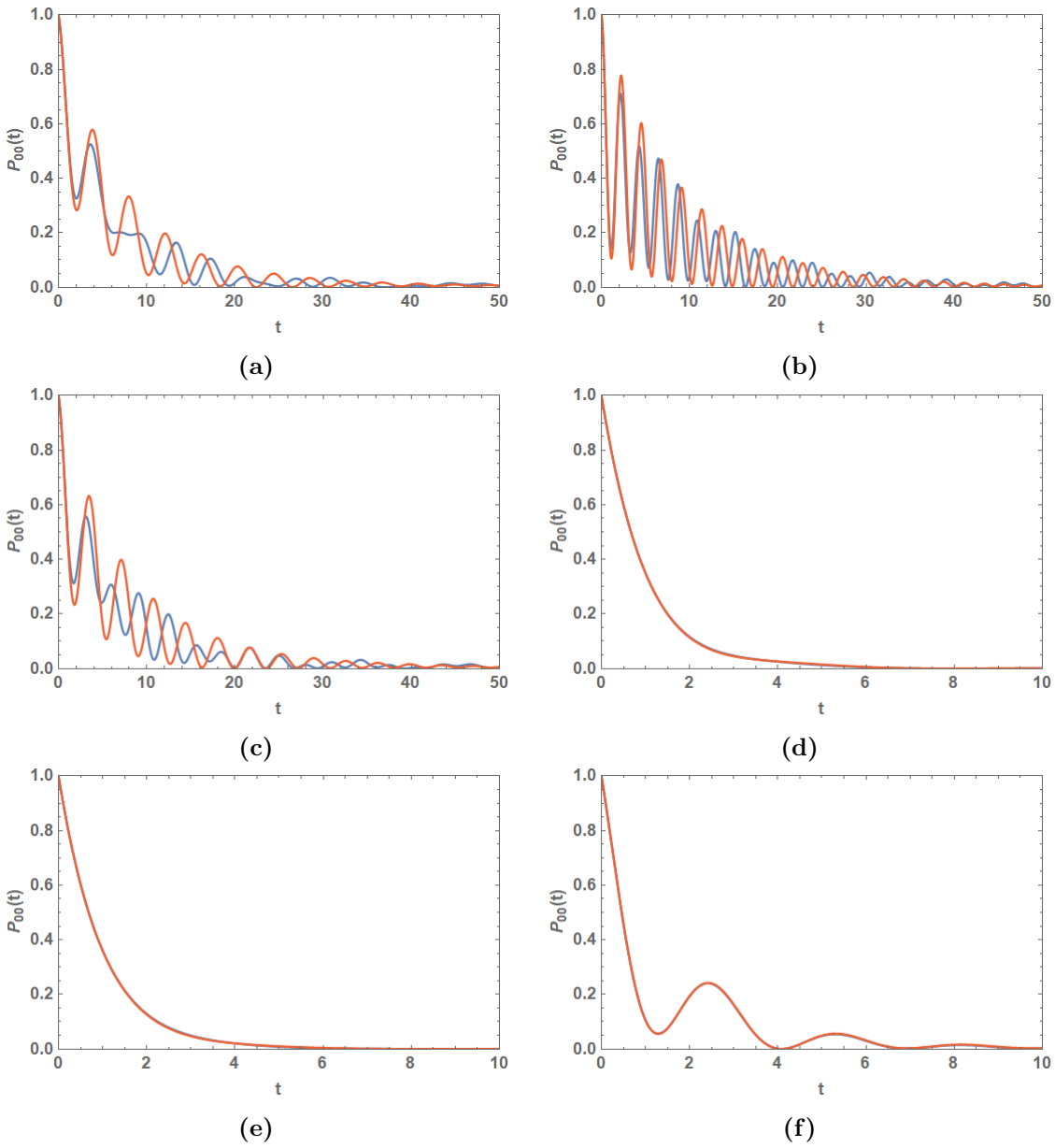

Figure 3.4: Return probability to ground state $|0\rangle$: $P_{00}(t)$, as a function of time for tuned (red) and detuned (blue) cases. In units of $\epsilon_1 = 1$. $\epsilon_2 = 1.5\epsilon_1$(blue),$\epsilon_2 = \epsilon_1 = 1$(red). (a): $\Gamma = 0.1$, $\Delta_{10} = 0.5$, $\Delta_{20} = 0.3$, (b): $\Gamma = 0.1$, $\Delta_{10} = 1$,$\Delta_{20} = 0.8$, (c): $\Gamma = 0.1$, $\Delta_{10} = 0.5$,$\Delta_{20} = 0.5$, (d): $\Gamma = 0.5$, $\Delta_{10} = 0.2$,$\Delta_{20} = 0.1$, (e): $\Gamma = 0.5$, $\Delta_{10} = 0.1$,$\Delta_{20} = 0.1$, (f): $\Gamma = 0.5$, $\Delta_{10} = 1$,$\Delta_{20} = 0.1$

In Figure 3.4 I calculate the ground-state dynamics $P_{00}(t)$ for the same parameters as the $P_{11}(t)$ dynamics of Figure 3.3. We immediately notice how the ground state is

unaffected by the dark-state occupancy, considering that it has no overlap with $|D\rangle$. The tuned biases do however introduce a phase-shift in the dynamics as can be seen in Figures 3.4a,3.4b, 3.4c. In accordance with this, the dynamics decay faster, and coherent oscillations persist for shorter times. Coherent oscillations are entirely washed out for a strong ground-state-decay rate relative to the tunnelling matrix elements, and we are in the fully incoherent regime.

The other limit of interest within the biased regime is that of small bias relative to tunnelling matrix element. In this regime we expect the tunnelling terms to dominate, such that we observe strong coherent oscillations persisting as well as beat frequencies arising from the interference of the two branches.

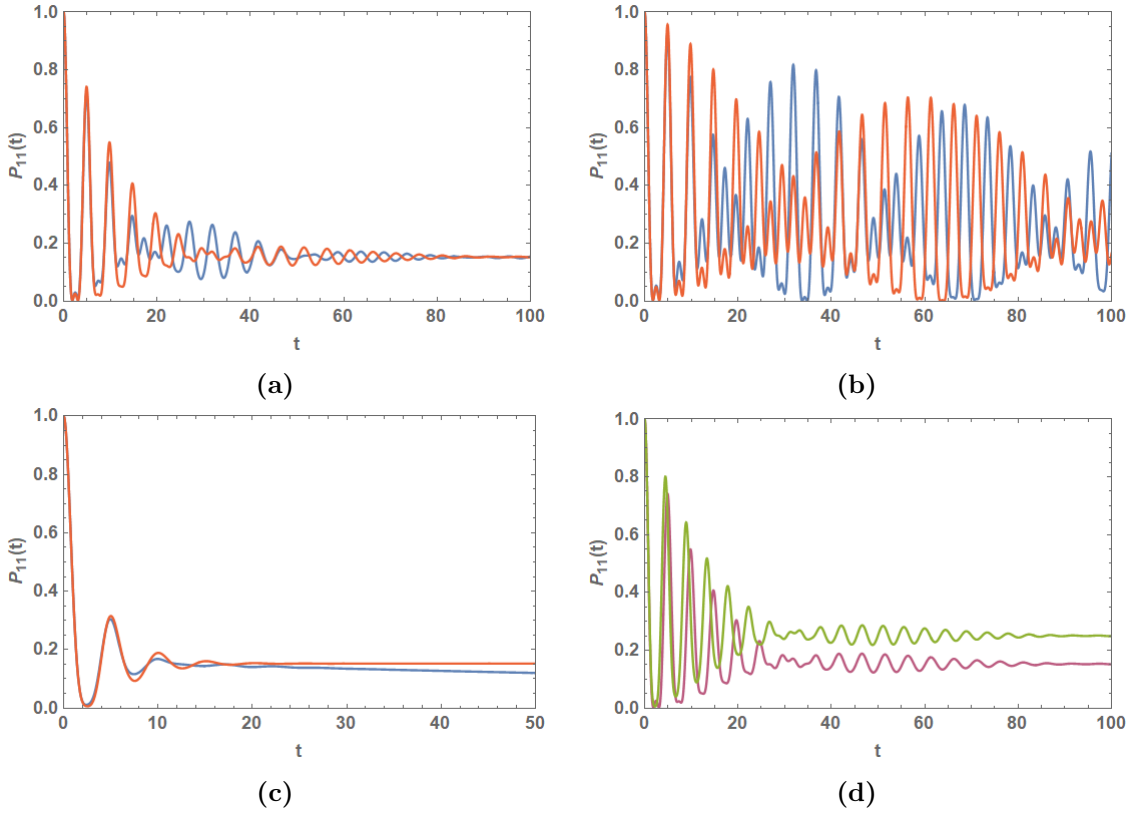

Figure 3.5: Return probability to state $|1\rangle$: $P_{11}(t)$, as a function of time for tuned biases (red) and detuned biases (blue), as well as tuned tunnelling (green) and detuned tunnelling (purple), in the small bias regime. $\epsilon_2 = 0.2, \epsilon_1 = 0.1$ (blue), $\epsilon_2 = \epsilon_1 = 0.1$(red). (a): $\Gamma = 0.1$, $\Delta_{10} = 1$, $\Delta_{20} = 0.8$, (b): $\Gamma = 0.01$, $\Delta_{10} = 1$,$\Delta_{20} = 0.8$, (c): $\Gamma = 0.5$, $\Delta_{10} = 1$,$\Delta_{20} = 0.8$, (d): $\Gamma = 0.5$, $\Delta_{10} = 0.2$,$\Delta_{20} = 0.1$, (e): $\Gamma = 0.1$, $\Delta_{10} = 1$,$\Delta_{20} = 0.8$

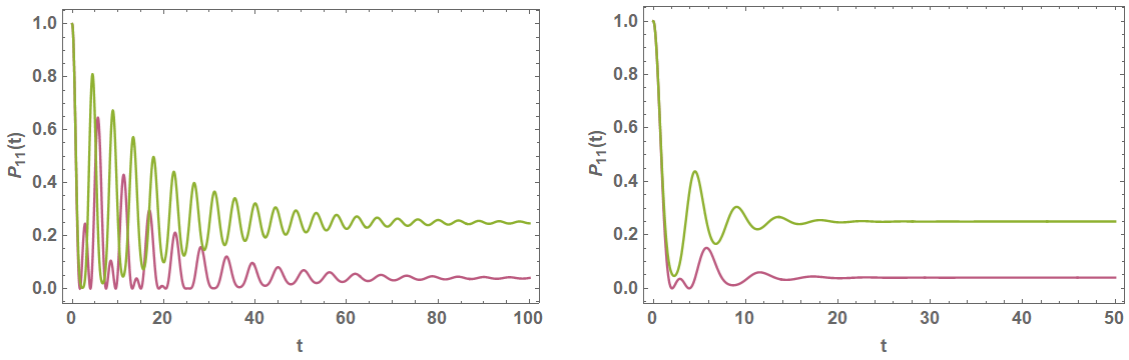

(a) **(b)**

Figure 3.6: Return probability to site 1 for unbiased system. $\Delta_{10} = 1$, $\Delta_{20} = 0.5$ (purple), $\Delta_{10} = 1$, $\Delta_{20} = 1$(green). (a): $\Gamma = 0.1$, (b): $\Gamma = 0.5$

We see from the unbiased plots in Figure 3.6 the presence of the zero energy 'dark-state' eigenvalue $\lambda = 0$ in the long-time population trapping. The effect of tuning the transition matrix elements to aid in population trapping is also evident even in the case of strong dissipation.

From the perspective of population trapping, it is instructive to investigate the long time dynamics $P_{11}(t \to \infty)$.

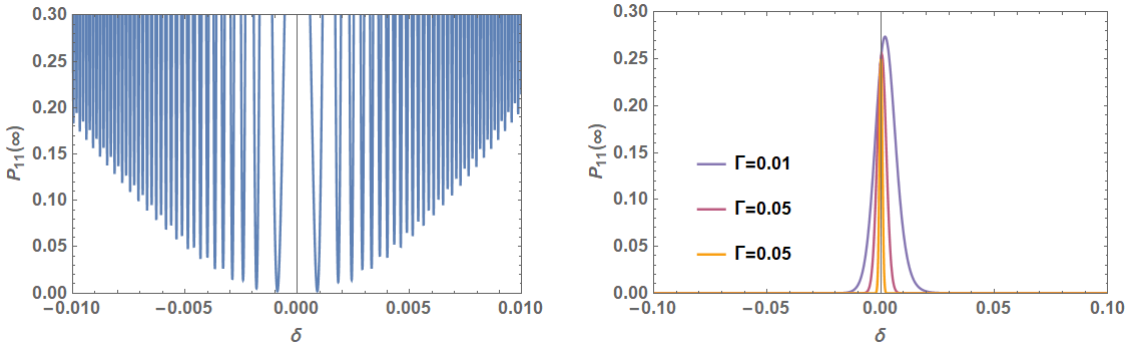

(a) **(b)**

Figure 3.7: Return probability to site 1 at $t \to \infty$: $P_{11}(\infty)$, as a function of detuning $\delta = \epsilon_1 - \epsilon_2$. $\Delta_{10} = \Delta_{20} = 0.1$, $\epsilon = 1$ (a) $\Gamma = 0$ (Bath off) (b) Dark-state peak for various decay rates

For the case of zero-decay rate to the reservoir 3.7a, we see how the detuning parameter δ introduces a phase shift in the dynamics. In the incoherent regime, with non-zero decay to the reservoir, we see the effect that continuously varying the detuning has on

P_{11} for long times. For large detuning, again we see how for large level asymmetry (large detuning), the system fails to leave $|1\rangle$. This is symptomatic of a large level-spacing leading to localisation and not population trapping. For small detuning, the system is well within the parameter regime for the 3-site model. For small, but non-zero δ, the system is depleted due to Γ and there is no state 1 population for long times. For $\delta \to 0$ however, the system enters in to the dark state and population remains for long times, indicated by the peak in Figure 3.7a.

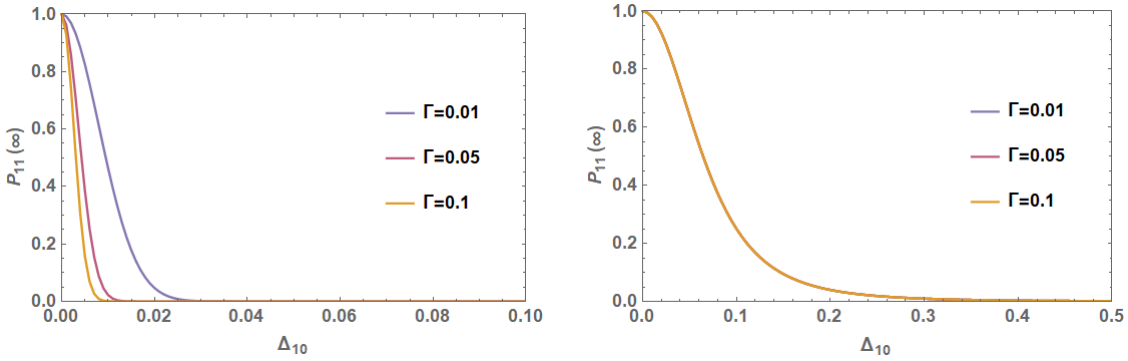

(a) **(b)**

Figure 3.8: Long time return probability $P_{11}(\infty)$ to site 1 vs Δ_{10}: $\Delta_{20} = \Delta_{20} = 0.1$, $\epsilon = 1$; (a) $\delta = 1$ (b) $\delta = 0$

3.2 Weak system-bath coupling regime for the 3-site-V system

If the system bath couplings are small then I can perform perturbation theory in the ratio $u_{\alpha q} = \lambda_\alpha/\omega_q$. Here I apply the Lang-Firsov polaron transformation [52] to the bare 3-site Hamiltonian coupled diagonally to an oscillator bath, which decouples the central system from the bath. To do this I define the unitary operator $U = e^S$, where $S = -\sum_{\alpha q} u_{\alpha q}(b_q - b_q^\dagger)\,|\alpha\rangle\langle\alpha|$ and $u_{\alpha q} = \lambda_{\alpha q}/\omega_q$ such that $H \to UHU^\dagger = e^S H e^{-S}$. Physically, this represents the shifting of the boson cloud to its new equilibrium position. So S can be thought of as a shift operator, for the diagonal system-bath interaction. Applying this transformation, and using the Baker-Campbell-Hausdorff formula, yields

$$\tilde{H} = \epsilon_1 |1\rangle\langle 1| + \epsilon_2 |2\rangle\langle 2| + \epsilon_0 |0\rangle\langle 0| \\ + \Delta_{10}\Big(|1\rangle\langle 0| B_{10} + |0\rangle\langle 1| B_{01}\Big) + \Delta_{20}\Big(|2\rangle\langle 0| B_{20} + |0\rangle\langle 2| B_{02}\Big) + H_B \tag{3.31}$$

where $B_{\alpha\beta} = \exp(\phi_\alpha - \phi_\beta)$, $\phi_\alpha = \sum_q u_{\alpha q}(b_q - b_q^\dagger)$ and a constant $(-1)\sum_q u_{\alpha q}\lambda_{\alpha q} |\alpha\rangle\langle\alpha|$ has also been dropped in $\tilde{H}$ such that the zero energy has been shifted accordingly[1]. Since the bath is decoupled from the central system via the polaron transformation, I can calculate the ground-state density matrix propagator of $\tilde{H}$ via

$$\tilde{K}_{00;00}(t) = \langle \tilde{A}_{00}(t)\tilde{A}^*_{00}(t)\rangle_B \tag{3.32}$$

where the statistical average is over the bath coordinates and I assume that the initial density matrix components for the bath and central system factorise at $t = 0$ such that $\rho(0) = \rho_S(0) \otimes \rho_B(0)$. Since the transformation has decoupled the bath from the central system, I can infer the transition amplitude $\tilde{A}(t)$ for the transformed Hamiltonian $\tilde{H}$, from the form determined in Section 3.1.2. Now each tunneling matrix element also contains a corresponding term $B_{\alpha\beta}$ that shifts the boson cloud as well. I present the form for the unbiased transformed Greens function here for brevity

$$A_{00}(t) = 1 + \sum_{n=1}^{\infty}(-i)^{2n}\int_0^t dt_{2n}\int_0^{t_{2n}} dt_{2n-1}\Big[\Delta_{10}^2 B_{10}(t_{2n})B_{01}(t_{2n-1}) + \Delta_{20}^2 B_{20}(t_{2n})B_{02}(t_{2n-1})\Big] \\ \times ... \int_0^{t_2} dt_1\Big[\Delta_{10}^2 B_{10}(t_2)B_{01}(t_1) + \Delta_{20}^2 B_{20}(t_2)B_{02}(t_1)\Big] \tag{3.33}$$

Therefore the ground-state-density-matrix propagator is

$$K_{00;00}(t) = \Big\langle 1 - \int_0^t dt_2\int_0^{t_2} dt_1\Big[k_{10}(t_1,t_2) + k_{20}(t_1,t_2)\Big] \\ + \int_0^t dt_4\int_0^{t_4} dt_3\int_0^{t_3} dt_2\int_0^{t_2} dt_1\Big[k_{10}(t_1,t_2)k_{10}(t_3,t_4) + k_{10}(t_1,t_2)k_{20}(t_3,t_4) \\ + k_{20}(t_1,t_2)k_{10}(t_3,t_4) + k_{20}(t_1,t_2)k_{20}(t_3,t_4)\Big] + ...\Big\rangle_B \tag{3.34}$$

[1]I can rewrite the shift operators in terms of the momentum operator $\phi_\alpha = \sum_q (x_\alpha c_q/m_q\omega_q^2)\hat{p}_\alpha$ where we can see more explicitly how the transformation serves to displace the oscillators about the distance $x_\alpha - x_\beta$, corresponding to the separation between wells

where the kernels

$$k_{\alpha\beta}(t,t') = \frac{\Delta^2_{\alpha\beta}}{2}\Big[B_{\alpha\beta}(t)B_{\beta\alpha}(t') + B_{\beta\alpha}(t)B_{\alpha\beta}(t')\Big] \tag{3.35}$$

describe the 'blips' in the system, in the language of the spin-boson model. The terms $B_{\alpha\beta}(t)$ are the shift operators for the bath modes. They move the bosons between the potential minima in the system and are dependent on the system-bath coupling, and the temperature of the bath.

The statistical average over the bath modes leads to the coupled-bath correlation functions containing the coupled-boson propagator, which I introduce shortly. We see that in the general case of equation 3.34 above, where blip interactions can be long range in time, that we have all higher order combinations of blip-blip interactions in the full summation. Since we're operating in the weak-coupling limit, and the shift operators $B_{\alpha\beta}(t)$ are functions of the dimensionless coupling parameter $u_{\alpha q}$, we can partially sum this series by only including the zeroth order blip interaction, i.e. the self-interaction of the blip. Blip-blip interactions contain terms that are higher order in $u_{\alpha q}$ and are therefore neglected. All of this is suggestive of a physical description of the situation that involves the bath rapidly measuring the state of the system and thereby suppressing coherent states within it. A blip–as discussed in the context of the spin-boson model– represents an off-diagonal excursion within the reduced density matrix of the central system. In the current formalism it takes the equivalent form of a tunnelling process (back and forth between wells) that interacts with the bath along the way. With this in mind the partial re-summation is

$$\begin{aligned}\tilde{K}_{00;00}(t) = 1 + \sum_{n=1}^{\infty}(-i)^{2n}\int_0^t dt_{2n}\int_0^{t_{2n}} dt_{2n-1}\Big(\Sigma_{10}(t_{2n},t_{2n-1}) + \Sigma_{20}(t_{2n},t_{2n-1})\Big)\int_0^{t_{2n-1}} dt_{2n-2} \\ \times \ldots \int_0^{t_3} dt_2 \int_0^{t_2} dt_1\Big(\Sigma_{10}(t_2,t_1) + \Sigma_{20}(t_2,t_1)\Big)\end{aligned} \tag{3.36}$$

where

$$\Sigma_{\alpha\beta}(t,t') = \frac{\Delta^2_{\alpha\beta}}{2}\Big[e^{-i(\epsilon_\alpha-\epsilon_\beta)(t-t')/\hbar}\Big\langle B_{\alpha\beta}(t)B_{\beta\alpha}(t')\Big\rangle_B + e^{i(\epsilon_\alpha-\epsilon_\beta)(t-t')/\hbar}\Big\langle B_{\beta\alpha}(t)B_{\alpha\beta}(t')\Big\rangle_B\Big] \tag{3.37}$$

and the bias terms have been reintroduced. Since I have decoupled the bath from the

central system, what I have here is a similar situation to the bare-3-site model of Section 3.1.2. The system can flip in either transition and return to the ground state each time, but now each time the system flips, it displaces the bath and drags a 'cloud' of bosons with it. This is accounted for by the averages $\langle B_{\alpha\beta}(t)B_{\alpha\beta}(t')\rangle$ which displace the boson-cloud to site α at time t and then back to site β at time t'. The bath correlator $\Sigma(t,t')$ includes both the forwards and backwards paths due to the density matrix formalism.

Implicit in the analysis so far is the assumption that bath correlations die off for long times, which is why I have only included nearest-neighbour-bath correlations. This is equivalent to the application of NIBA [99]. I will also investigate the regions of validity of this approximation later on in this chapter. Computing the Laplace transforms to solve the system yields

$$\tilde{K}_{00;00}(\lambda) = \frac{1}{\lambda} + \sum_{n=1}^{\infty}(-i)^{2n}\Big(\Sigma_{10}(\lambda) + \Sigma_{20}(\lambda)\Big)^n \frac{1}{\lambda^{n+1}} \tag{3.38}$$

where the self-energies are

$$\Sigma_{\alpha\beta}(t,t') = \Delta_{\alpha\beta}^2\langle \mathbb{B}_{\alpha\beta}\rangle\langle \mathbb{B}_{\beta\alpha}\rangle \cos\big[(\epsilon_\alpha - \epsilon_\beta)(t-t')/\hbar\big] e^{\varphi_{\alpha\beta}(t-t')} \tag{3.39}$$

and $\langle \mathbb{B}_{\alpha\beta}\rangle$ give rise to the Debye-Waller factor that renormalises the tunnelling energy ([99]) $\tilde{\Delta}_{\alpha\beta} = \Delta_{\alpha\beta}\sqrt{\langle \mathbb{B}_{\alpha\beta}\rangle\langle \mathbb{B}_{\beta\alpha}\rangle}$. This term represents the adiabatic renormalisation of the tunnelling energy due to high-frequency bath modes much greater than the tunnelling frequency. The bath correlations are contained in the second, exponential term, whose expansion contains all possible diagrams of electron-boson interaction. The phase factor is given by the well-known coupled phonon propagator [52]

$$\varphi_{\alpha\beta}(t) = \sum_q (u_{\alpha q} - u_{\beta q})^2 \Big[n_q\left(1 - e^{i\omega_q t}\right) + (1+n_q)\left(1 - e^{-i\omega_q t}\right)\Big] \tag{3.40}$$

with the Bose occupation numbers $n_q = (e^{\beta\omega_q} - 1)^{-1}$, and the dimensionless coupling parameter $u_{\alpha q} = \lambda_{\alpha q}/\omega_q$. In Appendix B I show how in the continuum limit, the phase is equivalent to

$$\varphi_{\alpha\beta}(t) = \frac{1}{\hbar}\int_0^\infty d\omega \frac{J_{\alpha\beta}(\omega)}{\omega^2}\Big[i\sin(\omega t) - (1-\cos(\omega t))\coth(\hbar\beta\omega/2)\Big] \tag{3.41}$$

For weak system-bath interaction $u_{\alpha q} \ll 1$, the 1st-order expansion of the self-energy in terms of the phase φ, gives

$$\Sigma_{\alpha\beta}(t) \approx \tilde{\Delta}^2_{\alpha\beta}\Big(\cos\big[(\epsilon_\alpha - \epsilon_\beta)t/\hbar\big](1 + \varphi_{\alpha\beta}(t)\Big) \tag{3.42}$$

Absorbing the bias term into the phase, such that

$$\Sigma_{\alpha\beta}(t) \approx \tilde{\Delta}^2_{\alpha\beta}\Big(\cos\big[(\epsilon_\alpha - \epsilon_\beta)t/\hbar\big] + \tilde{\varphi}_{\alpha\beta}(t, \epsilon_\alpha - \epsilon_\beta)\Big) \tag{3.43}$$

where

$$\tilde{\varphi}_{\alpha\beta}(t, \epsilon_\alpha - \epsilon_\beta) = \cos\big[(\epsilon_\alpha - \epsilon_\beta)t/\hbar\big]\varphi_{\alpha\beta}(t) \tag{3.44}$$

The Laplace-transformed self-energy is therefore

$$\Sigma_{\alpha\beta}(\lambda) \approx \tilde{\Delta}^2_{\alpha\beta}\left(\frac{2\lambda}{\lambda^2 + [(\epsilon_\alpha - \epsilon_\beta)/\hbar]^2} + \varphi_{\alpha\beta}(\lambda, \epsilon_\alpha - \epsilon_\beta)\right) \tag{3.45}$$

and the biased ground-state propagator becomes

$$\tilde{K}_{00;00}(\lambda) = \frac{1}{\lambda + (\Sigma_{10}(\lambda) + \Sigma_{20}(\lambda))} \tag{3.46}$$

Equation 3.46 has a formidable pole structure in the arbitrary bias regime $\epsilon_1 \neq \epsilon_2$. In the interest of producing tractable analytic results here, I inspect the case of tuned biases $\epsilon_1 = \epsilon_2 = \epsilon$, with the ground state $\epsilon_0 = 0$. In this case the pole structure produces a pole at $\lambda = 0$ and solutions to the cubic polynomial

$$\lambda^3 + \lambda^2\Phi(\lambda) + \lambda E^2 + \epsilon^2\Phi(\lambda) = 0 \tag{3.47}$$

where

$$\begin{aligned} \Phi(\lambda) &= \tilde{\Delta}^2_{10}\varphi_{10}(\lambda, \epsilon) + \tilde{\Delta}^2_{20}\varphi_{20}(\lambda, \epsilon) \\ E &= \sqrt{\epsilon^2 + \tilde{\Omega}^2}, \quad \tilde{\Omega}^2 = \tilde{\Delta}^2_{10} + \tilde{\Delta}^2_{20} \end{aligned} \tag{3.48}$$

N.B. when the bath couplings are zero (or equal), the bath decouples from the central system and the phase factors go to zero. In this limit I recover the Laplace-transformed dynamics for the bare-site system of equation 3.15, as one would expect. In accordance

with the perturbative approach I have taken here, I assume that the phase factors are small fluctuations about the bare poles, and so I Taylor expand these functions to 1st-order and evaluate them at the points

$$\lambda_D = 0, \quad \lambda_\pm = \pm iE/2 \tag{3.49}$$

which are the solutions to the pole structure of equation 3.47 in the absence of damping $\varphi = 0$. Recall that in the bare system, ϵ is the energy required to excite the dark state $|D\rangle$ and $(\epsilon \pm E)/2$ for the states $|\lambda_\pm\rangle$. The term involving the bath correlators $\Phi(\lambda)$ (evaluated at the bare poles) can be evaluated with use of the Fluctuation-Dissipation theorem [122, 31] (see Appendix D).

3.2.1 Linear response and the fluctuation-dissipation theorem

I now make a quick digression here to provide a heuristic derivation of the bath correlators above in the linear response regime and show how this is a form of the well known fluctuation-dissipation theorem.

The fluctuation-dissipation theorem is a central feature of linear response theory and is applied here in the 3-site perturbative model. The theorem relates the relaxation of a weakly perturbed system to the thermal fluctuations in the environment. The main result of the theory relates the power spectrum $S(\omega)$ of the fluctuations, to the Fourier transform of the susceptibility $\chi(\omega)$ (the linear response function). We begin with the bath correlation function

$$\varphi(t) = \cos(\epsilon t/\hbar) \int_0^\infty d\omega \frac{J(\omega)}{\hbar\omega^2} \Big(i \sin\omega t - (1 - \cos\omega t) \coth(\hbar\beta\omega/2) \Big) \tag{3.50}$$

the exponentiation of which produces all orders of possible bath interactions with the central system. In the perturbative limit the exponential is expanded to linear order and the Laplace transform of the function reduces to just the transform of the bath correlation function. The phase therefore describes the corrections to the system introduced by the bath. The time-independent term can be factorised in the exponential as a renormalisation of the tunneling energy. So the remaining fluctuating part is

$$\varphi(t) = \cos(\epsilon t/\hbar) \int_0^\infty d\omega \frac{J(\omega)}{\hbar\omega^2} \Big(i \sin\omega t + \cos\omega t \coth(\hbar\beta\omega/2) \Big) \tag{3.51}$$

In the perturbative limit we expect the solutions to the system to be small deviations from the 'bare-system' eigenvalues and thus I Taylor expand the phase about these points. In this case the complex frequencies of the transform take on the bare-eigenvalues λ_0 and we have

$$\varphi(\lambda_0) = \frac{1}{\hbar} \int_0^\infty dt e^{-\lambda_0 t} \cos(\epsilon t/\hbar) \int_0^\infty d\omega \frac{J(\omega)}{\hbar\omega^2} \Big(i \sin\omega t + \cos\omega t \coth(\hbar\beta\omega/2) \Big) \tag{3.52}$$

For the bare-system, uncoupled from the bath, the complex frequencies contain no real part and are related to the Fourier-transform real frequencies by $\lambda_0 \sim i\omega_0$. Performing the time integration first, and using the definition of the delta-function, we find

$$\begin{aligned} \varphi(\omega_0) = \frac{1}{4\hbar} \int_0^\infty d\omega \frac{J(\omega)}{\omega^2} \Bigg\{ & \Big[\delta(\omega - \omega_0 + \epsilon/\hbar) + \delta(\omega - \omega_0 - \epsilon/\hbar) \\ & - \delta(\omega + \omega_0 - \epsilon/\hbar) - \delta(\omega + \omega_0 + \epsilon/\hbar) \Big] + \Big[\delta(\omega - \omega_0 + \epsilon/\hbar) + \delta(\omega - \omega_0 - \epsilon/\hbar) \\ & + \delta(\omega + \omega_0 - \epsilon/\hbar) + \delta(\omega + \omega_0 + \epsilon/\hbar) \Big] \coth(\hbar\beta\omega/2) \Bigg\} \end{aligned} \tag{3.53}$$

and performing the frequency integrals

$$\begin{aligned} \varphi(\omega_0) = \frac{1}{4\hbar} \Bigg[& \frac{J(\omega_0 - \epsilon/\hbar)}{(\omega_0 - \epsilon/\hbar)^2} + \frac{J(\omega_0 + \epsilon/\hbar)}{(\omega_0 + \epsilon/\hbar)^2} - \frac{J(\epsilon/\hbar - \omega_0)}{(\omega_0 - \epsilon/\hbar)^2} - \frac{J(-\omega_0 - \epsilon/\hbar)}{(\omega_0 + \epsilon/\hbar)^2} \\ & + \frac{J(\omega_0 - \epsilon/\hbar)}{(\omega_0 - \epsilon/\hbar)^2} \coth(\hbar\beta(\omega_0 - \epsilon/\hbar)/2) + \frac{J(\omega_0 + \epsilon/\hbar)}{(\omega_0 + \epsilon/\hbar)^2} \coth(\hbar\beta(\omega_0 + \epsilon/\hbar)/2) \\ & - \frac{J(\epsilon/\hbar - \omega_0)}{(\omega_0 - \epsilon/\hbar)^2} \coth(\hbar\beta(\omega_0 - \epsilon/\hbar)/2) - \frac{J(-\omega_0 - \epsilon/\hbar)}{(\omega_0 + \epsilon/\hbar)^2} \coth(\hbar\beta(\omega_0 + \epsilon/\hbar)/2) \Bigg] \end{aligned} \tag{3.54}$$

A comparison with the formal result of the fluctuation-dissipation theorem provided in Appendix D shows the similarity between the two results. What I have done, is effectively derive the power spectrum of the fluctuations within linear response theory

for the density matrix propagator. The linear response function quoted in the formal theory usually applies to the 2-point propagator (Greens function). We've left the above result general for any form of the spectral density, and we see below how it simplifies for the various specific forms of interest.

3.2.2 Results of the 3-site-boson model in the perturbative regime

The solutions to equation 3.47 are obtained using the method outlined in Appendix E for solving cubic polynomials [123, 124, 125]. When the discriminant D of the cubic polynomial is greater than zero: $D > 0$, we have 1-real and 2-complex roots. I can ascribe the real pole to the Dark-state, as with tuned upper energy levels we have no oscillation frequency between them, so the resultant energy is purely real. The polynomial is solved in the most illuminating form as

$$\begin{aligned}\tilde{\lambda}_D &= \Gamma_\gamma(0) - \Gamma_r(0) \\ \tilde{\lambda}_\pm &= -\frac{\Gamma_\gamma(\pm E)}{2} - \Gamma_r(\pm E) \pm i\omega(\pm E)\end{aligned} \tag{3.55}$$

where

$$\begin{aligned}\Gamma_r(z) = \frac{\Phi(z)}{3}, \quad \Gamma_\gamma(z) = u(z) - v(z), \quad \omega(z) = \frac{\sqrt{3}}{2}(u(z) + v(z)) \\ u = \sqrt[3]{\sqrt{D} - \frac{(2\Phi^3 - 9\Phi E^2 + 27\epsilon^2\Phi)}{54}}, \quad \forall D > 0 \\ v = \sqrt[3]{\sqrt{D} + \frac{(2\Phi^3 - 9\Phi E^2 + 27\epsilon^2\Phi)}{54}}, \quad \forall D > 0\end{aligned} \tag{3.56}$$

So I have one entirely real pole λ_D that contains two decay rates Γ_r and Γ_γ. The remaining complex-conjugate poles contain a combination of the decay rates with a different argument and the frequency of oscillation ω. The discriminant D tells us the nature of the poles

$$D = \left(\frac{2\Phi^3 - 9\Phi E^2 + 27\epsilon^2\Phi}{2916}\right)^2 + \left(\frac{3E^2 - \Phi^2}{81}\right)^3 \tag{3.57}$$

For Ohmic spectral densities the bath correlation function takes the form

$$\Phi_D(0) = \frac{1}{\epsilon}[\tilde{\Delta}_{10}^2\gamma_{10} + \tilde{\Delta}_{20}^2\gamma_{20}]\coth\left(\frac{\epsilon}{\omega_c}\right)\coth\left(\frac{\hbar\beta\epsilon}{2}\right)$$

$$\Phi_{\pm}(\pm E) = [\tilde{\Delta}_{10}^2\gamma_{10} + \tilde{\Delta}_{20}^2\gamma_{20}]\Bigg\{\frac{\coth\left(\frac{E-\epsilon}{\omega_c}\right)}{E-\epsilon}\Big[1+\coth\left(\frac{\hbar\beta(E-\epsilon)}{2}\right)\Big] + \frac{\coth\left(\frac{E+\epsilon}{\omega_c}\right)}{E+\epsilon}\Big[1+\coth\left(\frac{\hbar\beta(E+\epsilon)}{2}\right)\Big]\Bigg\} \tag{3.58}$$

For super-Ohmic spectral densities the bath correlation function takes the form

$$\Phi_D(0) = \epsilon[\tilde{\Delta}_{10}^2\gamma_{10} + \tilde{\Delta}_{20}^2\gamma_{20}]\coth\left(\frac{\epsilon}{\omega_c}\right)\coth\left(\frac{\hbar\beta\epsilon}{2}\right)$$

$$\Phi_{\pm}(\pm E) = [\tilde{\Delta}_{10}^2\gamma_{10} + \tilde{\Delta}_{20}^2\gamma_{20}]\Bigg\{\coth\left(\frac{E-\epsilon}{\omega_c}\right)(E-\epsilon)\Big[1+\coth\left(\frac{\hbar\beta(E-\epsilon)}{2}\right)\Big] + \coth\left(\frac{E+\epsilon}{\omega_c}\right)(E+\epsilon)\Big[1+\coth\left(\frac{\hbar\beta(E+\epsilon)}{2}\right)\Big]\Bigg\} \tag{3.59}$$

3.2.3 Validity of NIBA in the perturbative regime for Ohmic and super-Ohmic damping

In Section 2.5 I introduced NIBA and discussed the mathematical condition for its validity. This amounted to the calculation of the 1st-moment of the self-energy (influence functional) which tells us the ratio of the blip/sojourn times F_1. In order for the coherences in the system to be short-lived, this 1st-moment must be small, such that $F_1 \ll 1$, and NIBA applies. Here we quantify it for the various spectral densities of interest within the perturbative regime. For Ohmic spectral densities the bath correlators take the form

$$\varphi_{\alpha\beta}(\lambda) = \frac{1}{\pi\hbar}(\eta_\alpha - \eta_\beta)^2\lambda\coth\left(\frac{\beta\lambda}{2}\right) \tag{3.60}$$

and for the super-Ohmic case

$$\varphi_{\alpha\beta}(\lambda) = \frac{1}{\pi\hbar}(\rho_\alpha - \rho_\beta)^2\lambda^3\coth\left(\frac{\beta\lambda}{2}\right) \tag{3.61}$$

where λ are the complex-frequencies of the bare-3-site system. The total self-energy is $\Sigma(\lambda) = \Sigma_{10}(\lambda) + \Sigma_{20}(\lambda)$, where

$$\Sigma_{\alpha\beta}(\lambda) \approx \tilde{\Delta}^2_{\alpha\beta}\left(\frac{\lambda}{\lambda^2+(\epsilon_\alpha-\epsilon_\beta)^2}+\varphi_{\alpha\beta}(\lambda-i(\epsilon_\alpha-\epsilon_\beta))+\varphi_{\alpha\beta}(\lambda+i(\epsilon_\alpha-\epsilon_\beta))\right) \quad (3.62)$$

In order to calculate F_1, I compute the derivative of the self-energy, which for both Ohmic and super-Ohmic spectral densities, I find

$$F_1 = \lim_{\lambda\to 0}\frac{\partial}{\partial\lambda}\Sigma(\lambda) = \frac{\Delta^2_{10}}{\epsilon_1^2}+\frac{\Delta^2_{20}}{\epsilon_2^2} \quad (3.63)$$

The condition for F_1 here in the perturbative regime, demonstrates the dependency of NIBA on the ratio Δ/ϵ. We see that as the bias energy goes to zero, the 1st-moment diverges, and thus we invalidate NIBA in this regime. Therefore NIBA only applies to biased systems in the perturbative regime, specifically small values of the tunnelling frequency relative to the bias energy. Qualitatively this is intuitive; as for large tunnelling frequency, we expect the system to spend more time in the off-diagonal states, and correspondingly for small bias energies, the system becomes less localised in each well. The coherences become more pronounced in this limit, and thus interactions between coherences to higher orders must be considered.

3.2.4 Coherent phase space in the perturbative regime

I now investigate the coherent-incoherent phase space of the model here in the perturbative limit. The sign of the discriminant D (see equation 3.57) determines what region of the phase space we're in.

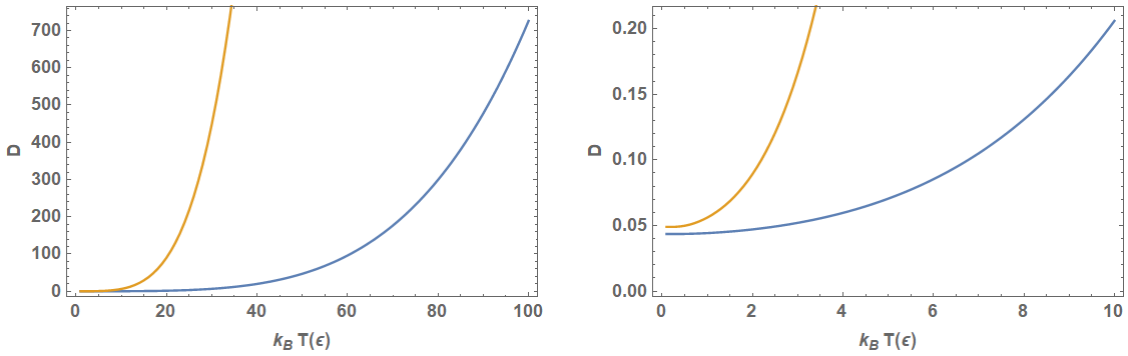

(a) **(b)**

Figure 3.9: Coherent-incoherent phase space of tuned-perturbative 3-site-bath model. Parameters: $\Delta_{10} = 0.1$, $\Delta_{20} = 0.12$ $\gamma_1 = 0.01$, $\gamma_2 = 0.05$, in units of ϵ. (blue) Ohmic, (orange) super-Ohmic.

In Figure 3.9 I investigate only the region where NIBA is valid, i.e. for large bias relative to tunnelling terms. We see that for all temperatures, the discriminant remains positive, and therefore the system is always in the underdamped regime. Therefore there are always two complex conjugate solutions and one real solution to the poles of the propagator.

3.2.5 Decay times in the perturbative regime for Ohmic spectral densities

Here I investigate the relationship of the various decay times in the system versus temperature and system-bath coupling for Ohmic spectral densities. In the high-temperature limit I can expand the temperature dependent function in terms of the dimensionless parameter $z/K_BT \ll 1$

$$\coth\left(\frac{z}{2k_BT}\right) = \frac{2k_BT}{z} + \frac{2z}{3k_BT} + ... \tag{3.64}$$

where $z \in \{\epsilon, \epsilon \pm E\}$. If I take just the 1st order term I can investigate this for various spectral densities. The relaxation time τ_r is the inverse of the pure relaxation rate $\Phi \equiv 1/\tau_r$ and for an Ohmic spectral density, the times are

$$\tau_r^{\pm} = \frac{1}{(\epsilon \pm E)[(\gamma_1 - \gamma_3)^2 + (\gamma_2 - \gamma_3)^2]}, \quad T = 0K, \quad \text{(Ohmic)}$$
$$\tau_r^{D} = \frac{1}{\epsilon[(\gamma_1 - \gamma_3)^2 + (\gamma_2 - \gamma_3)^2]}, \quad T = 0K, \quad \text{(Ohmic)}$$
$$\tau_r^{\pm} = T_r^{D} = \frac{1}{2k_B T[(\gamma_1 - \gamma_3)^2 + (\gamma_2 - \gamma_3)^2]}, \quad k_B T \gg \epsilon \pm E, \epsilon, \quad \text{(Ohmic)} \tag{3.65}$$

The relaxation time τ_γ is far more complicated in analytic form so instead I graph the full decay times associated with the frequencies $\tilde{\lambda}_D, \tilde{\lambda}_\pm$

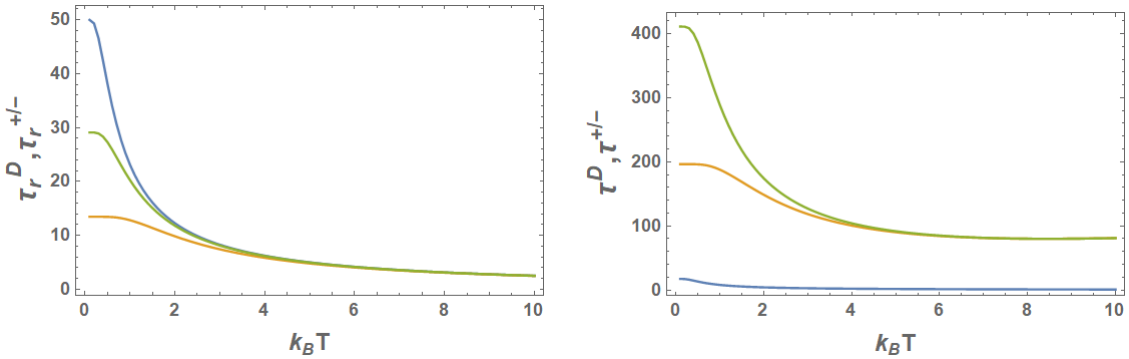

(a) **(b)**

Figure 3.10: (a) Pure relaxation times vs $k_B T$; $\tau_r^{\pm} = 3/\Phi(E)$ (orange/green), $\tau_r^{D} = 3/\Phi(\epsilon)$ (blue), (b) Full relaxation times vs $k_B T$; $\tau^{\pm} = 1/\mathrm{Re}\tilde{\lambda}_\pm$ (orange/green), $\tau^{D} = 1/\mathrm{Re}\tilde{\lambda}_D$ (blue). Parameters: $\gamma_1 = 0.01$, $\gamma_2 = 0.05$, $\epsilon = 1$, $\Delta_{10} = 0.1$, $\Delta_{20} = 0.2$,

We see that the pure relaxation times corresponding to $\lambda_\pm, \lambda_D$ are different for low temperatures. As the temperature is increased however, the two times converge and follow an inverse function of $k_B T$, independent of ϵ, E as indicated in equation 3.65. The system rapidly relaxes to the bath in this limit.

For all $k_B T$ the dark-state dominates the dynamics as its relaxation time is much lower than the other relaxation time in the system. Furthermore, the dark-state relaxation time tends towards zero very rapidly with increasing temperature, whereas $\tau_\pm$ tends towards a constant asymptotic value and the two relaxation times $\tau_\pm$ become unresolved in this limit. This suggests that for high enough temperatures, the dark state is hardly populated and it is $|\pm\rangle$ that dominates the dynamics. Additionally, in this limit we expect only two distinct frequencies to be present as $\Gamma_\pm$ have become unresolved. Of course as we take

this limit further $\epsilon/\Delta \to \infty$, the relaxation times should tend to infinity as we recover the Independent-boson-model discussed above, where we have only pure dephasing and no energy relaxation.

3.2.6 Decay times in the perturbative regime for super-Ohmic spectral densities

Here I investigate the relationship of the various decay times in the system versus temperature and system-bath coupling for super-Ohmic spectral densities. Once again I investigate the zero $T = 0K$ and high-T limits of the pure decay times but in the super-Ohmic regime now. For the decay times I find

$$\begin{aligned}
\tau_r^{\pm} &= \frac{1}{(\epsilon \pm E)^3[(\gamma_1-\gamma_3)^2+(\gamma_2-\gamma_3)^2]}, \quad T = 0K, \quad \text{(super-Ohmic)} \\
\tau_r^{D} &= \frac{1}{\epsilon^3[(\gamma_1-\gamma_3)^2+(\gamma_2-\gamma_3)^2]}, \quad T = 0K, \quad \text{(super-Ohmic)} \\
\tau_r^{\pm} &= \frac{1}{2k_BT(\epsilon \pm E)^2[(\gamma_1-\gamma_3)^2+(\gamma_2-\gamma_3)^2]}, \quad k_BT \gg \epsilon \pm E, \quad \text{(super-Ohmic)} \\
\tau_r^{D} &= \frac{1}{2k_BT\epsilon^2[(\gamma_1-\gamma_3)^2+(\gamma_2-\gamma_3)^2]}, \quad k_BT \gg \epsilon, \quad \text{(super-Ohmic)}
\end{aligned} \tag{3.66}$$

Immediately we notice that the full decay times do not converge and $\tau_r^D, \tau_r^{\pm}$ remain distinct for all temperatures in the super-Ohmic regime. We also see that the decay times fall off as a power-law in the bare-energies $\epsilon, \epsilon \pm E$.

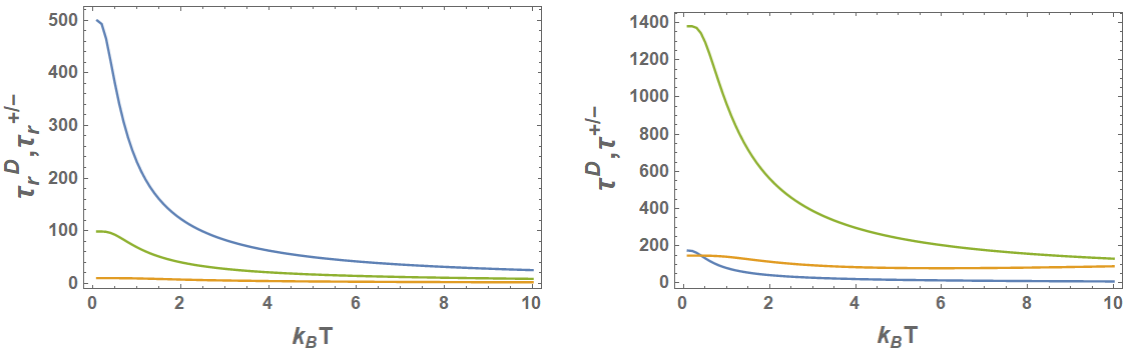

(a) **(b)**

Figure 3.11: (a) Pure relaxation times vs k_BT; $\tau_r^{\pm} = 3/\Phi(E)$ (orange/green), $\tau_r^D = 3/\Phi(\epsilon)$ (blue), (b) Full relaxation times vs k_BT; $\tau^{\pm} = 1/\mathrm{Re}\tilde{\lambda}_{\pm}$ (orange/green), $\tau^D = 1/\mathrm{Re}\tilde{\lambda}_D$ (blue). Parameters: $\gamma_1 = 0.01$, $\gamma_2 = 0.05$, $\epsilon = 1$, $\Delta_{10} = 0.1$, $\Delta_{20} = 0.2$,

Once again, the dark-state decay channel is evidently the most sensitive to the bath for all but the lowest temperatures here in the super-Ohmic regime.

3.3 Perturbative analysis: optical phonon bath with Lorentzian lineshape

I now investigate the 3-site model coupled perturbatively to an optical phonon bath. The spectral density for a realistic optical phonon bath will contain some line-broadening and here I choose a Lorentzian lineshape. Normally Lorentzians are difficult to deal with due to their long tails. However the result of equation 3.54 shows that the phase is dependent only on the spectral density evaluated at the bare poles. Therefore, the divergent frequency integral of the Lorentzian is avoided in this case and I indulge in the use of a Lorentzian spectral density here.

The spectral function for a Lorentzian lineshape centered around a frequency ω_0 and width ξ, including our dimensionless parameter is

$$\frac{1}{\pi\hbar}J_\alpha(\omega) = \Xi_\alpha \frac{\omega_0^2 \xi}{\xi^2 + (\omega - \omega_0)^2} \tag{3.67}$$

where the dimensionless coupling parameter for Lorentzian-optical phonons is defined as

$$\Xi_\alpha = \frac{\nu_\alpha \xi}{\pi\hbar\omega_0^2} \tag{3.68}$$

Applying my perturbative analysis above, the bath correlators for the 3-poles are calculated to be

$$
\begin{aligned}
\Phi_D(0) &= \frac{8\omega_0^3\xi\left(\tilde{\Delta}_{10}^2\Xi_{10}+\tilde{\Delta}_{20}^2\Xi_{20}\right)\coth(\hbar\beta\epsilon/2)}{\epsilon\left(\xi^2+\epsilon^2-2\epsilon\omega_0+\omega_0^2\right)\left(\xi^2+\epsilon^2+2\epsilon\omega_0+\omega_0^2\right)} \\
\Phi_\pm(\pm E) &= \xi\omega_0^2\left(\tilde{\Delta}_{10}^2\Xi_{10}+\tilde{\Delta}_{20}^2\Xi_{20}\right)\Bigg(\frac{\coth(\hbar\beta(\pm E-\epsilon)/2)\left(\frac{1}{(\mp E+\omega_0+\epsilon)^2+\xi^2}-\frac{1}{(\pm E+\omega_0-\epsilon)^2+\xi^2}\right)}{(\pm E-\epsilon)^2} \\
&+\frac{\coth(\hbar\beta(\pm E+\epsilon)/2)\left(\frac{1}{(\pm E-\omega_0+\epsilon)^2+\xi^2}-\frac{1}{(\pm E+\omega_0+\epsilon)^2+\xi^2}\right)}{(\pm E+\epsilon)^2} \\
&+\frac{1}{(\pm E+\epsilon)^2\left((\pm E-\omega_0+\epsilon)^2+\xi^2\right)}-\frac{1}{(\pm E-\epsilon)^2\left((\pm E+\omega_0-\epsilon)^2+\xi^2\right)} \\
&+\frac{1}{(\pm E-\epsilon)^2\left((\mp E+\omega_0+\epsilon)^2+\xi^2\right)}-\frac{1}{(\pm E+\epsilon)^2\left((\pm E+\omega_0+\epsilon)^2+\xi^2\right)}\Bigg)
\end{aligned}
\tag{3.69}
$$

In Figure 3.12 I calculate the three decay times for the optical phonon spectral density in the perturbative limit. I split the two temperature scales $0 < k_BT < 10$ and $10 < k_BT < 100$ to show how the decay times $\tau_\pm$ are indistinguishable for low temperatures, and distinct for high temperatures. We see how for low-T, the dark-state decay channel displays the longest relaxation time, but falls below $\tau_\pm$ for high-T.

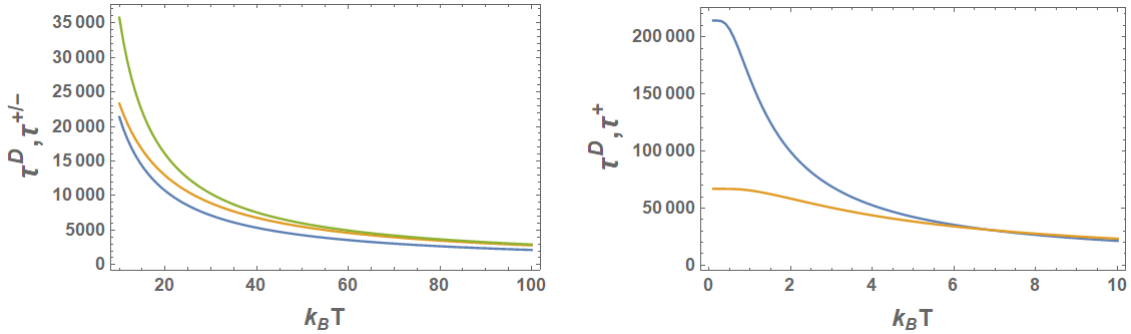

(a) **(b)**

Figure 3.12: Decay times for 3-site model and optical phonons. Parameters: $\Delta_{10} = 0.1$, $\Delta_{20} = 0.2$, $\Xi_1 = 0.01$, $\Xi_2 = 0.01$, $\Gamma = 0.001$, $\omega_0 = 10$.

In Figure 3.13 I plot the phase-space of the 3-site-optical-phonon model showing how the

system remains in the coherent phase for all temperatures in this perturbative limit.

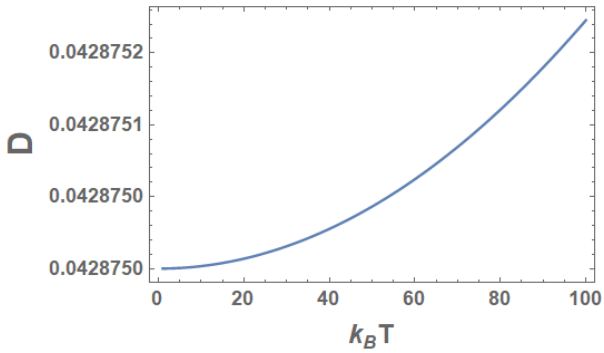

Figure 3.13: Phase space for 3-site model and optical phonons. $\tau_{\pm}$ (orange/green), τ_D (blue). Parameters: $\Delta_{10} = 0.1$, $\Delta_{20} = 0.2$, $\Xi_1 = 0.01$, $\Xi_2 = 0.01$, $\Gamma = 0.001$, $\omega_0 = 10$.

For the optical-phonon spectral density, the dark-state is the most robust state for relatively low-temperatures. We see that as the temperature increases however the 3 decay rates converge.

3.4 The 3-site-independent-boson model and dephasing

I now make a short comment on the limiting case of zero tunnelling $\Delta_{10} = \Delta_{20} = \Delta = 0$. In this limit we only have bias energies ϵ_α as well as the bath H_B including the system-bath coupling. This happens to be an exactly solvable model, given the application of the well known Independent-Boson model [52]. This amounts to applying the polaron transformation to each site independently. What we see in the dynamics amounts to the case of 'pure dephasing', where only the off-diagonal density matrix elements are depleted, while the diagonal elements remain unchanged. The Hamiltonian in this case is

$$H(\Delta = 0) = \epsilon_1 |1\rangle\langle 1| + \epsilon_2 |2\rangle\langle 2| + \epsilon_3 |3\rangle\langle 3| + \sum_q \sum_\alpha^3 |\alpha\rangle\langle\alpha| \lambda_{\alpha,q}(b_q + b_q^\dagger) + \sum_q \omega_q b_q^\dagger b_q \tag{3.70}$$

Since the bath is sensitive to the position of the particle, i.e. which well it occupies, and the tunnelling between wells has been turned off, the particles position does not change and there is no energy dissipated to the bath. We can see that the time-evolution of the diagonal populations is accordingly zero, such that $\partial_t \langle P_{\alpha\alpha} \rangle = 0$ and

$$\frac{\partial}{\partial t} P_{\alpha\alpha} = -i[P_{\alpha\alpha}, H(\Delta = 0)] = 0, \quad \frac{\partial}{\partial t} P_{\alpha\beta} = -i[P_{\alpha\beta}, H(\Delta = 0)] \neq 0 \tag{3.71}$$

whereas the evolution of the off-diagonal populations is non-zero. In the latter case we have what is known as 'pure dephasing'. As this is an exactly solvable model, with just three copies of the well known Independent-boson model, I will only comment on the results here in the text. I have included a calculation of the dynamics for the Ohmic and super-Ohmic spectral density in Appendix G for reference. The dynamics of the system are qualitatively the same for both spectral densities. In the zero-temperature to low-temperature limit, the off-diagonal density matrix elements decay only algebraically in time. For mid-to-high temperatures however, we see an exponential decay.

3.4.1 Summary

In this Chapter I have analysed the 3-site-V system in a number of limiting cases. First of all I considered the case of no environmental coupling such that the 3-site-V system is isolated but for a decaying ground state. This served to demonstrate the phenomenon of population trapping due to the formation of the dark-state. I then included an oscillator bath coupled weakly to the diagonal elements of the 3-site-V Hamiltonian. This corresponds to the diagonal system-bath interaction and was treated using perturbation theory due to the weak nature of the coupling. I investigated this system for three different spectral densities: Ohmic, super-Ohmic and optical. The resulting relaxation times in the system were compared and the dark-state relaxation time, associated with the inverse of the pure decay rate, was shown to be the shortest in the system for all spectral densities. This suggests that for a perturbative system-bath coupling, the dark-state is actually the most sensitive to the effects of the bath and experiences the fastest decay.

Chapter 4

Non-perturbative analysis of the 3-site system coupled diagonally to an Ohmic oscillator bath

I now proceed to treat the oscillator bath coupling to the 3-site-V system non-perturbatively. In Chapter 3, I analysed the 3-site model perturbatively in the system-bath coupling parameter. Here I relax that condition such that the system-bath coupling parameter can be arbitrarily strong. To do this I return to the analysis framework of the 3-site model outlined in Section 3.2, but this time evaluate the influence function non-perturbatively. In this chapter I consider just an Ohmic form for the bath spectral density. However in the next chapter, where I include non-diagonal couplings as well as diagonal system-bath couplings for a 2-state-spin-boson model, I will consider both a super-Ohmic form for the spectral density and a line-broadened optical phonon spectral density.

4.1 NIBA in the 3-site-boson model

We learned from the calculation of the bare transition amplitude for the system, that the path integral formalism for the bare-3-site-system involves a path that returns sequentially to the ground state, and for each subsequent flip, has the option of entering either the left or right branch before once again returning to the ground state. The symmetry about the ground state $|0\rangle$ means that we can be certain that with every flip the system makes from the ground state, it can either go to state $|1\rangle$ or state $|2\rangle$ and return. In the density matrix formalism, my return state is therefore the sojourn χ_{00}. This is possible

to deduce because I operate within NIBA, which favours occupation of diagonal states and only allows an excursion in the off-diagonal portion of the density matrix over one time interval in the path-integral formalism (see section 2.5). Otherwise, the possible blip-sojourn paths would involve a nearest-neighbour hopping around a three-by-three square with all possible combinations of hops. This is a substantially harder combinatorics problem and essentially comes down to the fact that there would exist states $\chi_{10}, \chi_{20}, \chi_{12}$ which would form intermediate symmetric paths in the off-diagonal portion of the density matrix. As I am working in NIBA, which suppresses the time spent by the system in the off-diagonal terms of the density matrix, these states are also suppressed. Mathematically they would manifest in the influence functional as terms that go like $\cos(\chi_{10}\xi_{12})$ and would physically represent subsequent coherent-superposition-states.

With this in mind the influence functional describing this system is

$$\begin{aligned} F^{\xi_{10};\xi_{20}}_{\chi_{11};\chi_{22}}(t) &= f^{\xi^{10}}_{\chi^{11}}(t) + f^{\xi^{20}}_{\chi^{22}}(t) + f^{\xi^{10}}_{\chi^{00}}(t) + f^{\xi^{20}}_{\chi^{00}}(t), \\ &= 4\Delta_{10}^2\Big[\cos\left(\chi^{11}\xi^{10}Q'_j\right) + 1\Big]e^{-\left(\xi^{10}\right)^2 Q''_j} + 4\Delta_{20}^2\Big[\cos\left(\chi^{22}\xi^{20}Q'_j\right) + 1\Big]e^{-\left(\xi^{20}\right)^2 Q''_j} \\ &= 8\Delta_{10}^2\cos^2\left(\chi^{11}\xi^{10}Q'_j/2\right)e^{-\left(\xi^{10}\right)^2 Q''_j} + 8\Delta_{20}^2\cos^2\left(\chi^{22}\xi^{20}Q'_j/2\right)e^{-\left(\xi^{20}\right)^2 Q''_j} \quad (4.1) \end{aligned}$$

where

$$\begin{aligned} Q'(t) &= \int_0^\infty d\omega \frac{j(\omega)}{\omega^2}\sin\omega t \\ Q''(t) &= \int_0^\infty d\omega \frac{j(\omega)}{\omega^2}(1-\cos\omega t)\coth(\beta\hbar\omega/2) \quad (4.2) \end{aligned}$$

The factor 8 in equation 4.1 comes from the summation of various blips and sojourn combinations: $\chi_{x,x'}$ and $\chi_{x',x}$, as well as $\xi_{x,x'}$ and $\xi_{x',x}$. Remember that we're effectively summing the probabilities for the system to be in all possible states. The function $j(\omega)$ in this case includes only the density of states of the bath and the system-bath coupling parameter has been absorbed in to the blip and sojourn terms in equation 4.1.

The influence functional describes the correlations between the outbound and return path, in this case, to return to state $|0\rangle$ where the weight to remain in this state is unity. The two terms represent both paths x, x' propagating through either branch, via the blips

ξ_{10} and ξ_{20} respectively[1]. I've simplified the influence functional in this case by setting $\gamma_0 = 0$, and thus the sojourn $\chi_{00} = 0$. One can think of this as setting the zero spatial position at the ground state.

At this point it is worth checking that the influence functional reduces to the Caldeira-Leggett SB influence functional in the limit that $\Delta_{10} = \Delta, \Delta_{20} = 0$ and $\gamma_2 = \gamma_0$. In this limit the influence functional becomes

$$f_{SB}(t_{2j} - t_{2j-1}) = \Delta^2 \cos\left(\gamma^2 Q'_j\right) e^{-\gamma^2 Q''_j} \tag{4.3}$$

which is indeed the SB model influence functional. Here I have made the same substitutions $\gamma_1 = \gamma/2, \gamma_0 = \gamma_2 = -\gamma/2$ in order to recover the Caldeira-Leggett influence functional (see equation 4.33 in [31].

4.1.1 Ground-state propagator for the unbiased 3-site-boson system

The simplest propagator to calculate is $K_{00;00}(t)$ which describes the return probability to the ground state. In the interest of calculating relaxation times in the system, all the relevant information can be extracted from this propagator as the denominator contains the pole structure of the system. In the path-integral-Influence-Functional formalism it reads in the time domain

$$\begin{aligned} K_{00;00}(t) = 1 + \sum_{n=1}^{\infty} (-i)^{2n} \int_0^t dt_{2n} \int_0^{t_{2n}} dt_{2n-1} F^{\xi_{10};\xi_{20}}_{\chi_{11};\chi_{22}}(t_{2n} - t_{2n-1}) \\ \times \ldots \int_0^{t_3} dt_2 \int_0^{t_2} dt_1 F^{\xi_{10};\xi_{20}}_{\chi_{11};\chi_{22}}(t_2 - t_1) \end{aligned} \tag{4.4}$$

where we've collected the state couplings Δ_{10}, Δ_{20}into the relevant influence functionals. The Laplace transform is

[1]I've used the shorthand notation $Q'_j = Q'_{2j,2j-1}, Q''_j = Q''_{2j,2j-1}$

$$K_{00;00}(\lambda) = \frac{1}{\lambda} + \sum_{n=1}^{\infty} (-i)^{2n} \frac{1}{\lambda^{n+1}} \left(F^{\xi_{10};\xi_{20}}_{\chi_{11};\chi_{22}}(\lambda) \right)^n$$
$$= \frac{1}{\lambda + F^{\xi_{10};\xi_{20}}_{\chi_{11};\chi_{22}}(\lambda)} \tag{4.5}$$

where $F^{\xi_{10};\xi_{20}}_{\chi_{11};\chi_{22}}(\lambda)$ is the full influence functional that allows flips in both branches.

4.1.2 Excited-state propagator for the unbiased 3-site-boson system

While this thesis will focus on calculating the ground-state propagator, I include the excited-state propagator here in the interest of potential further work that requires such propagators. One must take care in the construction of the excited-state propagator as one must take in to the account the final return 'flip' to the excited state, as we did in section 3.2, for the bare-3-site Greens function. Here we look at the return probability to site $|1\rangle$, defined by the propagator $K_{11;11}(t)$. A further complication arises in the 3-site-boson propagator calculation as the influence functional for the system contains time-non-local interacting blips. This forces us to separate terms in the propagator

$$K_{11;11}(\lambda) = \frac{\lambda + f^{\xi_{20}}_{\chi_{22}}(\lambda)}{\lambda^2 + \lambda F^{\xi_{10};\xi_{20}}_{\chi_{11};\chi_{22}}(\lambda)}$$
$$K_{22;22}(\lambda) = \frac{\lambda + f^{\xi_{10}}_{\chi_{11}}(\lambda)}{\lambda^2 + \lambda F^{\xi_{10};\xi_{20}}_{\chi_{11};\chi_{22}}(\lambda)} \tag{4.6}$$

The inverse Laplace transform of equations 4.6 provides the dynamics of the excited states in the system.

4.1.3 The influence functional for a biased 3-site system

I previously demonstrated the path integral decomposition for the calculation of the bare-3-site system in Section 3.1.2. For the full system, including the bath, I calculate the density matrix; which compares two paths coupled via the influence functional. When the paths x, x' visit the same state, we see that the bias contribution from the bare transition amplitudes $A[x]A^*[x]$ produces a factor 1. Whereas when $x(x')$ are, for e.g.

in states $|1\rangle$ ($|2\rangle$), we pick up factors in the transition amplitudes (ignoring factors dt^2 from the Suzuki-Trotter decomposition) of $\exp(-i\epsilon_1 t)[\exp(i\epsilon_2 t)]$. I therefore define the bias factors $B_{\{\xi\}}$ acting on a blip between times $t_{2j} - t_{2j-1}$ to be

$$\begin{aligned} B_{\xi_{10}}(t_{2j} - t_{2j-1}) &= \exp\Big[- i\epsilon_1 \xi_{10}(t_{2j} - t_{2j-1})\Big], \\ B_{\xi_{20}}(t_{2j} - t_{2j-1}) &= \exp\Big[- i\epsilon_2 \xi_{20}(t_{2j} - t_{2j-1})\Big] \end{aligned} \tag{4.7}$$

The $K_{00;00}$ propagator starts and ends in the sojourn χ_{00}, where I set the zero point energy $\epsilon_0 = 0$. Therefore, for the 3-site system in question, the system is constrained to evolve from that point to either χ_{11} or χ_{22} via ξ_{10} or ξ_{20}. For the final time-interval $t - t_{2n}$, the system is constrained to be in state $|0\rangle$, so both propagators in the density matrix combine to give just 1. I've collected the bias factors in to the influence functional terms according to

$$\begin{aligned} \tilde{F}^{\xi_{10};\xi_{20}}_{\chi_{11};\chi_{22}}(\tau_j) = 8\Delta_{10}^2 \cos\big(i\epsilon_1\tau_j\big)\cos^2\big(\chi_{11}\xi_{10}Q'_j/2\big)e^{-\xi_{10}^2 Q''_j} \\ +8\Delta_{20}^2 \cos\big(i\epsilon_2\tau_j\big)\cos^2\big(\chi_{22}\xi_{20}Q'_j/2\big)e^{-\xi_{20}^2 Q''_j} \end{aligned} \tag{4.8}$$

where the time interval is defined as $\tau_j = t_{2j} - t_{2j-1}$. In order to proceed with the analysis I must define the form of the spectral densities which then allows me to evaluate the correlation functions.

4.2 Non-perturbative analysis for Ohmic spectral densities

For Ohmic dissipation we have the following form for the spectral density (discussed in Section 2.3.1)

$$J_\alpha(\omega) = \eta_\alpha \omega e^{-\omega/\omega_c} \tag{4.9}$$

The dimensionless coupling parameter was defined as

$$\gamma_\alpha = \frac{\eta_\alpha}{\pi\hbar} \tag{4.10}$$

however in our formulation of the influence functional above, we have for simplicity, set the zero-position to $x_0 = 0$.

The bath correlators here contain just the bath density of states portion $j(\omega)$ of the spectral density. Performing the integrals in $Q'(t)$ and $Q''(t)$ one gets [31]

$$Q'(t) = \arctan(\omega_c t) \tag{4.11}$$

$$Q''(t) = \frac{1}{2}\ln(1+\omega_c^2 t^2) + \ln\left[\frac{\hbar\beta}{\pi t}\sinh\left(\frac{\pi t}{\hbar\beta}\right)\right] \tag{4.12}$$

The Laplace-transformed influence functional reads

$$f_\alpha(\lambda) = 8\int_0^\infty dt\, e^{-\lambda t}\cos^2\left[\gamma_\alpha \tan^{-1}(\omega_c t)\right]\left(1+\omega_c^2 t^2\right)^{-\gamma_\alpha}\left[\frac{\hbar\beta}{\pi t}\sinh(\frac{\pi t}{\hbar\beta})\right]^{-2\gamma_\alpha} \tag{4.13}$$

As we're considering times much greater than ω_c^{-1}, i.e. times greater than the characteristic timescale of the bath, the quantity $\omega_c t$ is much greater than one. Therefore applying the approximation $\omega_c t >> 1$ to zeroth order provides the approximations

$$1+\omega_c^2 t^2 \approx \omega_c^2 t^2, \quad \cos^2\left[a\arctan(\omega_c t)\right] \approx \cos^2(a\pi) \tag{4.14}$$

such that

$$f_\alpha(\lambda) \approx 8\left(\frac{\hbar\beta}{\pi}\omega_c\right)^{-2\gamma_\alpha}\cos^2\left(\pi\gamma_\alpha\right)\int_0^\infty dt\, e^{-\lambda t}\sinh\left(\frac{\pi t}{\hbar\beta}\right)^{-2\gamma_\alpha} \tag{4.15}$$

At this point one perform the Laplace transform here using the known integral [126]

$$\int_0^\infty dx e^{-at}\sinh^b cx = \frac{1}{2^{b+1}c}\mathrm{B}\left(\frac{a}{2c}-\frac{b}{2}, b+1\right) \tag{4.16}$$

where $B(x,y)$ is the Beta function, producing

$$f_\alpha(\lambda) = 8\left(\frac{\hbar\beta}{2\pi}\right)^{1-2\gamma_\alpha}\omega_c^{-2\gamma_\alpha}\cos^2\left(\pi\gamma_\alpha\right)\mathrm{B}\left(\frac{\hbar\beta\lambda}{2\pi}+\gamma_\alpha, 1-2\gamma_\alpha\right) \tag{4.17}$$

Turning the Beta function in to Gamma functions using

$$\mathrm{B}(x,y) = \frac{\Gamma(x)\Gamma(y)}{\Gamma(x+y)} \tag{4.18}$$

finally yields

$$f_\alpha(\lambda) = 8\omega_c^{-2\gamma_\alpha}\cos^2\left(\pi\gamma_\alpha\right)\Gamma[1-2\gamma_\alpha]\left(\frac{\hbar\beta}{2\pi}\right)^{1-2\gamma_\alpha}\frac{\Gamma(\gamma_\alpha+\hbar\beta\lambda/2\pi)}{\Gamma(1-\gamma_\alpha+\hbar\beta\lambda/2\pi)} \tag{4.19}$$

I can collect constant terms in 4.19 that contribute only to the renormalisation of the tunneling matrix elements in to

$$C_{\xi_{10}}^{\chi_{11}} = 8\omega_c^{-2\gamma_1}\cos^2(\pi\gamma_1)\Gamma(1-2\gamma_1), \quad C_{\xi_{20}}^{\chi_{22}} = 8\omega_c^{-2\gamma_2}\cos^2(\pi\gamma_2)\Gamma(1-2\gamma_2) \tag{4.20}$$

These renormalisation constants renormalise the tunneling matrix elements according

$$\tilde{\Delta}_1 = \sqrt{8\omega_c^{-2\gamma_1}\cos^2(\pi\gamma_1)\Gamma(1-2\gamma_1)}\Delta_1, \quad \tilde{\Delta}_2 = \sqrt{8\omega_c^{-2\gamma_2}\cos^2(\pi\gamma_2)\Gamma(1-2\gamma_2)}\Delta_2 \tag{4.21}$$

Extrapolating to the full biased influence functional $\tilde{F}$ with all terms included we find

$$\tilde{F}_{\chi_{11};\chi_{22}}^{\xi_{10};\xi_{20}}(\lambda) = \tilde{\Delta}_1^2\mu^{1-2\gamma_1}\frac{\Gamma(\gamma_1+\hbar\beta(\lambda+i\epsilon)/2\pi)}{\Gamma(1-\gamma_1+\hbar\beta(\lambda+i\epsilon)/2\pi)} + \tilde{\Delta}_2^2\mu^{1-2\gamma_2}\frac{\Gamma(\gamma_2+\hbar\beta(\lambda+i\epsilon_2)/2\pi)}{\Gamma(1-\gamma_2+\hbar\beta(\lambda+i\epsilon_2)/2\pi)} \tag{4.22}$$

where I've defined

$$\mu = \frac{\hbar\beta}{2\pi} \tag{4.23}$$

The next steps in the analysis of the 3-site system coupled to an Ohmic bath requires approximations of the Gamma functions, which at this point create polynomials in the pole structure of the propagators up to infinite order as they stand. As the expansion in the coupling constant has already been treated in the perturbative analysis, we'll of course focus here on the different temperature regimes so as to expand the Gamma functions. However as it turns out, the fully analytic form in the low-T (and zero-T by extension) regime is unfortunately unavailable to us in the case of the 3-site model. This is because the pole structure of the propagator takes on an arbitrary order due to the presence of terms that go like λ^γ. The work on the original 2-site-spin-boson model was able to get around this and reduce the pole structure to a tractable form because there

was only one exponent γ which could be factored out. However in our case, there are two, coming from the two paths in the system and the pole structure remains intractable analytically. Of course one can easily solve these polynomials numerically, however that is beyond the scope of this thesis which is primarily interested in analytic solutions.

4.2.1 Validity of NIBA for the 3-site-Ohmic-boson model

I first inspect the regions of validity of NIBA so as to guide my exploration of the parameter space of results. In order to determine the validity of NIBA in this regime I once again calculate the ratio F_1

$$F_1 = \frac{\langle b \rangle}{\langle s \rangle} = \lim_{\lambda \to 0} \frac{\partial}{\partial \lambda} F^{\xi_{10};\xi_{20}}_{\chi_{11};\chi_{22}}(\lambda) \tag{4.24}$$

to be

$$\begin{aligned}
F_1 = &-\frac{2\mu^{2-\gamma_1}\tilde{\Delta}_{10}^2}{\Gamma(1-\gamma_1/2-i\mu\epsilon_1)(\gamma_1-2i\mu\epsilon_1)^2}\Bigg(\Gamma(\gamma_1/2-i\mu\epsilon_1)\Big(2+\psi_0(1-\gamma_1/2-i\mu\epsilon_1)-\psi_0(\gamma_1/2-i\mu\epsilon_1)\Big)\gamma_1 \\
&-2i\mu\epsilon_1\Big(2+\psi_0(1-\gamma_1/2-i\mu\epsilon_1)-\psi_0(\gamma_1/2-i\mu\epsilon_1)\Big)\Bigg) \\
&-\frac{2\mu^{2-\gamma_1}\tilde{\Delta}_{10}^2}{\Gamma(1-\gamma_1/2+i\mu\epsilon_1)(\gamma_1+2i\mu\epsilon_1)^2}\Bigg(\Gamma(\gamma_1/2+i\mu\epsilon_1)\Big(2+\psi_0(1-\gamma_1/2+i\mu\epsilon_1)-\psi_0(\gamma_1/2+i\mu\epsilon_1)\Big)\gamma_1 \\
&+2i\mu\epsilon_1\Big(2+\psi_0(1-\gamma_1/2+i\mu\epsilon_1)-\psi_0(\gamma_1/2+i\mu\epsilon_1)\Big)\Bigg) \\
&-\frac{2\mu^{2-\gamma_2}\tilde{\Delta}_{20}^2}{\Gamma(1-\gamma_2/2-i\mu\epsilon_2)(\gamma_2-2i\mu\epsilon_2)^2}\Bigg(\Gamma(\gamma_2/2-i\mu\epsilon_2)\Big(2+\psi_0(1-\gamma_2/2-i\mu\epsilon_2)-\psi_0(\gamma_2/2-i\mu\epsilon_2)\Big)\gamma_2 \\
&-2i\mu\epsilon_2\Big(2+\psi_0(1-\gamma_2/2-i\mu\epsilon_2)-\psi_0(\gamma_2/2-i\mu\epsilon_2)\Big)\Bigg) \\
&-\frac{2\mu^{2-\gamma_2}\tilde{\Delta}_{20}^2}{\Gamma(1-\gamma_2/2+i\mu\epsilon_2)(\gamma_2+2i\mu\epsilon_2)^2}\Bigg(\Gamma(\gamma_2/2+i\mu\epsilon_2)\Big(2+\psi_0(1-\gamma_2/2+i\mu\epsilon_2)-\psi_0(\gamma_2/2+i\mu\epsilon_2)\Big)\gamma_2 \\
&+2i\mu\epsilon_2\Big(2+\psi_0(1-\gamma_2/2+i\mu\epsilon_2)-\psi_0(\gamma_2/2+i\mu\epsilon_2)\Big)\Bigg)
\end{aligned} \tag{4.25}$$

We see from inspection of equation 4.25 how temperature, tunnelling and coupling strength affect the NIBA condition $F_1 \ll 1$. The parameter $\mu = \hbar/2\pi k_B T$ contains

the temperature dependence. The function for F_1 contains a fairly complicated dependence on the free parameters $T, \epsilon, \gamma, \Delta$, due to the presence of the polygamma functions. F_1 does however display a simple quadratic dependence in the the renormalised tunneling terms $\tilde{\Delta}$ where we see that by increasing the tunnelling strength brings us out of the regime of validity of NIBA. Intuitively this makes sense, as more dominant tunnelling leads to an increase coherence effects and thus counteracts the effect of the environment to affect decoherence in the system. It's for this reason that NIBA is indeed valid for small values of Δ/ω_c. We see more clearly here how NIBA remains a valid approximation for $k_BT \gg \Delta$ as in this limit I minimise F_1. Upon inspection of the function governing the renormalisation of the tunneling matrix element (see equation 4.21), we see how NIBA becomes exact for $\gamma = 1/4$, verifying a result previously identified by Leggett et al. [31] to be the so called Toulouse limit. This happens because the $\cos(2\pi\gamma)$ term coming from the blip-sojourn interaction part of the influence functional vanishes in this limit.

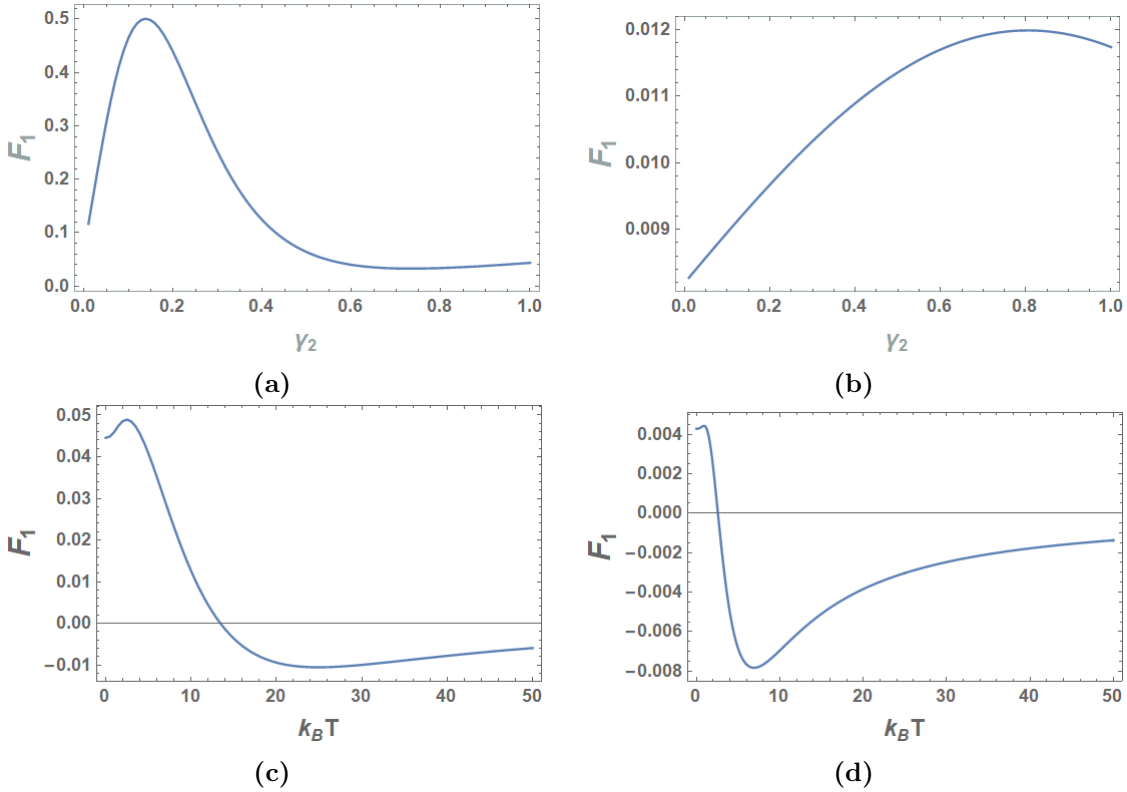

Figure 4.1: F_1 vs γ_1 figures (a) and (b), F_1 vs k_BT figures (c) and (d). Parameters: $\gamma_0 = 0$, $\gamma_2 = 0.2$, $\epsilon_1 = 1$, $\epsilon_2 = 1.5$. (a) $\Delta_{10} = 0.1, \Delta_{20} = 0.2$, $k_BT = 10$ (b) $\Delta_{10} = 0.1, \Delta_{20} = 0.2$, $k_BT = 0.1$, (c) $\Delta_{10} = 0.1, \Delta_{20} = 0.2$, $\gamma_1 = 0.2$, (d) $\Delta_{10} = 0.1, \Delta_{20} = 0.2$, $\gamma_1 = 0.8$

We see from Figure 4.1 how F_1 is minimised for a range of γ_1, predominantly in the mid-strong coupling regime. For small values of γ_1, as one would expect, F_1 is large, and therefore outside the region of validity of NIBA. Here the system exhibits strongly coherent oscillations, and one must go beyond NIBA in order to account for this. As γ_1 approaches 1 we also see a rapid divergence in F_1 coming from the $\Gamma[1-\gamma]$ factor in the tunnelling renormalisation term.

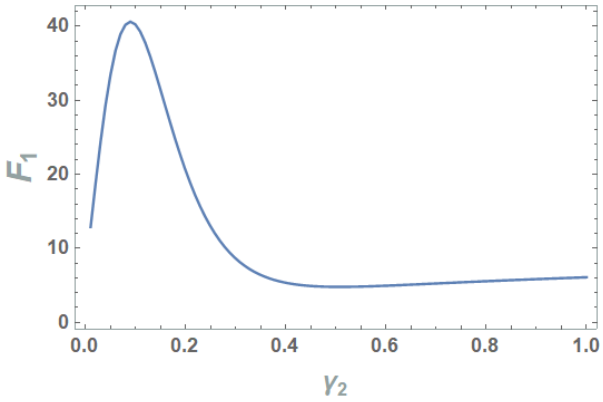

Figure 4.2: F_1 vs γ_2. Parameters: $\gamma_0 = 0$, $\gamma_1 = 0.2$, $\epsilon_1 = \epsilon_2 = 1$, $\Delta_1 = \Delta_2 = \Delta = 1$ (a) $\gamma_2 = 0.2$, (b) $k_B T = 10$

In Figure 4.2 I inspect the regime where the tunnelling elements are comparable to the bias energies. We see that NIBA is essentially invalid here, as F_1 remains much larger than 1 throughout the range of γ even for high-temperature.

4.2.2 Mid-high temperatures in the non-perturbative regime

In the high temperature regime, $k_B T \gg \hbar\Delta$, I can expand the Gamma functions in the influence functional in terms of the parameter $\mu\lambda$, where $\mu = 2\pi/k_B T$. First I express the influence functional in the form

$$f_\chi^\xi(\lambda) = \left(\frac{\mu^{1-2\gamma}}{\gamma + \mu\lambda}\right) \frac{\Gamma(1+\gamma+\mu\lambda)}{\Gamma(1-\gamma+\mu\lambda)} \tag{4.26}$$

having used the functional relation of the gamma function $\Gamma(1+z) = z\Gamma(z)$ N.B. this relationship for the Gamma function takes it from its holomorphic form to its meromorphic form which therefore allows us to access the pole structure of the propagator [127]. Taylor expanding about $\mu\lambda = 0$ up to 2nd order

$$f_{\chi}^{\xi}(\lambda) \approx \left(\frac{\mu^{1-2\gamma}}{\gamma+\mu\lambda}\right)\frac{\Gamma(1+\gamma)}{\Gamma(1-\gamma)}\Bigg[1+\mu\lambda\Big(\psi_0(1+\gamma)-\psi_0(1-\gamma)\Big) + \frac{(\mu\lambda)^2}{2}\Big(\psi_0^2(1-\gamma)+\psi_0^2(1+\gamma)-2\psi_0(1-\gamma)\psi_0(1+\gamma) - \psi_1(1-\gamma)+\psi_1(1+\gamma)\Big)\Bigg] \tag{4.27}$$

where $\psi_0(z)$ is the digamma function defined as

$$\psi_0(z) = \frac{\Gamma'(z)}{\Gamma(z)}, \quad \psi_m = \frac{d^m}{dz^m}\psi_0(z) \tag{4.28}$$

Explicitly the full influence functional in this regime is found to be

$$F_{\chi_{11};\chi_{22}}^{\xi_{10};\xi_{20}}(\lambda) = \tilde{\Delta}_1^2\left(\frac{\mu^{1-2\gamma_1}}{\gamma_1+\mu\lambda}\right)\nu_1\left(1+\mu\Lambda_1\lambda+\frac{\mu^2\Theta_1}{2}\lambda^2\right) + \tilde{\Delta}_2^2\left(\frac{\mu^{1-2\gamma_2}}{\gamma_2+\mu\lambda}\right)\nu_2\left(1+\mu\Lambda_2\lambda+\frac{\mu^2\Theta_2}{2}\lambda^2\right) \tag{4.29}$$

with the biases introduced via

$$\tilde{F}_{\chi_{11};\chi_{22}}^{\xi_{10};\xi_{20}}(\lambda) = \tilde{f}_{\chi_{11}}^{\xi_{10}}(\lambda+i\epsilon)+\tilde{f}_{\chi_{11}}^{\xi_{10}}(\lambda-i\epsilon)+\tilde{f}_{\chi_{22}}^{\xi_{20}}(\lambda+i\epsilon)+\tilde{f}_{\chi_{22}}^{\xi_{20}}(\lambda-i\epsilon) \tag{4.30}$$

where

$$\begin{aligned}
&\nu_1 = \frac{\Gamma(1+\gamma_1)}{\Gamma(1-\gamma_1)}, \quad \nu_2 = \frac{\Gamma(1+\gamma_2)}{\Gamma(1-\gamma_2)},\\
&\Lambda_1 = \psi_0(\gamma_1)-\psi_0(1-\gamma_1), \quad \Lambda_2 = \psi_0(\gamma_2)-\psi_0(1-\gamma_2),\\
&\Theta_1 = \psi_0^2(1-\gamma_1)+\psi_0^2(1+\gamma_1)-2\psi_0(1-\gamma_1)\psi_0(1+\gamma_1)-\psi_1(1-\gamma_1)+\psi_1(1+\gamma_1),\\
&\Theta_2 = \psi_0^2(1-\gamma_2)+\psi_0^2(1+\gamma_2)-2\psi_0(1-\gamma_2)\psi_0(1+\gamma_2)-\psi_1(1-\gamma_2)+\psi_1(1+\gamma_2)
\end{aligned} \tag{4.31}$$

The pole structure of the propagator takes a cubic form if I restrict myself to the limit $\epsilon_1 = \epsilon_2 = \epsilon$ and $\gamma_1 = -\gamma_2$. So I have for the pole structure of the propagator

$$\lambda + \Omega^2 \left(\frac{\mu^{1-2\gamma}}{\gamma + \mu(\lambda - i\epsilon)} \right) \nu_1 \left(1 + \mu\Lambda(\lambda - i\epsilon) + \frac{\mu^2\Theta}{2}(\lambda - i\epsilon)^2 \right)$$
$$+\Omega^2 \left(\frac{\mu^{1-2\gamma}}{\gamma + \mu(\lambda + i\epsilon)} \right) \nu \left(1 + \mu\Lambda(\lambda + i\epsilon) + \frac{\mu^2\Theta}{2}(\lambda + i\epsilon)^2 \right) = 0 \tag{4.32}$$

where the coefficients of the cubic equation

$$a\lambda^3 + b\lambda^2 + c\lambda + d = 0 \tag{4.33}$$

are

$$a = \frac{\gamma\theta\nu\Omega^2\mu^{3-2\gamma} + 2\Lambda\nu\Omega^2\mu^{3-2\gamma} + 2\gamma\mu}{\theta\nu\Omega^2\mu^{4-2\gamma} + \mu^2} \tag{4.34}$$

$$b = \frac{\gamma^2 + 2\gamma\Lambda\nu\Omega^2\mu^{2-2\gamma} + 2\nu\Omega^2\mu^{2-2\gamma} + \theta\nu\Omega^2\epsilon^2\mu^{4-2\gamma} + \mu^2\epsilon^2}{\theta\nu\Omega^2\mu^{4-2\gamma} + \mu^2}$$

$$d = \frac{2\gamma\nu\Omega^2\mu^{1-2\gamma} - \gamma\theta\nu\Omega^2\epsilon^2\mu^{3-2\gamma} + 2\Lambda\nu\Omega^2\epsilon^2\mu^{3-2\gamma}}{\theta\nu\Omega^2\mu^{4-2\gamma} + \mu^2} \tag{4.35}$$

One can also verify, upon turning off the bath couplings $\gamma_1 = \gamma_2 = 0$, that we recover the bare-3-site frequencies of the density matrix propagator, which is an important consistency check.

4.2.3 Coherent phase space and relaxation times: Ohmic regime for mid-high-temperatures

Next I inspect the relaxation times in the system for an Ohmic spectral density in the high-T regime. For the case of small tunnelling relative to bias energies, the system is in the coherent phase. This is characterised by a positive discriminant for all system-bath coupling values up to a critical value, and so I solve the cubic equation using the solutions outlined in Appendix E.

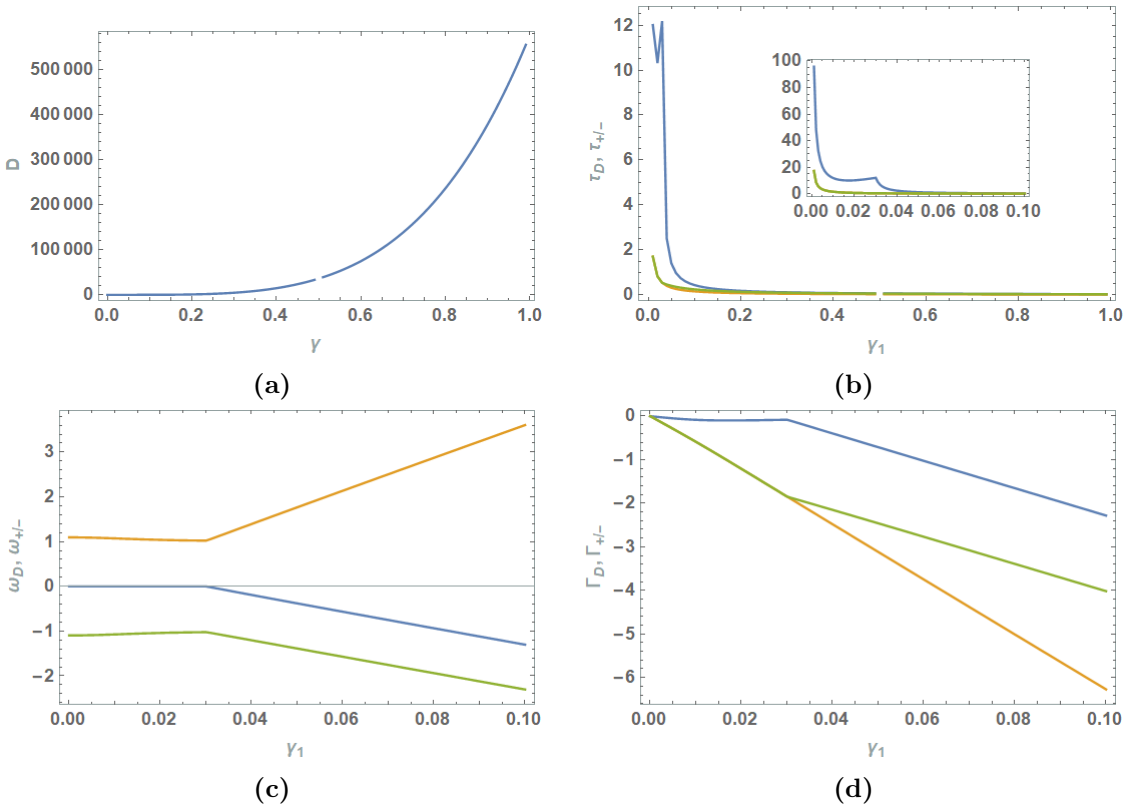

Figure 4.3: Phase space, decay rates, relaxation times and oscillation frequency vs γ (coherent regime). Γ_D, τ_D (blue), Γ_-, τ_+ (green), Γ_+, τ_- (orange). Parameters: $\Delta_1 = 0.1$, $\Delta_2 = 0.05$, $\epsilon = 1$, $k_B T = 10$

In Figure 4.3 we see the results for the symmetric, high temperature, 3-site-boson model with Ohmic spectral density. I find for the parameter range considered here that the system remains in a persistent coherent phase across the range of the system-bath dimensionless coupling parameter. As such I calculate the three oscillation frequencies in the system and find them to be relatively constant for small system-bath couplings. For large enough couplings they diverge however with the dark state having the smallest oscillation frequency. We also find that the dark state relaxation time dominates substantially over small coupling strengths and for intermediate to high coupling strengths it remains dominant but to a lesser degree.

4.2.4 3-site-Ohmic bath model in FMO

I now look at the results of the 3-site-boson model within the context of photosynthesis, for an Ohmic spectral density. In Section 4.2 I was able to solve the system

non-perturbatively in the Ohmic regime of the bath in the limit of $\gamma_1 = \gamma_2 = \gamma$ and $\epsilon_1 = \epsilon_2 = \epsilon$. Therefore I apply these results here to the case of the FMO complex in photosynthesis. The parameters used for the FMO system were outlined in Chapters 1 and 2. It was determined that for an effective 3-site-model in the FMO complex the two tunnelling energies are $\Delta_{10} = 2\text{meV}$ and $\Delta_{20} = 3\text{meV}$, the bias energy is $\epsilon = 20\text{meV}$. Feeding these parameters in to the non-perturbative analysis of Section 4.2 and leaving the system-bath coupling as a free parameter for now, I present the coherent phase and relaxation times in Figure 4.4.

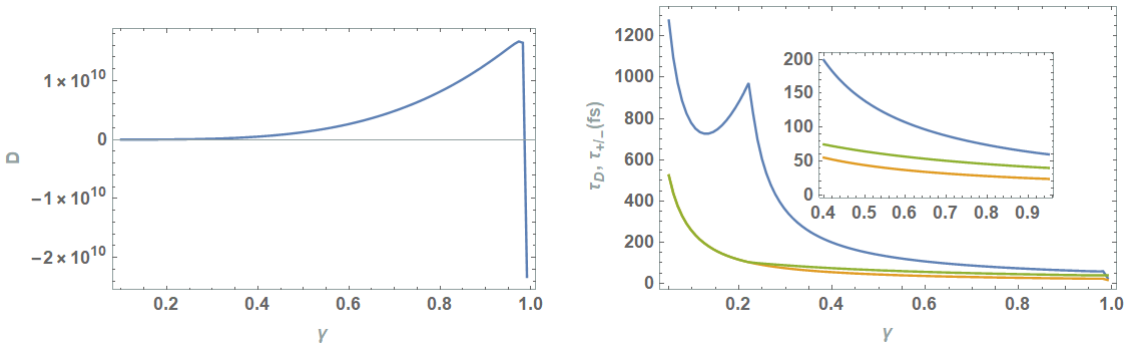

(a) **(b)**

Figure 4.4: Phase space and relaxation times of FMO complex at T=300K in units of femtoseconds with Ohmic bath. FMO parameters: $\tilde{\Delta}_{10} = 2meV$, $\tilde{\Delta}_{20} = 3meV$, $\epsilon = 20meV$

We see from figure 4.4 how the 3-level system coupled to an Ohmic bath remains in the coherent phase even at physiological temperatures for system-bath couplings below the critical value $\gamma = 1$. Incidentally, this is the same critical value for the diagonal coupling where the coherent-incoherent phase transition was also observed in the original spin-boson model. For the FMO parameter $\gamma = 0.22$, we are therefore in the coherent phase. We see that the dark-state relaxation time dominates and in this case I find relaxation times $\tau_D \sim 800\text{fs}$, $\tau_\pm \sim 100\text{fs}$.

4.2.5 Summary

In this Chapter I have treated the coupling of a 3-state-V system to an external oscillator bath non-perturbatively. The oscillator bath spectral density was assumed to be of Ohmic form and the system was analysed using the influence functional techniques outlined in Chapter 2. In this case it was found that the relaxation time associated with the

dark-state, the pure relaxation time with no oscillatory component, was found to be the longest-lived of the three times in the system. This suggests that for the 3-site-V system coupled non-perturbatively to an Ohmic oscillator bath, the dark-state is actually the most robust state and the population trapping mechanism described in Chapter 3, prevalent. The presence of the dark-state serves as a potential hindrance to efficient exciton transfer in the FMO complex. The 3-site-V system was shown in Chapter 3 to have its applications to the FMO complex either as a configuration of three chromophores, or an effective 3-site model for the full FMO system. These results suggest that the FMO complex, with strong system-environment couplings, must avoid these possible trapping states in order to facilitate efficient exciton transfer. Tuning of chromophore energy levels leading to a 3-site-V configuration as used in this analysis has been shown to lead to the formation of a relatively long-lived dark-state in the system. Therefore, one can conclude from this, that the avoidance of tuned chromophore energy levels in the FMO complex is a crucial aspect to facilitating efficient exciton transfer through the system.

Chapter 5

A dual-coupling-spin-boson model for light-harvesting molecules

In this chapter I investigate the effect of non-diagonal couplings on the 2-state-spin-boson (SB) model for both super-ohmic and optical spectral densities. The new model is therefore dubbed the Dual-coupling-spin-boson (DCSB) model. This means that I include not only the coupling of the bath to the diagonal elements of the central system Hamiltonian (σ_z), as is present in the original spin-boson model, but also include couplings to the off-diagonal elements (σ_x) too. The heuristic justification for excluding non-diagonal couplings in the SB model normally relies on the assumption that small tunnelling rate relative to the on-site energy: $\Delta \ll \epsilon$, renders the non-diagonal coupling negligible [31]. Since any interaction to σ_x should be proportional to the wavefunction overlap of the two wells–and is therefore proportional to Δ–the non-diagonal coupling is assumed to be comparatively small.

The problem with this assumption in the context of the SB model is that, while the tunnelling energy is indeed required to be small relative to the bias energy for NIBA to apply, it is not negligibly small. In fact, the SB model is considered such a powerful model because it retains coherence effects up to a degree, and this is because of a small but appreciable tunnelling energy. A perturbative tunnelling energy would actually justify a Fermi's-Golden-Rule approach as we saw in Section 1.4.2, which permits only a one way transfer of energy to the bath and removes any coherence effects. All of this suggests that the SB model is somewhat incomplete without non-diagonal couplings.

Indeed there are a number of problems where non-diagonal couplings are warranted. For example, tunnelling defects in solids interact with their surrounding atoms not only

by a fluctuation of their on-site energies (diagonal coupling) but can emit and absorb phonons (non-diagonal coupling) corresponding to atomic vibrations that modulate the distance between defects. This latter effect should lead to an increase in the well known phenomenon of phonon-assisted tunnelling [128, 99].

Non-diagonal couplings were first discussed by Holstein (1959) [47] in the context of his 'small' polaron model. The first application of these couplings was in the SSH model for polyacetylene [129]. Silbey and Munn [130, 131, 132] later used a canonical transformation method along with numerical approximations to investigate non-diagonal couplings in molecular crystals. In their three part series on electron-phonon coupling, they found that the diffusion coefficient of charge carriers in molecular crystals is dominated by the competition of the two forms of coupling. Since then non-diagonal couplings have seen application to the SB model treated with a two bath approach [55] as well as numerical approaches [133, 134]. Recently we've seen that the inclusion of both diagonal and non-diagonal couplings in the SSH model leads to a sharp transition between the behaviour at weak and strong couplings [50, 79].

5.1 The dual-coupling polaron transformation

For the general case of a bath coupled to the diagonal and non-diagonal elements of the 2-state tunnelling system we have

$$H = \epsilon(\{b_q\})\frac{\sigma_z}{2} + \Delta(\{b_q\})\frac{\sigma_x}{2} + H_B \tag{5.1}$$

where $H_B = \sum_q \omega_q b_q^\dagger b_q$ is the kinetic energy of the bosonic bath. The Pauli spin matrices here are defined as $\sigma_z = |1\rangle\langle 1| - |2\rangle\langle 2|$ and $\sigma_x = |1\rangle\langle 2| + |2\rangle\langle 1|$. Both the on-site energies and transition matrix elements are modulated by the bath in this case. To linear order in the bath couplings [50] (see Section 1.3) we then have

$$H = \frac{\epsilon}{2}\sigma_z + \frac{\Delta}{2}\sigma_x + \frac{\sigma_x}{2}\sum_q \lambda_{x,q}(b_q + b_q^\dagger) + \frac{\sigma_z}{2}\sum_q \lambda_{z,q}(b_q + b_q^\dagger) + H_B \tag{5.2}$$

We can decouple the bath from the central system with the appropriate unitary transformation, which in this case involves a product of the shift operators for the diagonal and non-diagonal couplings respectively

$$U = e^{-S}, \quad S = \frac{\sigma_x}{2}\sum_q u_{x,q}(b_q - b_q^\dagger) + \frac{\sigma_z}{2}\sum_q u_{z,q}(b_q - b_q^\dagger) \tag{5.3}$$

where $u_{x,q} = \lambda_{x,q}/\omega_q$ and $u_{z,q} = \lambda_{z,q}/\omega_q$. Performing the transformation $H \to UHU^T \equiv \tilde{H}$ using the Baker-Campbell-Hausdorff formula

$$\tilde{H} = H - [S,H] + \frac{1}{2!}[S,[S,H]] - \frac{1}{3!}[S,[S,[S,H]]] + \frac{1}{4!}[S,[S,[S,[S,H]]]] + ... \tag{5.4}$$

I find for the the transformed Hamiltonian

$$\tilde{H} = \hat{\epsilon}\sigma_z + \hat{K}_-\sigma_+ + \hat{K}_+\sigma_- + H_B \tag{5.5}$$

where I have introduced the operator notation $\hat{\epsilon}$ to reflect the fact that the on-site energy, in the transformed Hamiltonian picture, is fluctuating due to the non-diagonal coupling. The on-site energy is now

$$\hat{\epsilon} = \frac{\Delta}{2} + \frac{\epsilon}{2}\cosh\left(\hat{\phi}_x\right) - \frac{\Delta}{2}\cosh\left(\hat{\phi}_z\right) \tag{5.6}$$

The kernels are defined as

$$\hat{K}_\pm = \frac{\epsilon}{2} + \frac{\Delta}{2}B_z^\pm - \frac{\epsilon}{2}B_x^\pm \tag{5.7}$$

where

$$\hat{\phi}_x = \sum_q u_{x,q}(b_q - b_q^\dagger), \quad \hat{\phi}_z = \sum_q u_{z,q}(b_q - b_q^\dagger) \tag{5.8}$$

I identify the boson shift operators [52, 61, 99]

$$B_\pm^x = \exp\left(\pm\hat{\phi}_x\right), \quad B_\pm^z = \exp\left(\pm\hat{\phi}_z\right) \tag{5.9}$$

One can also verify that the transformed Hamiltonian reduces to the 2-state tunnelling Hamiltonian with the system-bath coupling turned off.

5.2 Dynamics of the dual-coupling-spin-boson model

The time evolution of the system is governed by the reduced density matrix $\rho_s(t)$. The probabilities for each state are therefore $\langle\sigma_f|\,\rho_s(t)\,|\sigma_f'\rangle \equiv \rho_s(\sigma_f,\sigma_f';t)$, and can be described in the Feynman-Vernon path integral formalism as

$$\rho_s(\sigma_f,\sigma'_f;t)=\sum_{\sigma_i,\sigma'_i}\int_{\sigma_i}^{\sigma_f}D\sigma(\tau)\int_{\sigma'_i}^{\sigma'_f}D\sigma'(\tau')e^{iS_0[\sigma(\tau)]-iS_0[\sigma'(\tau')]}F[\sigma(\tau),\sigma'(\tau')]\rho_s(\sigma_i,\sigma'_i;0) \tag{5.10}$$

where $\sigma_f=\sigma(\tau=t),\sigma'_f=\sigma'(\tau'=t),\sigma_i=\sigma(\tau=0),\sigma'_i=\sigma'(\tau'=0)$ are paths that visit the two states in the central system $\sigma,\sigma'\in\{|1\rangle,|2\rangle\}$. The paths σ,σ' in the central system are coupled via the influence functional $F[\sigma,\sigma']$, which incorporates all of the effects of the bath. Since the bath has been decoupled from the central system via the dual-coupling polaron transformation, the transformed Hamiltonian $\tilde{H}$ of equation 5.5 corresponds to a transformed action for the central system $\tilde{S}_0$. Therefore the reduced density matrix for the transformed action

$$\rho_s(\sigma_f,\sigma'_f;t)=\left\langle\sum_{\sigma_i,\sigma'_i}\int_{\sigma_i}^{\sigma_f}D\sigma(\tau)\int_{\sigma'_i}^{\sigma'_f}D\sigma'(\tau')e^{i\tilde{S}_0[\sigma(\tau)]-i\tilde{S}_0[\sigma'(\tau')]}\rho_s(\sigma_i,\sigma'_i;0)\right\rangle_B \tag{5.11}$$

contains the effects of the bath in the transformed probability amplitudes, and the trace over the bath degrees of freedom leaves the dynamics in terms of central system variables only. The transformed probability amplitudes are

$$\tilde{A}_{\sigma_f,\sigma_i}(t)\equiv\int_{\sigma_i}^{\sigma_f}D\sigma(\tau)e^{i\tilde{S}_0[\sigma(\tau)]}=\langle\sigma_f|\,e^{-i\tilde{H}t/\hbar}\,|\sigma_i\rangle \tag{5.12}$$

The effects of the bath enter via the transformed on-site energies $\pm\epsilon/2\,|\pm\rangle\langle\pm|\rightarrow\pm\hat{\epsilon}\,|\pm\rangle\langle\pm|$, and transition matrix elements $\Delta\sigma_\pm\rightarrow K_\mp\sigma_\pm$, which are now operators containing the bath shift operators $\hat{B}_\pm$. In this formalism, the probability amplitudes can be calculated independently, and the trace over the bath degrees of freedom performed to obtain a closed expression for the central system dynamics. Expanding each transition amplitude for the density matrix, following the analysis outlined in Section 3.1.2 gives

$$\begin{aligned}\rho_s(1,1;t)=\Bigg\langle&\left(1-\int_0^t dt_2\int_0^{t_2}dt_1e^{-2i\tilde{\epsilon}(t_2-t_1)}K_+(t_2)K_-(t_1)+...\right)\\&\times\left(1-\int_0^t dt_2\int_0^{t_2}dt_1e^{2i\tilde{\epsilon}(t_2-t_1)}K_-(t_2)K_+(t_1)+...\right)\Bigg\rangle_B\end{aligned} \tag{5.13}$$

where the density matrix element corresponding to the probability to start and end in state $|1\rangle$ was chosen. For clarity the ground state energy has been shifted to state $|1\rangle$,

such that $\epsilon_1 = 0$, and the amplitude for no transitions $\tilde{A}_{11}^{(0)}(t)$=1. Therefore the energy of state $|2\rangle$ is $\epsilon_2 = -2\hat{\epsilon}$. Collecting terms

$$\rho_s(1,1;t) = 1 - \int_0^t dt_2 \int_0^{t_2} dt_1 \tilde{\Upsilon}(t_1,t_2) + \int_0^t dt_4 \int_0^{t_4} dt_3 \int_0^{t_3} dt_2 \int_0^{t_2} dt_1 \tilde{\Upsilon}(t_1,t_2)\tilde{\Upsilon}(t_3,t_4) + ... \tag{5.14}$$

The kernel acting at times t, t' is therefore

$$\tilde{\Upsilon}(t,t') = \left\langle e^{i2\hat{\epsilon}(t-t')/\hbar} K_+(t)K_-(t') \right\rangle_B + \left\langle e^{-i2\hat{\epsilon}(t-t')/\hbar} K_-(t)K_+(t') \right\rangle_B \tag{5.15}$$

where NIBA has been invoked such that

$$\left\langle K_+(t_1)K_-(t_2)K_+(t_3)K_-(t_4) \right\rangle_B \equiv \left\langle K_+(t_1)K_-(t_2) \right\rangle_B \left\langle K_+(t_3)K_-(t_4) \right\rangle_B \tag{5.16}$$

and only correlations between successive bath fluctuations are permitted. This approximation is valid when the system spends vastly more time in diagonal states of the density matrix compared to off-diagonal states (see Section 2.5). Separating the transformed on-site energy in to the sum of its average value $\tilde{\epsilon} \equiv \langle \hat{\epsilon} \rangle$, and fluctuations about its mean value $\delta\hat{\epsilon}$, leads to $\hat{\epsilon} \equiv \tilde{\epsilon} + \delta\hat{\epsilon}$. Now the Kernel reads

$$\tilde{\Upsilon}(t,t') = e^{i2\tilde{\epsilon}(t-t')/\hbar} \left\langle e^{i2\delta\hat{\epsilon}(t-t')/\hbar} K_+(t)K_-(t') \right\rangle_B + e^{-i2\tilde{\epsilon}(t-t')/\hbar} \left\langle e^{-i2\delta\hat{\epsilon}(t-t')/\hbar} K_-(t)K_+(t') \right\rangle_B \tag{5.17}$$

The system is solved by taking the Laplace transform of the density matrix

$$\rho_s(1,1;\lambda) = \frac{1}{\lambda} - \mathscr{L}\left[\int_0^t dt_2 \int_0^{t_2} dt_1 \tilde{\Upsilon}(t_1,t_2) \right] + \mathscr{L}\left[\int_0^t dt_4 \int_0^{t_4} dt_3 \int_0^{t_3} dt_2 \int_0^{t_2} dt_1 \tilde{\Upsilon}(t_1,t_2)\tilde{\Upsilon}(t_3,t_4) \right] + ... \tag{5.18}$$

and the Laplace-transform of the Kernel is therefore

$$\tilde{\Upsilon}(\lambda) = \int_0^\infty dt e^{-\lambda t}\left[e^{i2\tilde{\epsilon}t/\hbar}\Big\langle e^{i2\delta\hat{\epsilon}t/\hbar}K_+(t)K_-(t)\Big\rangle_B + e^{-i2\tilde{\epsilon}t/\hbar}\Big\langle e^{-i2\delta\hat{\epsilon}t/\hbar}K_-(t)K_+(t)\Big\rangle_B\right] \tag{5.19}$$

The fluctuations of the on-site energy $\delta\hat{\epsilon}$ come from the shift operators $\delta B_\pm$. They introduce terms in the integrand that go like $e^{-i\epsilon\delta B_\pm t/\hbar}$. These terms become rapidly oscillating functions, and by the stationary phase approximation, integrate to zero for large arguments of the phase. Therefore I can approximate this integral as

$$\tilde{\Upsilon}(\lambda) = \int_0^\infty dt e^{-\lambda t}\left[e^{i2\tilde{\epsilon}t/\hbar}\Big\langle K_+(t)K_-(t)\Big\rangle_B + e^{-i2\tilde{\epsilon}t/\hbar}\Big\langle K_-(t)K_+(t)\Big\rangle_B\right] \tag{5.20}$$

The functions $\Big\langle K_+(t)K_-(t')\Big\rangle_B$ describe the interactions of successive flips within the system - dragging their respective boson clouds with them, and are multiplied by a prefactor corresponding to the kinetic energy term of the Hamiltonian. So I retain only the average of the fluctuating on-site energy

$$\begin{aligned}\tilde{\epsilon} &= \frac{\Delta}{2} + \frac{\epsilon}{2}\Big\langle \cosh\big(\phi_x\big)\Big\rangle_B - \frac{\Delta}{2}\Big\langle \cosh\big(\phi_z\big)\Big\rangle_B \\ &= \frac{\Delta}{2} + \frac{\epsilon}{2}\langle B_x\rangle_B - \frac{\Delta}{2}\langle B_z\rangle_B\end{aligned} \tag{5.21}$$

Laplace transforming $\rho_S(1,1;t)$ leads to the geometric series summation

$$\rho_S(1,1;\lambda) = \sum_{n=0}^{\infty}(-1)^{2n}\frac{\tilde{\Upsilon}(\lambda)^n}{\lambda^{n+1}} = \frac{1}{\lambda + \tilde{\Upsilon}(\lambda)} \tag{5.22}$$

The Kernel is expanded to

$$\begin{aligned}\tilde{\Upsilon}(\lambda) = \frac{1}{2}\int_0^\infty dt e^{-\lambda t}\Big\{ &\cos(2\tilde{\epsilon}t)\Big[\epsilon^2\big(1-2\mathbb{B}_x\big) + 2\epsilon\Delta\mathbb{B}_z\Big] \\ &+ \epsilon^2\mathbb{B}_x^2 f_{xx}(t) + \Delta^2\mathbb{B}_z^2 f_{zz}(t) - 2\epsilon\Delta\mathbb{B}_x\mathbb{B}_z f_{xz}(t)\Big\}\end{aligned} \tag{5.23}$$

Paying close attention to the distinction here between diagonal and non-diagonal couplings, the bath correlation functions are calculated following Mahan [52] and are found to be

$$\langle B^{\alpha}_{\pm}(t)B^{\beta}_{\mp}(0)\rangle_B = \langle B^{\alpha}_{\pm}\rangle\langle B^{\beta}_{\mp}\rangle e^{\varphi_{\alpha\beta}(t)} \tag{5.24}$$

where the indices $\alpha, \beta \in \{x, z\}$, and $\langle B^{\alpha}_{\pm}(t)B^{\beta}_{\mp}(0)\rangle_B = \langle B^{\alpha}_{\mp}(t)B^{\beta}_{\pm}(0)\rangle^{\dagger}_B$. The phase

$$\varphi_{\alpha\beta}(t) = iQ'_{\alpha\beta}(t) + Q''_{\alpha\beta}(t) \tag{5.25}$$

is comprised of the functions

$$\begin{aligned} Q'_{\alpha\beta}(t) &= \int_0^{\infty} d\omega \frac{\sqrt{J_{\alpha}(\omega)J_{\beta}(\omega)}}{\hbar\omega^2}\sin(\omega t) \\ Q''_{\alpha\beta}(t) &= \int_0^{\infty} d\omega \frac{\sqrt{J_{\alpha}(\omega)J_{\beta}(\omega)}}{\hbar\omega^2}\cos(\omega t)\coth(\hbar\beta\omega/2) \end{aligned} \tag{5.26}$$

The biased influence functionals, within NIBA, are therefore

$$f_{\alpha\beta}(t) = \mathbb{B}_{\alpha}\mathbb{B}_{\beta}\cos\left[2\tilde{\epsilon}t + Q'_{\alpha\beta}(t)\right]e^{Q''_{\alpha\beta}(t)} \tag{5.27}$$

The spectral density function $J_{\alpha}(\omega) = (\pi/2)\sum_q(\lambda^2_{\alpha,q}/\omega_q)\delta(\omega - \omega_q)$ describes the distribution of bath modes weighted by their coupling to the exciton. The terms $\mathbb{B}_x \equiv \langle B^x_{\pm}\rangle_B$, $\mathbb{B}_z \equiv \langle B^z_{\pm}\rangle_B$ are the Debye-Waller factors, which can be cast in the continuum limit as [61]

$$\langle B^{\alpha}_{\pm}\rangle_B = \exp\Big[-\int_0^{\infty} d\omega \frac{J_{\alpha}(\omega)}{\omega^2}\coth(\beta\omega/2)\Big] \tag{5.28}$$

We see that the Debye-Waller factor has an infra-red divergence for Ohmic spectral densities leading to an orthogonality catastrophe [61], however for super-Ohmic spectral densities the integral is infrared convergent, reflecting the probability for the system to tunnel between wells without exciting the bath.

It's prudent to check that when the non-diagonal coupling $\zeta_x \to 0$ is turned off, we recover the spin-boson-model influence function result with just diagonal coupling ζ_z. One can verify that this indeed the case. One can also verify that by turning off the bath entirely–both diagonal and non-diagonal couplings, we recover the eigenvalues of the 2-site tunnelling Hamiltonian. In this case the pole structure for the propagator reduces to

$$\lambda^2 + \epsilon^2 + \Delta^2 = 0, \rightarrow \lambda = \pm i\sqrt{\epsilon^2 + \Delta^2} \tag{5.29}$$

which is the pole structure for the propagator of the isolated 2-site system.

5.3 Super-Ohmic spectral densities in the DCSB model

I now turn to the case of a bath characterised by a super-Ohmic spectral density. In this case the spectral density takes the form

$$J_x(\omega) = \rho_x \frac{\omega^3}{\omega_{ph}^2} e^{-\omega/\omega_c}, \quad J_z(\omega) = \rho_z \frac{\omega^3}{\omega_{ph}^2} e^{-\omega/\omega_c} \tag{5.30}$$

where in section 2.3.2 I defined a dimensionless coupling constant for acoustic phonons as

$$\zeta_\alpha = \frac{\rho_\alpha}{\pi\hbar} \tag{5.31}$$

The first step in evaluating the super-Ohmic influence functional is to do the frequency integrals in $Q'(t), Q''(t)$ given in their general form in equation 4.2. For the super-Ohmic phonon density of states they take the form

$$\begin{aligned} Q'_{ph}(t) &= \int_0^\infty d\omega\, \omega e^{-\omega/\omega_c} \sin(\omega t) \\ Q''_{ph}(t) &= \int_0^\infty d\omega\, \omega e^{-\omega/\omega_c} (1 - \cos(\omega t)) \coth(\hbar\beta\omega/2) \end{aligned} \tag{5.32}$$

which appear in the individual influence functionals

$$\tilde{f}_\alpha(t) = \frac{1}{2} \cos\big(2\tilde{\epsilon}t + \zeta_\alpha Q'_{ph}(t)/\omega_{ph}^2\big) \exp\big(-\zeta_\alpha Q''_{ph}(t)/\omega_{ph}^2\big) \tag{5.33}$$

and the indices form the set $\alpha \in \{z, x, xz\}$. Next I split up the second bath correlator in to its time-independent and time-dependent parts

$$Q''_{ph}(t) = Q''_0 - \tilde{Q}''_{ph}(t) \tag{5.34}$$

The time-independent term is therefore

$$Q_0'' = \int_0^\infty d\omega\, \omega e^{-\omega/\omega_c} \coth(\hbar\beta\omega/2) \tag{5.35}$$

which leads to the adiabatic phonon dressing of the tunnelling matrix element [34]. The exponentiation of this time-independent term can be factorised out from the full influence functional and the corresponding factor that is absorbed into the tunnelling matrix element is known as the Debye-Waller factor [99]. This term serves to renormalise parameters due to thermal excitations of the polaron cloud [34]. The integral I calculate to be

$$Q_0'' = -\omega_c^2 + 2\left(\frac{k_B T}{\hbar}\right)^2 \psi'\left(\frac{k_B T}{\hbar\omega_c}\right) \tag{5.36}$$

Expanding to 2nd-order in $k_B T \ll \hbar\omega_c \ll 1$ produces

$$Q_0'' \sim \omega_c^2 + \frac{1}{3}\left(\frac{\pi k_B T}{\hbar}\right)^2 + 2\frac{\psi''(1)}{\omega_c}\left(\frac{k_B T}{\hbar}\right)^3 + \frac{\pi^4 (k_B T)^4}{15\hbar^4\omega_c^2} \tag{5.37}$$

I absorb these terms into the renormalisation factors defined earlier

$$\mathbb{B}_z = e^{-\theta_{zz}}, \quad \mathbb{B}_x = e^{-\theta_{xx}}, \quad \mathbb{B}_{xz} = e^{-\theta_{xz}} \tag{5.38}$$

where

$$\theta_{zz} = \zeta_z Q_0''/\omega_{ph}^2, \quad \theta_{xx} = \zeta_x Q_0''/\omega_{ph}^2, \quad \theta_{xz} = \sqrt{\zeta_x\zeta_z} Q_0''/\omega_{ph}^2 \tag{5.39}$$

The time-dependent part of the influence phase left over is

$$\varphi(t) = iQ_{ph}'(t) + \tilde{Q}_{ph}''(t) \tag{5.40}$$

Defining a complex time-variable

$$\tau = t - i\hbar\beta/2 \tag{5.41}$$

the phase can be cast in the convenient form for the phonon-phase in the complex time-domain

$$\tilde{f}_{\alpha\beta}(\tau) = \mathrm{Re}\left\{\exp\left[\varphi_{\alpha\beta}(\tau)/\omega_c^2 + 2i\tilde{\epsilon}(\tau + i\hbar\beta/2)\right]\right\} \tag{5.42}$$

Computing the frequency integral using known integrals (Section 4.13 in [126]) yields

$$\varphi(\tau) = \frac{1}{(\hbar\beta)^2}\left[\psi'\left(\frac{1}{2} + \frac{1 - i\omega_c\tau}{\hbar\omega_c\beta}\right) + \psi'\left(\frac{1}{2} + \frac{1 + i\omega_c\tau}{\hbar\omega_c\beta}\right)\right] \tag{5.43}$$

where the polygamma functions are defined

$$\psi_n(z) = \frac{d^n}{dz^n}\psi_0(z), \quad \psi_0(z) = \frac{d^n}{dz^n}\ln\left[\Gamma(z)\right] \tag{5.44}$$

Analytic continuation of the phase back to the real axis yields

$$\varphi_{\alpha\beta}(t) = \frac{\sqrt{\zeta_\alpha\zeta_\beta}}{(\hbar\beta)^2}\left[\psi'\left(\frac{1 - i\omega_c t}{\hbar\omega_c\beta}\right) + \psi'\left(\frac{1 + \hbar\omega_c\beta + i\omega_c t}{\hbar\omega_c\beta}\right)\right] \tag{5.45}$$

As it stands, the Laplace transforms of the individual influence functionals in Equation 5.23, are intractable. In the interest of exploring physiological temperatures, where $k_BT = 27\text{meV}$ ($T = 300K$), and phonon cut-off frequencies $\omega_c = 8.7\text{meV}$ [98], we can expand in the parameter $\hbar\omega_c\beta \ll 1$. Asymptotic expansion of Equation 5.45 to third order yields

$$\begin{gathered}\varphi_{\alpha\beta}(t) \approx \Theta_{\alpha\beta} + i\phi_{\alpha\beta}t - \Phi_{\alpha\beta}t^2 \\ \Theta_{\alpha\beta} = \sqrt{\zeta_\alpha\zeta_\beta}\left(\frac{2\omega_c}{\beta} + \frac{\omega_c^3\beta}{3}\right), \ \phi_{\alpha\beta} = 2\sqrt{\zeta_\alpha\zeta_\beta}\omega_c^3, \\ \Phi_{\alpha\beta} = \frac{2\sqrt{\zeta_\alpha\zeta_\beta}\omega_c^3}{\beta}\end{gathered} \tag{5.46}$$

It now remains to evaluate the Laplace transform of the propagator.

5.4 High-temperature limit in the super-Ohmic NDSB model

As they stand, the influence functionals produce a pole structure in the propagator of Equation 5.22 of infinite order in λ, representing all possible excited states of the system across the whole temperature range. In the interest of keeping the system-bath couplings to all orders, I can investigate certain temperature limits. In the high-temperature limit I can expand the influence phase in the small quantity $\lambda\beta \ll 1$. the biased influence functional can be Taylor expanded to 1st-order as

$$\tilde{f}_{\alpha\beta} = \tilde{f}^0_{\alpha\beta} - \tilde{f}^1_{\alpha\beta}\lambda \tag{5.47}$$

where the coefficients are

$$\begin{aligned}
\tilde{f}^0_{\alpha\beta} &= e^{\Theta_{\alpha\beta}} \int_0^\infty dt \cos(2\tilde{\epsilon}t + \phi_{\alpha\beta}t) e^{-\Phi_{\alpha\beta}t^2} \\
\tilde{f}^1_{\alpha\beta} &= e^{\Theta_{\alpha\beta}} \int_0^\infty dt\, t \cos(2\tilde{\epsilon}t + \phi_{\alpha\beta}t) e^{-\Phi_{\alpha\beta}t^2}
\end{aligned} \tag{5.48}$$

The time interval in $\tilde{f}^0_{\alpha\beta}$ can be evaluated with the known integral BI (263)(5) in [126] to be

$$\tilde{f}^0_{\alpha\beta} = \frac{e^{\Theta_{\alpha\beta}}}{2}\sqrt{\frac{\pi}{\Phi_{\alpha\beta}}}\exp\left[-\frac{(2\tilde{\epsilon}+\phi_{\alpha\beta})^2}{4\Phi_{\alpha\beta}}\right] \tag{5.49}$$

The first order coefficient $\tilde{f}^1_{\alpha\beta}$ can be evaluated using the known integral BI (362)(2) in [126] and the Maclaurin series of the Dawson function [135] $D(x) = \sum_{n=0}^{\infty}(-2)^n x^{2n+1}/(2n+1)!!$, to get

$$\tilde{f}^1_{\alpha\beta} = \frac{e^{\Theta_{\alpha\beta}}}{2\Phi_{\alpha\beta}} - \frac{e^{\Theta_{\alpha\beta}}}{2\Phi^{3/2}_{\alpha\beta}}(2\tilde{\epsilon}+\phi_{\alpha\beta})D\left(\frac{2\tilde{\epsilon}+\phi_{\alpha\beta}}{2\sqrt{\Phi_{\alpha\beta}}}\right) \tag{5.50}$$

The pole structure of the propagator now takes the form

$$\lambda + \frac{\big(\epsilon^2\big(1-2\mathbb{B}_x\big) + 2\epsilon\Delta\mathbb{B}_z\big)\lambda}{2(\lambda^2+4\tilde{\epsilon}^2)} + \Upsilon_0 - \Upsilon_1\lambda = 0 \tag{5.51}$$

where

$$\begin{aligned}
\Upsilon_0 &= \Delta^2\mathbb{B}^2_z\tilde{f}^0_z + \epsilon^2\mathbb{B}^2_x\tilde{f}^0_x - 2\Delta\epsilon\mathbb{B}_x\mathbb{B}_z\tilde{f}^0_{xz} \\
\Upsilon_1 &= \Delta^2\mathbb{B}^2_z\tilde{f}^1_z + \epsilon^2\mathbb{B}^2_x\tilde{f}^1_x - 2\Delta\epsilon\mathbb{B}_x\mathbb{B}_z\tilde{f}^1_{xz}
\end{aligned} \tag{5.52}$$

Rearranging the pole structure to

$$2(1-\Upsilon_1)\lambda^3 + 2\lambda^2\Upsilon_0 + \lambda\big(2\epsilon^2\big(1-2\mathbb{B}_x\big) + 4\epsilon\Delta\mathbb{B}_z + 8\tilde{\epsilon}^2 - 4\tilde{\epsilon}^2\Upsilon_1\big) + 8\tilde{\epsilon}^2\Upsilon_0 = 0 \quad (5.53)$$

The solutions of the cubic equation are obtained using the analysis framework of Appendix E. For the poles I find

$$\begin{aligned}\lambda_r &= \Gamma_\gamma - \Gamma_\theta \\ \lambda_\phi &= -\frac{\Gamma_\gamma}{2} - \Gamma_\theta \pm i\omega\end{aligned} \quad (5.54)$$

where

$$\begin{aligned}\Gamma_\theta &= \frac{\Upsilon_0}{3(1-\Upsilon_1)}, \quad \Gamma_\gamma = u - v, \quad \omega = \frac{\sqrt{3}}{2}(u+v) \\ u &= \sqrt[3]{\sqrt{D} - \frac{q}{2}}, \quad \forall D > 0 \\ v &= \sqrt[3]{\sqrt{D} + \frac{q}{2}}, \quad \forall D > 0 \\ q &= \frac{2(\Upsilon_0/(1-\Upsilon_1))^3 - 9(\Upsilon_0\Xi)/(4(1-\Upsilon_1)^2) + 108\tilde{\epsilon}^2\Upsilon_0/(4(1-\Upsilon_1))}{27} \\ p &= \frac{3\Xi/(4(1-\Upsilon_1) - \Upsilon_0^2/(1-\Upsilon_1)^2}{3} \\ \Xi &= \epsilon^2\big(1-2\mathbb{B}_x\big) + 2\epsilon\Delta\mathbb{B}_z + 4\tilde{\epsilon}^2 - 4\tilde{\epsilon}^2\Upsilon_1\end{aligned} \quad (5.55)$$

The entirely real pole $\lambda_r \equiv \Gamma_r$ represents the pure relaxation rate. This pole leads to a term describing exponential relaxation in the time regime upon Laplace inversion. The inverse of Γ_r represents the inverse time scale for relaxation of the system to its ground state, and is therefore interpreted as the exciton transfer time through the sysytem. The real part of the other two poles $\Gamma_\phi \equiv \mathrm{Re}[\lambda_\phi]$ is the decoherence rate describing the inverse timescale for the loss of phase coherence in the system. It manifests as the damping rate of the oscillatory terms in the dynamics upon Laplace-inversion [61].

$$D = \left(\frac{q}{2}\right)^2 + \left(\frac{p}{3}\right)^3 \quad (5.56)$$

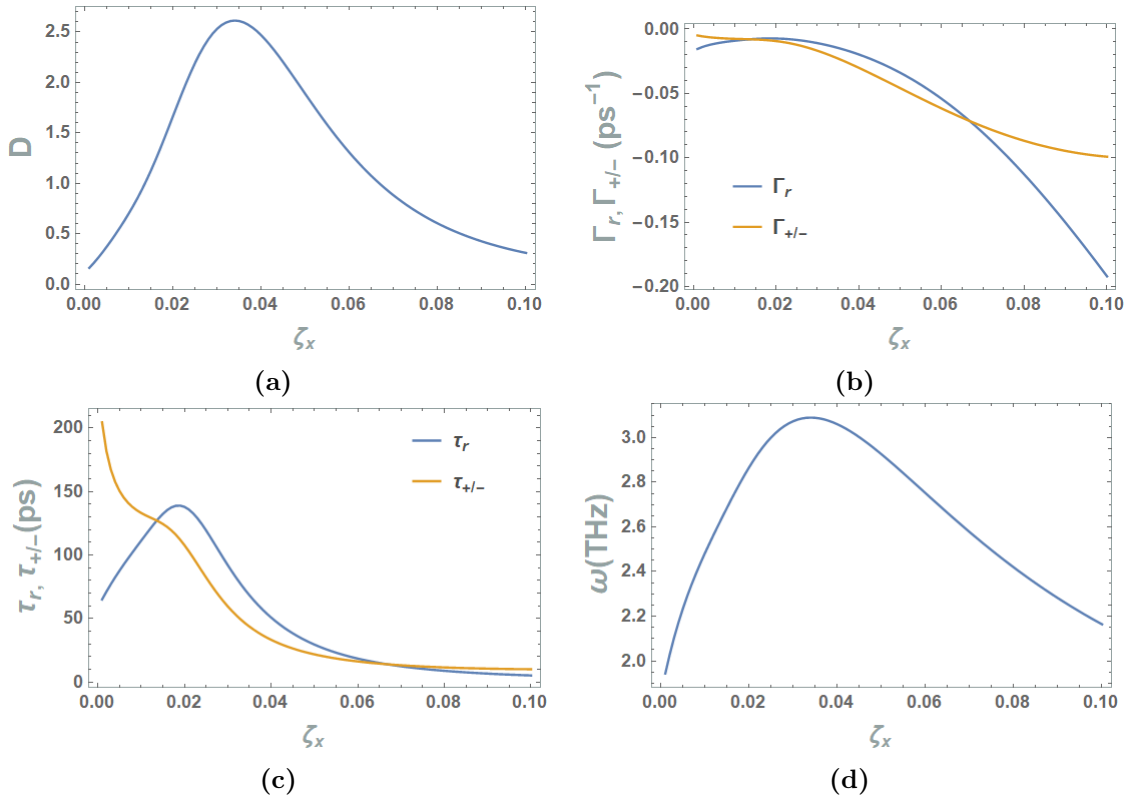

Figure 5.1: Phase space, decay rates and oscillation frequency for Non-diagonal-SB model vs ζ_x. $\zeta_z = 1$. Parameters: $\epsilon = 1$, $\Delta = 0.3$, $k_B T = 5$, $\omega_c = 0.1$. In units of ϵ.

In Figure 5.1 the results for the DCSB model are presented as a function of non-diagonal coupling strength ζ_x. The discriminant D remains positive, therefore the system remains in the coherent phase for $0 < \zeta_x \ll \zeta_z$. However this just means that the exciton has some oscillatory component to its dynamics. The duration of these oscillations can be seen in Figure c. The timescale associated with the decay of the exciton oscillations is $\tau_\phi \equiv \tau_\pm$, and we see that it remains longer than the exciton transfer time τ_r for small values of ζ_x. In the intermediate regime of ζ_x, for the range considered here, the coherence time falls below the exciton transfer time. For larger values of ζ_x we see the coherence time is once again longer than τ_r. In Figure d the effect of phonon-assisted transport (normally associated with the oscillation frequency) can be seen by continuously varying the non-diagonal coupling parameter γ_x, and the dimer oscillation frequency rises. For high enough values of γ_x, however, we see ω reduce rapidly due to an 'over dressing' of the particle's phonon cloud [52] i.e it becomes more difficult for the particle to tunnel between wells as it gets heavier. Therefore, while the non-diagonal coupling serves as an additional

decoherence mechanism in the system, it suppresses coherence at a slower rate than the exciton transfer time. This means that the exciton moves rapidly through the dimer system while remaining coherent for the duration of its transfer between chromophores.

5.4.1 DCSB model for the FMO system with acoustic phonons

I now apply the DCSB model with super-Ohmic spectral densities to a dimer of two chromophores in the FMO complex. I use the excitation energies of the chromophores and the inter-chromophore tunnelling energies determined in Section 1.5. The strength of the diagonal system-environment coupling was discussed in Section 2.3.2.

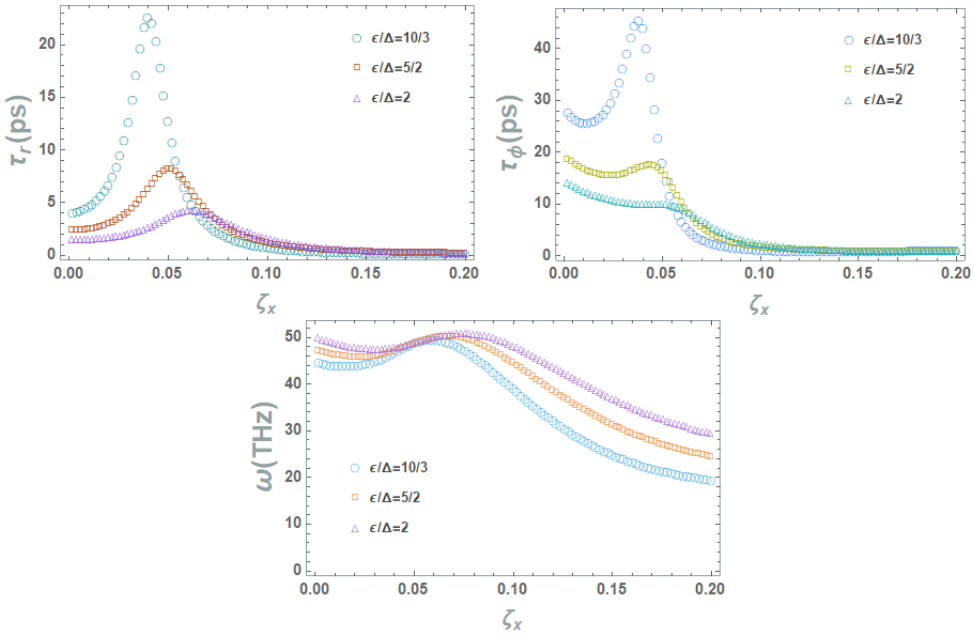

Figure 5.2: Exciton transfer time τ_r, coherence time τ_ϕ, and dimer oscillation frequency ω as a function of non-diagonal coupling strength ζ_x. Parameters: $\epsilon = 20\text{meV}$, $\zeta_z + \zeta_x = 1$, $k_BT = 27\text{meV}$, $\omega_c = 8.7\text{meV}$. Bath spectral density of super-Ohmic form: $J_{(x,z)}(\omega) = \pi\hbar\zeta_{(x,z)}(\omega^3/\omega_c^2)\exp(-\omega/\omega_c)$.

In Figure 5.2 we see how varying the system-bath coupling strength affects the exciton transfer time, coherence time and oscillation frequency of the dimer with both diagonal and non-diagonal couplings. We observe the increase in dimer oscillation frequency as ζ_x is varied for small ζ_x. Along with this increase in oscillation frequency, the transfer time is seen to also increase. This can be interpreted as coherent tunnelling back and

forth within the dimer, as the density of states available to the exciton increases with phonon-assisted tunnelling. For large enough non-diagonal coupling strength, the transfer time is seen to rapidly decrease as the exciton tunnelling becomes one-way. At the same time the exciton coherence time is seen to decrease with the additional decoherence mechanism provided by the non-diagonal coupling. However, the coherence time is seen to remain persistently longer than the transfer time, indicating the exciton is coherent for the duration of its motion.

The sum of diagonal and non-diagonal coupling strengths used for these calculations was $\zeta_z + \zeta_x = 1$. This number can be determined from the experimentally determined reorganisation energy of a super-Ohmic spectral density bath model for the FMO complex. This was discussed in Section 2.3. The non-diagonal coupling strength for the FMO complex has not been experimentally measured yet and is therefore kept a free parameter in the results.

5.5 The DCSB model coupled to optical phonons

In this section I model the environment as an oscillator bath comprised of optical phonons with frequency ω_0. We saw in Section 2.3.4, how the experimentally determined spectra for biomolecules actually contain structure beyond a continuous distribution of low-frequency modes. Sharp optical transition peaks were observed revealing the presence of discrete oscillation modes present in the environment of the biomolecule. Therefore, I would like to investigate the effect of including optical phonon modes in the spectral density of the DCSB model. Considering an optical phonon spectral density with spectral broadening of, the spectral density function takes the form

$$J_\alpha(\omega) = \lambda_\alpha e^{-(\omega-\omega_0)^2/2\xi^2} \tag{5.57}$$

where ω_0 is the optical phonon frequency, λ_x, λ_z the non-diagonal and diagonal coupling energies respectively and ξ the peak width. The dimensionless coupling constant for optical phonons is $\nu_\alpha = \lambda_\alpha \xi / \pi\omega_0^2$. We see that the optical phonon coupling scales linearly with the spectral weight $\lambda\xi$ and with the inverse of the optical phonon frequency squared. Therefore optical phonon peaks at high frequency with relatively small spectral weight couple weakly to the exciton. In the interest of studying non-perturbative effects we therefore consider relatively low-frequency optical phonons.
The influence phase in complex time is now

$$\varphi_{\alpha\beta}(\tau) = \sqrt{\nu_\alpha \nu_\beta} \int_0^\infty \frac{d\omega}{\omega^2} e^{-(\omega-\omega_0)^2/2\xi^2} \cos(\omega\tau)\mathrm{csch}(\hbar\beta\omega/2) \tag{5.58}$$

The frequency integral can be evaluated with the use of the saddle-point approximation since for light-harvesting molecules, the optical phonon peaks have a very narrow linewidth ξ. This means that the prefactor to the argument of the Gaussian exponential spectral function $x = 1/2\xi^2$ is very large, and the peak therefore very narrow around the point ω_0. We find for the Gaussian-optical phonon influence phase

$$\varphi_{\alpha\beta}(\tau) = \frac{\xi\sqrt{2\pi\lambda_\alpha\lambda_\beta}}{\pi\hbar\omega_0^2} \cos(\omega_0\tau)\mathrm{csch}(\hbar\beta\omega_0/2) \tag{5.59}$$

and for the Debye-Waller factors

$$\mathbb{B}_\alpha = \exp\left(-\nu_\alpha\sqrt{2\pi}\coth\hbar\beta\omega_0/2\right) \tag{5.60}$$

Expanding the influence phase in the limit $\omega_0\tau \ll 1$ produces a Gaussian integral

$$\varphi_{\alpha\beta}(\tau) \approx \frac{\xi\sqrt{2\pi\lambda_\alpha\lambda_\beta}}{\pi\hbar\omega_0^2}\left(1-\omega_0^2\tau^2\right)\mathrm{csch}(\hbar\beta\omega_0/2) \tag{5.61}$$

Analytically continuing $\varphi(\tau)$ to the real time axis and evaluating the first two terms of $\varphi(\lambda)$, again expanded in $\lambda\beta \ll 1$, yields

$$\begin{aligned}
\tilde{f}^0_{\alpha\beta} &= \frac{e^{\Lambda_{\alpha\beta}}}{2}\sqrt{\frac{\pi}{\Lambda_{\alpha\beta}\omega_0^2}}\exp\left[-\frac{(2\tilde{\epsilon}+\Lambda_{\alpha\beta}\omega_0^2\beta)^2}{4\Lambda_{\alpha\beta}\omega_0^2}\right] \\
\tilde{f}^1_{\alpha\beta} &= \frac{e^{\Lambda_{\alpha\beta}}}{2(\Lambda_{\alpha\beta}\omega_0^2)^{3/2}}\left[\sqrt{\Lambda_{\alpha\beta}\omega_0^2}\right. \\
&\quad \left. -(\Lambda_{\alpha\beta}\omega_0^2\hbar\beta+2\tilde{\epsilon})D\left(\frac{2\tilde{\epsilon}+\Lambda_{\alpha\beta}\omega_0^2\hbar\beta}{2\sqrt{\Lambda_{\alpha\beta}\omega_0^2}}\right)\right]
\end{aligned} \tag{5.62}$$

where $\Lambda_{\alpha\beta} = \sqrt{2\pi\nu_\alpha\nu_\beta}\mathrm{csch}(\hbar\beta\omega_0/2)$. The poles of the density matrix propagator with optical phonons is then given by substituting Equations 5.62 and 5.60 in to the density matrix of Equation 5.22.

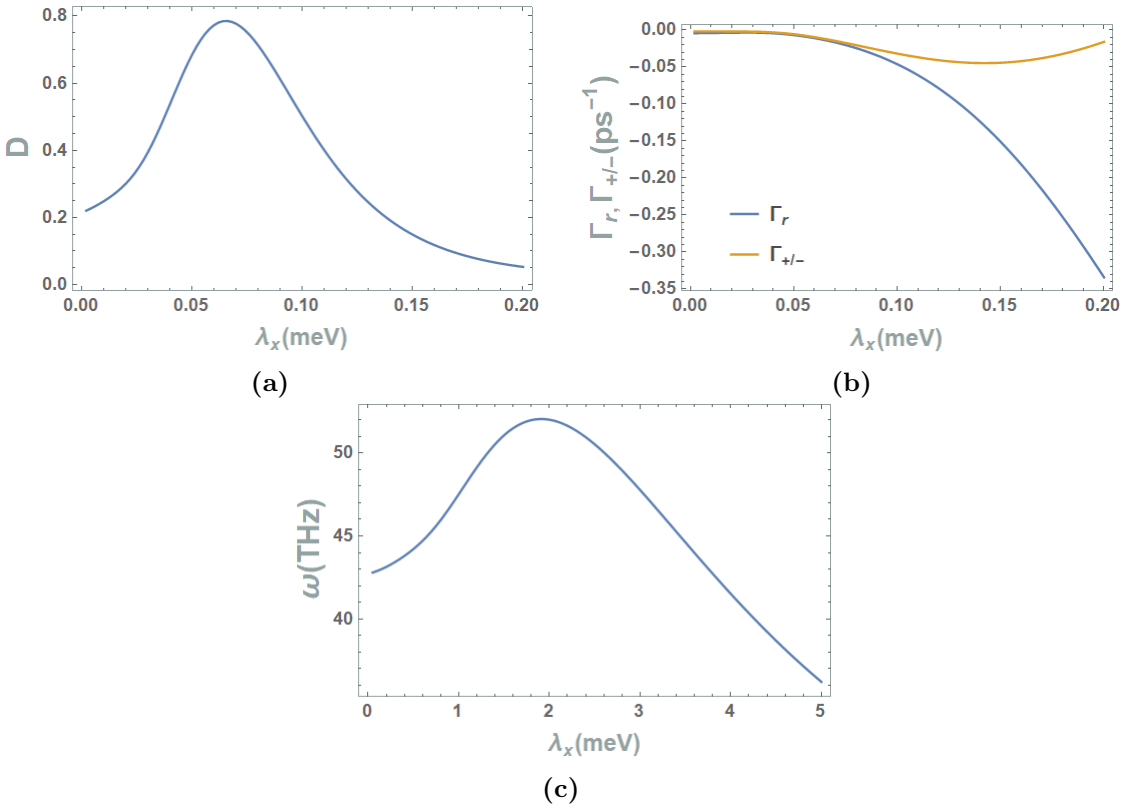

Figure 5.3: (a) $\tilde{\Delta} = 0.3$, $\epsilon = 1$, $k_BT = 1$, $\omega_o = 0.4$, $\xi = 0.01$, $\lambda_z = 5$ in units of (meV).

In Figure 5.3, the results for the DCSB model are presented in the low temperature regime $k_BT = 0.1$. The discriminant D remains positive and the system is therefore persistently in the coherent phase. As the non-diagonal coupling energy λ_x is turned, the oscillation frequency of the dimer is seen to increase in accordance with the phonon-assisted transport mechanism. As λ_x is increased further however, the oscillation frequency drops off rapidly. The dimer relaxation rate Γ_r is seen to increase slightly for increasing λ_x, representing the inverse timescale for the dimer relaxation to its ground state.

5.5.1 DCSB model for the FMO system with optical phonons

In this section I apply the DCSB model with an optical phonon bath to the FMO complex. It was determined in Section 2.3.4, for certain peaks selected from FMO spectral data, that the corresponding optical phonon dimensionless coupling parameter was small enough to permit a perturbative calculation of the system-bath interaction. This was done in Section 3.3. Here I use various optical phonon peaks at 6,8 and 10 meV, with

linewidth 0.5meV, and spectral weight 15meV to investigate the non-perturbative effect of optical phonons on the FMO system. This optical phonon frequency falls within the bandwidth of the FMO dimer and is expected to greatly affect the dynamics. This is in contrast to the perturbative results for very large optical phonon frequency relative to FMO dimer parameters.

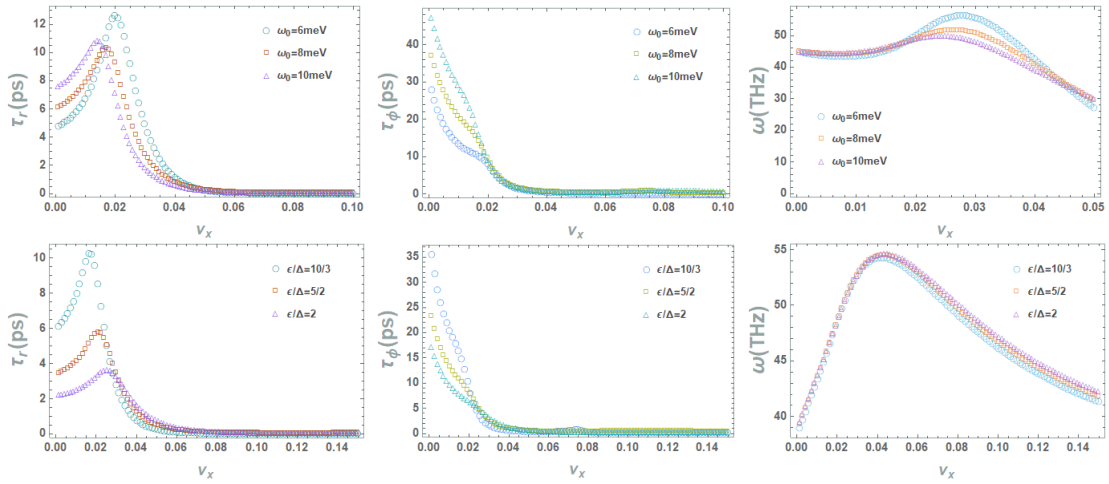

Figure 5.4: Exciton transfer time τ_r (blue line), coherence time τ_ϕ (orange line), and dimer oscillation frequency ω (purple line) as a function of non-diagonal coupling strength ν_x. Parameters: $\epsilon = 20$meV, $\Delta = 6$meV, ζ_z=1, $k_BT = 27$meV, $\omega_0 = 6$meV. Bath spectral density of Gaussian-optical form: $J_{(x,z)}(\omega) = \lambda_{(x,z)}\exp(-(\omega - \omega_0)^2/2\xi^2)$.

In Figure 5.4 we see the effect of turning on the non-diagonal coupling on a dimer with FMO parameters. We see qualitatively similar results to the FMO system coupled to an acoustic phonon bath. The dimer oscillation frequency is once again seen to increase in accordance with the phonon-assisted transport mechanism and drop off for large enough values of the non-diagonal coupling energy. For small values of ν_x the exciton time is seen to increase, alongside a an increase in the dimer oscillation frequency. As the non-diagonal coupling energy is increased further, both the transfer time and coherence time, decrease rapidly as the additional coupling mechanism begins to decrease coherence effects and aid in transfer rate of the exciton through the dimer system. However, despite the additional decoherence observed with non-diagonal coupling, once again the coherence time remains persistently longer than the transfer. Therefore we can conclude that the exciton remains coherent for the duration of its motion.

5.5.2 Summary

In this chapter I have analysed a two-state central system coupled both diagonally and non-diagonally to an oscillator bath. I dubbed this model the Dual-coupling spin-boson (DCSB) model. I used both a super-Ohmic and optical spectral density for the bath, with the optical spectral density having a Gaussian form for the spectral broadening. The application of the DCSB model to photosynthesis was motivated in Chapters 2 and 3 by the presence of delocalised excitons across two chromophores in the FMO complex. Oscillator baths consisting of acoustic phonons motivated the use of a super-Ohmic spectral density and optical phonons motivated the Gaussian-optical spectral density.

For a super-Ohmic bath, the DCSB model found the exciton to remain in the coherent phase as the non-diagonal coupling was turned on and varied. The exciton transfer time through the dimer was found to decrease rapidly for larger non-diagonal couplings as did the exciton coherence. Oscillations were found to persist in the exciton dynamics for the range of non-diagonal coupling strengths, with the coherence time found to be longer than the exciton transfer time for the full range of non-diagonal couplings. Therefore the non-diagonal coupling was found to not only facilitate exciton transfer through the dimer system, but produce coherent exciton transfer for relatively large non-diagonal coupling strengths. Similar results were found for a Gaussian-optical spectral density. Both the exciton transfer time and coherence time were found to decrease rapidly for significant non-diagonal coupling strengths, with the coherence time again remaining longer than the transfer time.

Both of these results can be interpreted within the context of the inelastic-phonon-assisted tunnelling mechanism. By turning on the non-diagonal coupling to the bath, inelastic processes are introduced to the dynamics. Excitons can tunnel between chromophores by emission and absorption of phonons from the bath. This produces an increased density of final states available to the exciton, and therefore facilitates exciton tunnelling. As the coupling strength becomes large enough, the tunnelling becomes one-way as the exciton becomes heavily dressed with its phonon cloud.

Chapter 6

Summary, conclusions and future work

I now summarise the work presented in this thesis, and draw conclusions pertaining to the results of the 3-site-boson model, and the dual-coupling-spin-boson (DCSB) model. I also conclude the investigation of applying both models to the photosynthesis mechanism. Finally I suggest a number of avenues of further research.

In Chapter 3 I introduced some of the key aspects of the 3-site model isolated from any environment, as well as some of the limiting and perturbative treatments of the 3-site system interacting with a harmonic oscillator bath. First, I introduced the concept of population trapping in a 3-site-V configuration. I demonstrated that the addition of an arbitrarily strong decay mode out of the lower ground state still leads to a long-time population present in the dynamics. This 'trapping' effect can be attributed to the presence of an eigenstate, known as the 'dark state', that overlaps only with the upper two levels despite there being no tunnelling term between these levels in the 3-site-V configuration. I demonstrated how, by tuning the on-site energies of the upper two levels, this dark-state is accessed and contains no overlap with the decaying ground-state, leading to the long-time population trapping. To do this I established a path-integral formalism for the 'bare' 3-site system, not only to calculate the Greens functions for the bare system, but also to set up the analysis for subsequent chapters where I treat the system-bath coupling non-perturbatively. In the interest of exploring the 3-site system coupled to some environment, I first introduced a perturbative system-bath coupling to an external oscillator bath.

I then solved the 3-site-V system coupled perturbatively to a harmonic oscillator bath

for 3-different spectral densities: Ohmic, super-Ohmic and optical phonons. I applied the noninteracting-blip-approximation (NIBA) to truncate the number of coherent-bath interaction processes corresponding to higher-order coherence effects. The region of validity of this approximation was not just discussed qualitatively—in the introduction chapter—but quantified. The quantity F_1, describing the ratio of average time spent in an off-diagonal state to a diagonal state of the density matrix, was shown to be minimised in the perturbative regime provided the tunnelling energies were small compared to the on-site energies. With this condition met, NIBA was shown to be valid in this regime. My final results for this model involved calculations of the three frequencies present in the system and an exploration of the coherent-incoherent phase space. We saw that the system operates only in the coherent phase across the full temperature range (N.B. I don't vary the system-bath coupling parameter here as it represents a perturbative quantity in this model). I found that the relaxation time associated with the dark-state was the shortest of the three in both the Ohmic and super-Ohmic regime. Therefore, in the perturbative limit at least, I show that the dark-state is the most sensitive state in the system to the effects of the bath, and coherence effects attributed to this state are strongly suppressed. However, the opposite is found to be true for the case of an optical phonon bath for low-temperatures. Here, the dark-state dominates the relaxation times and therefore is the most robust state in terms of exhibiting long-time coherence effects. For mid-high temperatures the decay rates are shown to converge and the corresponding relaxation times in this limit are comparable.

In Chapter 4 I moved beyond the perturbative analysis of the 3-site-boson model, incorporating the effects of the bath to all orders in the system-bath coupling parameter. Building on the path integral formalism for the 3-site propagator set up in Chapter 3, I used an influence functional approach to model the system-bath interactions. NIBA was once again employed to simplify the number of coherent system-bath processes, however the influence functionals still required expansions in small parameters in order to obtain tractable pole structures for the propagators. Therefore I chose to inspect the high-temperature limit in the interest of modelling physiological temperatures $T = 300K$ in the FMO complex. This provided me once again with a cubic pole structure for the propagator, this time to all orders in the system-bath coupling parameter. Incidentally, for the case of Ohmic-bath spectral densities, I was unable to explore the low-temperature regime for three distinct frequencies, as the pole structure in this limit is an arbitrary order polynomial in the system-bath coupling parameter. The original 2-site spin-boson model was able to explore this limit by utilising the special function: the Mittag-Leffler

function [31, 61], however the 3-site problem remains intractable analytically. A numerical solution to the propagators pole structure is still permitted of course, but beyond the scope of this thesis. Nevertheless, the high-temperature regime was still accessible for the Ohmic case and it is in this regime that we see the coherent-incoherent phase transition. I was once again able to explore the phase space of the model by inspecting the discriminant of the cubic polynomial, and in a similar fashion to the original spin-boson model, we saw a phase transition beyond a critical value of the coupling parameter.

I also quantified the validity of NIBA in the non-perturbative regime with a calculation of F_1 for various areas of the parameter space. I demonstrated how for the Ohmic case, NIBA is primarily valid in the semi-classical regime of small tunnelling energy relative to on-site energy. The complicated dependence of F_1 on the system-bath coupling parameter as well as temperature required a graphical analysis. In general, we saw that NIBA is valid in the mid-high temperature regime as well as the strong coupling regime. This is intuitive as NIBA is a strong-decoherence approximation and one would expect this to apply in the case of strong system-bath coupling and/or high-temperature.

The primary results of the non-perturbative analysis are the relaxation times. In the Ohmic regime I calculated the three distinct frequencies coming from the cubic pole structure in the high-temperature limit. For the parameter space explored in this section: $\epsilon/\Delta \sim 10, k_B T \ll \omega_c, \gamma < 1$, I found the system to exhibit a persistent coherent phase. The frequency associated with the dark-state of the system was found to have the slowest decay rate, and correspondingly the longest relaxation time, especially for small to intermediate values of the coupling parameter. Therefore, it is this state in the system that dominates the long-time coherence in the system across the range $0 < \gamma < 1$.

The 3-site boson model, for an Ohmic bath spectral density, is ultimately applied to the FMO complex. For the FMO parameters determined for an effective 3-site system coupled to an Ohmic bath, I found relaxation times $\tau_D \sim 800$fs, $\tau_\pm \sim 100$fs at physiological temperatures. These results put the exciton transfer well within the incoherent regime, as the exciton coherence dies out faster than the time taken for the exciton to propagate through the system.

In Chapter 5 I formulated the dual-coupling spin-boson model (DCSB) and investigated the results in both a general parameter regime–in units of the bias energy ϵ, and for the FMO-complex parameters. This model describes a dimer system coupled both diagonally and non-diagonally to an oscillator bath, and I utilised an environment characterised by both super-Ohmic and optical phonon spectral densities. I once again used NIBA to evaluate the influence functionals, meaning that this model applies in the regime

of small tunnelling energy to on-site energy.

For the case of a super-Ohmic oscillator bath, I was able to explore results in the high temperature limit. We saw in this limit how the system remained in a persistent coherent phase as the dimensionless non-diagonal coupling parameter is varied. For small couplings the dimer oscillation frequency rapidly increases along with a slight reduction in the pure relaxation rate. The physical basis for this is due to the inelastic phonon-assisted transport mechanism, whereby the transfer rate between dimer states is increased due to the allowance of phonon emission/absorption processes. As the coupling is increased beyond a certain point, the oscillation frequency dies off as the particle's phonon cloud becomes heavier, making it harder for the particle to tunnel between wells. For the DCSB model with acoustic phonons applied to the FMO complex, similar effects were found. The exciton transfer time–the inverse of the pure relaxation rate–was found to increase slightly for small enough values of the non-diagonal coupling parameter as well. Correspondingly, the coherent relaxation time–the time associated with the relaxation of the oscillatory terms in the dynamics–was found to also increase for small non-diagonal couplings. However, as the non-diagonal coupling was increased further, both the transfer and coherence times of exciton were seen to rapidly decrease. This happens alongside a reduction in dimer oscillation frequency and can be interpreted within the context of phonon-assisted tunnelling. For small enough couplings the exciton is able to tunnel back and forth coherently between the two states in the system. This is due to an increased density of final states available to the exciton by way of phonon emission/absorption processes. However, as the coupling becomes sufficiently strong, the exciton is over 'dressed' by its phonon cloud and tunnelling becomes one-way.

The addition of non-diagonal system-bath coupling serves to not only increase the rate at which the exciton is transferred through the dimer but also introduce an additional decoherence mechanism. However, the coherence time remains longer than the exciton transfer within a certain range of non-diagonal couplings. Therefore, one can conclude that, provided the non-diagonal coupling strength is significant, the exciton remains coherent as it travels through the FMO dimer according to the DCSB model.

The DCSB model has successfully managed to produce both rapid and coherent exciton transfer in the FMO complex. Traditional models for FRET fail to reproduce these effects, which suggests the inclusion of non-diagonal couplings is crucial to the exciton transfer mechanism in the FMO complex. Förster theory can produce rapid exciton transfer times but excludes any possibility of coherence. In the opposite limit, Redfield theory fails to produce the rapid exciton transfer times observed in the FMO complex. Fur-

thermore, in both cases, the model parameters do not accurately reflect the real physical systems they model. Neither the assumption of perturbative tunnelling energy relative to system-bath coupling in Förster theory, nor the Markov approximation and perturbative system-bath coupling assumed in Redfield theory are valid. A non-perturbative theory, in any of these parameters, falls within the purview of the spin-boson model. When applied to the FMO complex, the spin-boson model predicts incoherent exciton transfer for Ohmic spectral densities, and coherent but slow exciton transfer for super-Ohmic baths. Therefore one can conclude that the inclusion of non-diagonal couplings is crucial to the maintenance of rapid and coherent exciton transfer in the FMO complex with a super-Ohmic bath.

Motivated by the evidence of structured spectral densities in the FMO complex, I also investigated the DCSB model for an optical phonon bath. A Gaussian lineshape was used to model the optical phonon peaks, and the bath correlators were evaluated using the saddle-point approximation. This technique is valid for spectral lineshapes with very small width which is indeed the case for the FMO complex. We saw in Section 2.3.4, that experimentally determined spectra for the FMO complex found optical phonon peaks at relatively high frequencies with small linewidths. Therefore the saddle-point approximation was justified in this case. I also demonstrated in Section 2.3.4, how the dimensionless coupling parameters pertaining to the dominant peaks in the FMO spectra were very small. This permitted a perturbative approach to modelling the system-bath couplings. In the interest of investigating the non-perturbative effects of optical phonons on the FMO system, a fictitious peak with frequency within the bandwidth of the FMO parameters was chosen for the DCSB model. The strong coupling to this optical phonon peak is hoped to reflect the overall coupling of the FMO system to the many weak optical phonon vibrations.

The results of the DCSB model with an optical phonon bath were similar to the acoustic phonon (super-Ohmic) results. The dimer oscillation frequency increased for small enough values of the non-diagonal system-bath coupling energy, and the coherence time remained longer than the pure relaxation time for the range of couplings. Once again, while both the exciton transfer time and coherence time were greatly reduced for significant non-diagonal couplines, the coherence time remained persistently longer. Therefore the optical phonon bath also aids in exciton transfer through the dimer in a similarly efficacious way to the acoustic phonon bath, while the exciton remains coherent for the duration of its motion.

It is prudent to ask the question at this point: what is the functionality of coherence

in the FMO exciton transfer mechanism? The experimental evidence for coherence in the system is clear, and the success of the DCSB model here has demonstrated the importance of including non-diagonal couplings in the modelling of exciton transfer. However, what do these results say about the functionality of coherence in the system? Coherent (delocalised) excitons are characterised by overlapping exciton wavefunctions on nearby chromophores. The resulting exciton dynamics behaves in a wave-like manner, and associated with this will be the oscillatory 'quantum beating' signals observed in experiment. When there exists significant wavefunction overlap between chromophores, non-diagonal couplings should be present. The DCSB model has demonstrated that significant non-diagonal couplings promotes exciton transfer through the dimer system in accordance with the experimentally observed values. While the presence of non-diagonal couplings serves to introduce an additional decoherence mechanism, the coherence time of exciton remains longer than the exciton transfer time. This is perhaps unsurprising, since the presence of non-diagonal couplings is predicated on the coherent nature of excitons in the first place. Therefore, the functionality of coherence in photosynthesis, if any, could be to introduce non-diagonal system-bath couplings between chromophores. This facilitates the inelastic phonon-assisted transport mechanism and provides the exciton with additional tunnelling pathways between chromophores.

6.1 Further Work

I now discuss a number of avenues of further research that could build on the work presented in this thesis. Neither the 3-site boson model presented in this thesis nor the DCSB model are exactly solvable due to the complicated nature of the system-bath coupling. The noninteracting-blip approximation (NIBA) employed here is a first step along the way of treating the system-bath interaction processes in a non-perturbative coupling approach. A number of analytic studies have been done that go beyond NIBA. These take the form of summing a larger class of diagrams, including higher order system-bath processes. The nearest-neighbour blip-approximation (NNBA) for example includes consecutive blip-blip interaction terms, permitting the system to spend more time in the off-diagonal state of the density matrix and therefore incorporate longer-lived coherence effects. This would allow one to consider stronger tunnelling matrix elements with respect to the on-site energies in both the 3-site and 2-site models. This is because the system is permitted to spend more time in off-diagonal states of the density matrix. This preserves longer coherence effects and one would expect to see an increase in relaxation

times calculated for these systems. For the FMO complex, there are a number of three- and two-site molecular configurations that contain a larger ratio of Δ/ϵ than considered in this work. Modelling these molecular configurations would require a model that goes beyond NIBA, and NNBA could be a candidate for this. Of course, as one considers increasingly higher order diagrams in this regard, the analytical complexity of the model greatly increases. However for the 2-site spin-boson model this has nevertheless been shown to remain a tractable analytical problem yielding illuminating results [27, 99].

For the 3-site boson model it remains unclear whether such a relaxed approximation (NNBA) can be applied successfully analytically. The problem one faces in the 3-dimensional Hilbert space of the model is substantially harder than that for the 2-D Hilbert space of the 2-site model. Excursions into the off-diagonal elements of the 3-by-3 density matrix need to take into account all possible consecutive blip-blip and blip-sojourn interactions which make up the space of the 3-by-3 density matrix. Since the system is permitted to spend additional time in the off-diagonal space of the density matrix, the combinatorics problem grows substantially. Nevertheless, the solution to this problem would be a valuable one not just in the interest of relaxation NIBA and observing the additional coherence effects in the model but also because it would allow the system to occupy the coherent state in the system that overlaps with both the upper two levels. This possibility was excluded in our model because of the application of NIBA which quenches the off-diagonal excursions too rapidly before they can enter into this fragile coherent state.

One of the famous applications of the spin-boson model was to the Kondo problem. It was shown that the peculiar singular behaviour of charged interstitials in conducting metals could be explained by the high density of electron-hole excitations around the Fermi surface. This leads to a self-trapping phase transition at zero temperature above a critical value of the coupling strength, as well as an anomalous temperature dependence on diffusion. The spin-boson model was appropriate in this case because the impurities can be represented by a spin-1/2 central system, and the surrounding Fermi gas can be characterised by electron-hole excitations around the Fermi surface at such low temperatures. These electron-hole pairs are bosonic in character and obey an Ohmic form for the spectral density. Therefore, in the context of this research, one could ask the question: how does the Kondo effect change when the impurity is actually a 3-level system such as the one studied in this system? As discussed in this thesis, the 3-level system contains intrinsic properties such as population trapping that are very different to a 2-level system. This could have dramatic effects on the Kondo effect when applied to metals.

The 3-level model coupled to an Ohmic oscillator bath would need to be explored in the zero temperature regime, as only the high-T regime was considered in this thesis. One would also need to inspect certain response functions such as the magnetic susceptibility in order to answer specific questions relating to the Kondo effect.

Finally I would like to comment on the implications of these findings with respect to the development of artificial light-harvesting systems. Research into photosynthesis is motivated not only by our general interest in a complete understanding of the biophysics but also by the potential applications to our own light-capturing technologies. Nature has had millions of years to optimise these processes, and reverse engineering the energy transfer mechanism in photosynthesis could help us make our own artificial light harvesting technologies more efficient. If we are to achieve higher efficiencies in light-capturing technologies, it is possible that this can be achieved by promoting inelastic phonon-assisted tunnelling processes in the exciton transport schemes of these devices. This would mean reducing the inter-molecular spacing as much as possible, as this would facilitate greater exciton wavefunction overlap between molecules, and therefore augmented phonon-assisted tunnelling. We have learned from photosynthesis, that even in hot and messy molecular environments, exciton transfer can be very efficient, provided the inter-molecular distances are kept sufficiently small. In this case, quantum effects are allowed to persist in otherwise non-ideal environments.

Bibliography

[1] D. P. DiVincenzo, D. Loss. Quantum computers and quantum coherence. *Journal of Magnetism and Magnetic Materials*, 200(202-218), 1999.

[2] D. A. Ryndyk. *Theory of Quantum Transport at Nanoscale*. Springer, 2016.

[3] Hwang, H and Rossky, P. Electronic decoherence induced by intramolecular vibrational motions in a betaine dye molecule. *J. Phys. Chem. B*, 108(6723–6732), 2004.

[4] Franco, I; Shapiro, M; Brumer, P. Femtosecond dynamics and laser control of charge transport in trans-polyacetylene. *The Journal of Chemical Physics*, 128(244905), 2008.

[5] Gregory S. Engel, Tessa R. Calhoun, Elizabeth L. Read, Tae-Kyu Ahn, Tomas Mancal, Yuan-Chung Cheng, Robert E. Blankenship, and Graham R. Fleming. Evidence for wavelike energy transfer through quantum coherence in photosynthetic systems. *Nature*, 446(7137):782–786, April 2007.

[6] H. Lee, Y. C. Cheng, and G. R. Fleming. Coherence dynamics in photosynthesis: Protein protection of excitonic coherence. *Science*, 316(1462), 2007.

[7] Panitchayangkoon, G et al. Long-lived quantum coherence in photosynthetic complexes at physiological temperature. *PNAS*, 107(12766–12770), 2010.

[8] Collini, E et al. Coherently wired light-harvesting in photosynthetic marine algae at ambient temperature. *Nature*, 463(644), 2010.

[9] Fassioli, F et. al. Photosynthetic light harvesting: excitons and coherence. *J. R. Soc. Interface*, 11(20130901), 2014.

[10] Roseanne J. Sension. Biophysics: Quantum path to photosynthesis. *Nature*, 446(7137):740–741, April 2007.

[11] I. Burghardt, V. May, D. A. Micha, and E. R. Bittner, editors. *Energy Transfer Dynamics in Biomaterial Systems*. Springer Series in Chemical Physics 93, 2009.

[12] R. E. Blankenship. *Molecular Mechanisms of Photosynthesis*. Blackwell Science, London, 2002.

[13] X. Hu and K. Schulten. How nature harvests sunlight. *Physics Today*, 50(28), 1997.

[14] C. Curutchet and B. Mennucci. Quantum chemical studies of light harvesting. *Chemical Reviews*, 117(294-343), 2016.

[15] M. B. Plenio and S. F. Huelga. Dephasing-assisted transport: quantum networks and biomolecules. *New J. Phys.*, 10(11):113019, November 2008.

[16] F. Caruso, A. W. Chin, A. Datta, S. F. Huelga, and M. B. Plenio. Highly efficient energy excitation transfer in light-harvesting complexes: The fundamental role of noise-assisted transport. *J. Chem. Phys.*, 131(10):105106, September 2009.

[17] A. W. Chin, A. Datta, F. Caruso, S. F. Huelga, and M. B. Plenio. Noise-assisted energy transfer in quantum networks and light-harvesting complexes. *New J. Phys.*, 12(6):065002, June 2010.

[18] A.W. Chin et al. The role of non-equilibrium vibrational structures in electronic coherence and recoherence in pigment–protein complexes. *Nature Physics*, 9, 2013.

[19] J. Lim et al. Phonon-induced dynamic resonance energy transfer. *New Journal of Physics*, 16, 2014.

[20] J. Cao and R.J. Silbey. Optimization of exciton trapping in energy transfer processes. *The Journal of Physical Chemistry A*, 113(50), 2009.

[21] Ishizaki, A; Fleming, G.R. Unified treatment of quantum coherent and incoherent hopping dynamics in electronic energy transfer: Reduced hierarchy equation approach. *THE JOURNAL OF CHEMICAL PHYSICS*, 130(234111), 2009.

[22] A. Kolli et al. The fundamental role of quantized vibrations in coherent light harvesting by cryptophyte algae. *The Journal of Chemical Physics*, 137(174109), 2012.

[23] Alexandra Olaya-Castro, Chiu Fan Lee, Francesca Fassioli Olsen, and Neil F. Johnson. Efficiency of energy transfer in a light-harvesting system under quantum coherence. *Phys. Rev. B*, 78(8):085115, August 2008.

[24] Ishizaki, A; Fleming, G.R. On the adequacy of the redfield equation and related approaches to the study of quantum dynamics in electronic energy transfer. *J. Chem. Phys*, 130(234110), 2009.

[25] Sharp, L.Z; Egorova, D; Domcke, W. Efficient and accurate simulations of two-dimensional electronic photonecho signals: Illustration for a simple model of the fenna–matthews–olson complex. *J. Chem. Phys*, 132(014501), 2009.

[26] P. Nalbach, D. Braun and M. Thorwart. Exciton transfer dynamics and quantumness of energy transfer in the fenna-matthews-olson complex. *Phys. Rev. E*, 84(041926), 2011.

[27] Leonardo A. Pachón and Paul Brumer. The physical basis for long-lived electronic coherence in photosynthetic light harvesting systems. *J. Phys. Chem. Lett.*, 2(21), 2011.

[28] V.J Emery, A. Luther. Low-temperature properties of the kondo hamiltonian. *Phys. Rev. B*, 9(1), 1974.

[29] Caldeira, A & Leggett, A. Influence of dissipation on quantum tunneling in macroscopic systems. *PRL*, 46(4), 1981.

[30] Caldeira, A & Leggett, A. Quantum tunnelling in a dissipative system. *Annals of Physics*, 149(374-456), 1983.

[31] Leggett, A.J., Chakravarty, S. et al. Dynamics of the dissipative two-state system. *Rev. Mod. Phys.*, 59(1), 1987.

[32] Chakravarty, S; Leggett, A. Dynamics of the two-state system with ohmic dissipation. *PRL*, 52(1), 1984.

[33] Dekker, H. Noninteracting-blip approximation for a two-level system coupled to a heat bath. *PRA*, 35(3), 1987.

[34] Weiss, U. Influence of friction and temperature on coherent quantum tunneling. *Journal of Low Temperature Physics*, 68(3/4), 1987.

[35] Grabert, H; Weiss, U. Quantum tunneling rates for asymmetric double-well systems with ohmic dissipation. *PRL*, 54(15), 1985.

[36] Fisher, M.P.A. and Dorsey, A.T. Dissipative quantum tunneling in a biased double-well system at finite temperatures. *Physical Review Letters*, 54(15), 1985.

[37] Feynman, R.P.; Vernon, F.L. The theory of a general quantum system interacting with a linear dissipative system. *Annals of Physics*, 24(118-173), 1963.

[38] Fisher, M.P.A and Zwerger, W. Quantum brownian motion in a periodic potential. *Phys. Rev. B*, 32(10), 1985.

[39] Wilhelm, F.K.; Kleff, S; von Delft, J. The spin-boson model with a structured environment: a comparison of approaches. *Chemical Physics*, 296(345-353), 2004.

[40] Grabert, H. Dissipative quantum tunneling of two-state systems in metals. *PRB*, 46(19), 1992.

[41] Joel Gilmore, Ross H. McKenzie. Spin boson models for quantum decoherence of electronic excitations of biomolecules and quantum dots in a solvent. *J. Phys.: Condens. Matter*, 17(1735), 2005.

[42] Joel Gilmore, Ross H. McKenzie. Criteria for quantum coherent transfer of excitons between chromophores in a polar solvent. *arXiv:quant-ph/0412170*, 2006.

[43] Gilmore, J and McKenzie, R. Quantum dynamics of electronic excitations in biomolecular chromophores: Role of the protein environment and solvent. *J. Phys. Chem. A*, 112(2162-2176), 2008.

[44] Jeremy Moix et al. Efficient energy transfer in light-harvesting systems, iii: The influence of the eighth bacteriochlorophyll on the dynamics and efficiency in fmo. *J. Phys. Chem. Lett.*, 2(3045–3052), 2011.

[45] Hui Dong, Da-Zhi Xu, Jin-Feng Huang, and Chang-Pu Sun. Coherent excitation transfer via the dark-state channel in a bionic system. *Light Sci. Appl.*, 1(3):e2, March 2012.

[46] Julia Adolphs and Thomas Renger. How proteins trigger excitation energy transfer in the FMO complex of green sulfur bacteria. *Biophys. J.*, 91(8):2778–2797, 2006.

[47] T. Holstein. Studies of polaron motion: Part 2. the 'small' polaron. *Ann. Phys.*, 8(343), 1959.

[48] R. Peierls. *Quantum Theory of Solids*. Clarendon Press, Oxford, 1955.

[49] W. P. Su, J. R. Schrieffer, and A. J. Heeger. Solitons in polyacetylene. *Phys. Rev. Lett.*, 42(1698), 1979.

[50] D.J. J. Marchand, P.C. E. Stamp, and M.Berciu. Dual coupling effective band model for polarons. *Phys. Rev. B*, 95(035117), 2017.

[51] G. H. Richards, K. E. Wilk, P. M. G. Curmi, H. M. Quiney, and J. A.Davis. Excited state coherent dynamics in light-harvesting complexes from photosynthetic marine algae. *J. Phys. B: At. Mol. Opt. Phys.*, 45(154015), 2012.

[52] G.D. Mahan. *Many particle physics, 2nd ed.* Plenum Press, 1990.

[53] N. Wu, K. Sun, Z. Chang, and Y. Zhao. Resonant energy transfer assisted by off-diagonal coupling. *J. Chem. Phys.*, 136(124513), 2012.

[54] A. Nazir. Correlation-dependent coherent to incoherent transitions in resonant energy transfer dynamics. *Phys. Rev. Lett.*, 102(146404), 2009.

[55] Y. Yao, N, Zhou, J, Prior, Y, Zhao. Competition between diagonal and off-diagonal coupling gives rise to charge-transfer states in polymeric solar cells. *Nature Scientific Reports*, 5(14555), 2015.

[56] V. Coropceanu et. al. Charge transport in organic semiconductors. *Chem. Rev.*, 107(926-952), 2007.

[57] S.M. Falke, et al. Coherent ultrafast charge transfer in an organic photovoltaic blend. *Science*, 344(1001), 2014.

[58] Wang, T. and Chan, W.-L. Dynamical localization limiting the coherent transport range of excitons in organic crystals. *J. Phys. Chem. Lett.*, 5(1812C1818), 2014.

[59] G. Scholes et. al. Using coherence to enhance function in chemical and biophysical systems. *Nature*, 543(647), 2017.

[60] A. Würger. Strong-coupling theory for the spin-phonon model. *Phys. Rev. B.*, 57(1), 1998.

[61] U Weiss. *Quantum Dissipative Sytems.* World Scientific, 2008.

[62] Tobias Brixner, Jens Stenger, Harsha M. Vaswani, Minhaeng Cho, Robert E. Blankenship, and Graham R. Fleming. Two-dimensional spectroscopy of electronic couplings in photosynthesis. *Nature*, 434(7033):625–628, March 2005.

[63] D. Karcz et al. Lessons from chlorophylls: Modifications of porphyrinoids towards optimized solar energy conversion. *Molecules*, 19(15938-15954), 2014.

[64] V. May and O. Kuhn, editors. *Charge and Energy Transfer Dynamics in Molecular Systems.* Wiley, 2004.

[65] A.S. Davydov. The theory of molecular excitons. *Soviet Physics Uspekhi*, 7(2), 1964.

[66] G.D. Scholes. Long-range resonance energy transfer in molecular systems. *Annu. Rev. Phys. Chem.*, 54(57), 2012.

[67] V. Helms, editor. *Principles of Computational Cell Biology.* Wiley, 2008.

[68] Peterman, E.J, Dukker, F.M, van Grondelle, R, van Amerongen, H. Chlorophyll a and carotenoid triplet states in light-harvesting complex ii of higher plants. *Biophys. J.*, 69(2670-2678), 1995.

[69] B.W. Matthews, R.E. Fenna. Structure of a green bacteriochlorophyll protein. *Acc. Chem. Res.*, 13(9), 1980.

[70] Tronrud,D.E.;Wen,J.;Gay,L.;Blankenship,R.E. Thestructural basis for the difference in absorbance spectra for the fmo antenna protein from various green sulfur bacteria. *Photosynth. Res*, 100(79-87), 2009.

[71] A. Lohner et al. Fluorescence-excitation and emission spectroscopy on single fmo complexes. *Nature Scientific Reports*, 6(31875), 2016.

[72] D. Singh and S. Dasgupta. Coherence and its role in excitation energy transfer in fenna- matthews-olson complex. *J. Phys. Chem. B*, 121(1290-1294), 2017.

[73] M. Aghtar et al. The fmo complex in a glycerol-water mixture. *J. Phys. Chem. B*, 117(7157), 2013.

[74] Hayes, D. & Engel, G. S. Extracting the excitonic hamiltonian of the fenna-matthews-olson complex using three-dimensional third-order electronic spectroscopy. *Biophys. J.*, 100(2043–2052), 2011.

[75] C. Olbrich, T. L. C. Jansen, J. Liebers, M. Aghtar, J. Strümpfer, K. Schulten, J. Knoester, and U. Kleinekathöfer. From atomistic modeling to excitation transfer and two-dimensional spectra of the fmo light-harvesting complex. *J. Phys. Chem. B*, 115(8609), 2011.

[76] S. Shim, P. Rebentrost, S. Valleau, and A. Aspuru-Guzik. Atomistic study of the long-lived quantum coherences in the fenna-matthews-olson complex. *Biophys. J.*, 102(649), 2012.

[77] B. S. Prall, D. Y. Parkinson, G. R. Fleming, M. Yang, and N. Ishikawa. Two-dimensional optical spectroscopy: Two-color photon echoes of electronically coupled phthalocyanine dimers. *J. Chem. Phys.*, 120(2537), 2004.

[78] S. M. Vlaming, and R. J. Silbey. Correlated intermolecular coupling fluctuations in photosynthetic complexes. *J. Chem. Phys.*, 136(055102), 2012.

[79] D. J. J. Marchand, G. De Filippis, V. Cataudella, M. Berciu, N. Nagaosa, N. V. Prokofev, A. S. Mishchenko and P. C. E. Stamp. Sharp transition for single polarons in the one-dimensional su-schrieffer-heeger model. *Phys. Rev. Lett.*, 105(266605), 2017.

[80] B.W. Matthews, R.E. Fenna. Calculation of couplings and energy-transfer pathways between the pigments of lh2 by the ab initio transition density cube method. *J. Phys. Chem. B*, 102(5378-5386), 1998.

[81] Sharp, L.Z.; Egorova, D.; Domcke, W. . Efficient and accurate simulations of two-dimensional electronic photon-echo signals: Illustration for a simple model of the fenna–matthews–olson complex. *The Journal of Chemical Physics*, 132(014501), 2010.

[82] T. Forster. Delocalized excitation and excitation transfer. *Mordern Quantum Chemistry, Istanbul Lectures*, 3(93), 1965.

[83] H. Fukagawa, T. Shimizu, Y. Iwasaki . Operational lifetimes of organic light-emitting diodes dominated by förster resonance energy transfer. *Nature: Scientific Reports*, 7(1735), 2017.

[84] A. Ishizaki, et al. Quantum coherence and its interplay with protein environments in photosynthetic electronic energy transfer. *Phys. Chem. Chem. Phys.*, 12(7319–7337), 2010.

[85] A.G. Redfield. On the theory of relaxation processes. *IBM J. Res. Dev.*, 1(19), 1957.

[86] P. Lambropoulus and D. Petrosyan. *Fundamentals of Quantum Optics and Quantum Information*. Springer, 2007.

[87] H.P. Breuer and F. Petruccione. *THE THEORY OF OPEN QUANTUM SYSTEMS*. Oxford University Press, 2002.

[88] F. Petruccione H. Breuer. *The Theory of Open Quantum Systems*. Oxford University Press, 2007.

[89] H.B. Chen et al. Using non-markovian measures to evaluate quantum master equations for photosynthesis. *Nature Scientific Reports*, 5(12753), 2015.

[90] M. Schmidt et al. The eighth bacteriochlorophyll completes the excitation energy funnel in the fmo protein. *J. Phys. Chem. Lett.*, 2(93-98), 2011.

[91] Thyrhaug, E; et al. Exciton structure and energy transfer in the fenna-matthews-olson complex. *J. Phys. Chem. Lett.*, 7(1653-1660), 2016.

[92] K. Saito, T. Suzuki, H. Ishikita. Absorption-energy calculations of chlorophyll a and b with an explicit solvent model. *Journal of Photochemistry and Photobiology A: Chemistry*, 358(422-431), 2017.

[93] Leggett, A.J. Percolation, localization and supercon- ductivity. *NATO ASI Series B: Physics*, 109(p.1), 1984.

[94] Y. Cheng and G. R. Fleming. Dynamics of light harvesting in photosynthesis. *Annu. Rev. Phys. Chem.*, 60(241), 2009.

[95] G. D. Scholes and G. R. Fleming. Energy transfer and photosynthetic light harvesting. *Adventures in Chemical Physics: A Special Volume in Advances in Chemical Physics*, 132(57), 2006.

[96] Guinea, F. Friction and particle-hole pairs. *PRL.*, 53(13), 1984.

[97] Hänngi, P. and Ingold, G.L. Fundamental aspects of quantum brownian motion. *Chaos*, 15(026105), 2005.

[98] Jang, S.J. and Mennucci, B. Delocalized excitons in natural light harvesting complexes. *Rev. Mod. Phys.*, 90(035003), 2018.

[99] P. Esquinazi, editor. *Tunneling Systems in Amorphous and Crystalline Solids*. Springer, 1998.

[100] S. Hunklinger. Phonons in amorphous solids. *Journal de Physique*, 12(c9-461), 1982.

[101] M. F. Thorpe. *Phonons in Amorphous Solids*. Springer, 1976.

[102] M. Aghtar et al. Different types of vibrations interacting with electronic excitations in phycoerythrin 545 and fenna-matthews-olson antenna systems. *J. Phys. Chem. Lett.*, 5(3131), 2014.

[103] Cho,M et al. Exciton analysis in 2d electronic spectroscopy. *J. Phys. Chem. B*, 109(10542-10556), 2005.

[104] B. Li et al. The brownian oscillator model for solvation effects in spontaneous light emission and their relationship to electron trans fer. *J. Am. Chem. SOC*, 116(11039-11047), 1994.

[105] E.T.J. Nibbering, D.A. Wiersma, K.Duppen . Ultrafast electronic fluctuation and solvation in liquids. *Chemical Physics*, 183(167-185), 1994.

[106] L. Onsager. Electric moments of molecules in liquids. *J. Am. Chem. Soc.*, 58(1486), 1936.

[107] J. Tomasi and M. Persico. Molecular interactions in solution: An overview of methods based on continuous distributions of the solvent. *Chem. Rev.*, 94(2027), 1994.

[108] J. Newman and K.E. Thomas-Alyea. *Electrochemical systems*. Wiley, 2004.

[109] V.I. Novoderezhkin et al. Excitation dynamics in the lhcii complex of higher plants: Modeling based on the 2.72 åcrystal structure. *J. Phys. Chem. B*, 109(10493-10504), 2005.

[110] E. Read et al. Visualization of excitonic structure in the fenna-matthews-olson photosynthetic complex by polarization-dependent two-dimensional electronic spectroscopy. *Biophysical Journal*, 95(847–856), 2008.

[111] D. Zigmantas et al. Two-dimensional electronic spectroscopy of the b800–b820 light-harvesting complex. . *Proc. Natl. Acad. Sci. USA*, 103(12672–12677), 2006.

[112] T. Renger and R. A. Marcus. On the relation of protein dynamics and exciton relaxation in pigment–protein complexes: An estimation of the spectral density and a theory for the calculation of optical spectra. *J. Chem. Phys.*, 116(22), 2002.

[113] S.Jang, Y.C. Cheng, D.R. Reichman, and J.D. Eaves. Theory of coherent resonance energy transfer. *J. Chem. Phys.*, 129(101104), 2008.

[114] Olbrich, C et al. Theory and simulation of the environmental effects on fmo electronic transitions. *J. Phys. Chem. Lett.*, 2(, 1771–1776), 2011.

[115] Damjanovic, A; Kosztin, I; Schulten, K. Excitons in a photosynthetic light-harvesting system: A combined molecular dynamics/quantum chemistry and polaron model study. *Physical Review E*, 65(031919), 2002.

[116] Feynman, R.P. Space-time approach to non-relativistic quantum me- chanics. *Rev. Mod. Phys.*, 20(367-387), 1948.

[117] A. Atland and B. Simons. *Condensed Matter Field Theory*. Cambridge University Press, 2010.

[118] A. Devaquet. Avoided crossings in photochemistry. *Pure and applied chemistry*, 41(455), 1975.

[119] P. M. Radmore and P. L. Knight. Population trapping and dispersion in a three-level system. *J. Phys. B: At. Mol. Phys.*, 15(4):561, February 1982.

[120] Radmore, P.M; Knight, P.L. Population trapping and dispersion in a three-level system. *J. Phys. B*, 15(561-573), 1982.

[121] E.N. Economou. *Green's Functions in Quantum Physics*. Springer, 2006.

[122] Wurger, A. Dissipative tunneling in insulators: Noninteracting blip approximation and beyond. *Physical Review Letters*, 9(0031-9007), 1997.

[123] Riccardi, M. Solution of cubic and quartic equations. *Formalized Mathematics*, 17(2), 2009.

[124] Holmes, G.C. The use of hyperbolic cosines in solving cubic polynomials. *The Mathematical Gazette*, 86(507), 2002.

[125] Nickalls, R.W.D. A new approach to solving the cubic: Cardan's solution revealed. *The Mathematical Gazette*, 77(480), 1993.

[126] I.M. Gradshteyn, I.S. & Ryzhik. *Table of Integrals, Series, and Products*. Elsevier, 7th ed, 2007.

[127] Davis, P.J. Leonard euler's integral: A historical profile of the gamma function. *The American Mathematical Monthly*, 66(849-869), 1959.

[128] L. Kleinman. Theory of phonon-assisted tunneling in semiconductors. *Phys. Rev.*, 140(A637), 1965.

[129] W. P. Su, J. R. Schrieffer, and A. J. Heeger. Solitons in polyacetylene. *Phys. Rev. Lett.*, 42(1698), 1979.

[130] R. Silbey, R.W. Munn. General theory of electronic transport in molecular crystals. i. local linear electron–phonon coupling. *The Journal of Chemical Physics*, 72(2763), 1980.

[131] R.W. Munn, R. Silbey. Theory of electronic transport in molecular crystals. ii. zeroth order states incorporating nonlocal linear electron–phonon coupling. *The Journal of Chemical Physics*, 83(1843), 1985.

[132] R.W. Munn, R. Silbey. Theory of electronic transport in molecular crystals. iii. diffusion coefficient incorporating nonlocal linear electron–phonon coupling. *The Journal of Chemical Physics*, 83(1854), 1985.

[133] D. Chen, J. Ye, H. Zhang, Y. Zhao. On the munn-silbey approach to polaron transport with off-diagonal coupling and temperature-dependent canonical transformations. *J. Phys. Chem. B*, 115(5312), 2011.

[134] Z. Huang, et al. Polaron dynamics with off-diagonal coupling: beyond the ehrenfest approximation. *Phys. Chem. Chem. Phys*, 19(1655), 2017.

[135] M. Abramowitz and I.A. Stegun. *Handbook of Mathematical Functions.* Dover Publications, 1972.

[136] J. Matthews and R.L Walker, editors. *Mathematical Methods of Physics (2nd Edition).* Addison-Wesley, 1971.

Appendix A

Calculation of the electron-phonon correlation function for DCSB model

Here I present the calculation of the electron-phonon correlation function used to describe the effects of the phonon bath on a central system. In section chapter 5 I required a calculation of the electron-phonon correlation function $\langle B_+^x(t)B_-^z(t)\rangle$, which involves a correlation between phonon displacement operators pertaining to both diagonal and non-diagonal couplings. While following a derivation in Mahan [52] in evaluating these correlation functions, I present the specifics of my deviations rather than simply quoting the results, as I must be careful to distinguish between the diagonal and non-diagonal couplings λ_x and λ_z respectively. In the traditional literature, the electron correlation function calculation usually assumes just diagonal couplings present in the system therefore I must present the more general derivation case here. Starting from the calculation of the trace over the phonon distributions

$$\begin{aligned} F_{xz}(t) &= \left\langle B_+^x(t)B_-^z(0)\right\rangle_B \\ &= e^{\beta\Omega_{ph}}\mathrm{Tr}\left[e^{-\beta\sum_q \omega_q n_q}B_+^x(t)B_-^z(0)\right] \end{aligned} \tag{A.1}$$

Averaging each phonon state independently

$$F_{xz}(t) = \prod_q f_q^{xz}(t)$$

$$f_q^{xz}(t) = e^{\beta\Omega_{ph}} \sum_{n_q=0}^{\infty} e^{-\beta n_q \omega_q} \left\langle n_q \right| e^{-\lambda_q^x (b_q^\dagger e^{i\omega_q t} - b_q e^{-i\omega_q t})} e^{\lambda_q^z (b_q^\dagger - b_q)} \left| n_q \right\rangle \tag{A.2}$$

where

$$e^{\beta\Omega_q} = \left(\sum_{n_q=0}^{\infty} e^{-\beta n_q \omega_q} \right)^{-1} = 1 - e^{-\beta\omega_q} \tag{A.3}$$

is a normalisation prefactor. For brevity we drop the phonon wavevector subscript q for the time being.

$$f_{xz}(t) = (1 - e^{-\beta\omega}) \sum_{n=0}^{\infty} e^{-\beta n\omega} \left\langle n \right|^{-\lambda^x (b^\dagger e^{i\omega t} - b e^{-i\omega t})} e^{\lambda^z (b^\dagger - b)} \left| n \right\rangle \tag{A.4}$$

The state of n bosonic excitations is given by

$$\left| n \right\rangle = \frac{(b^\dagger)^n}{\sqrt{n!}} \left| 0 \right\rangle \tag{A.5}$$

Performing the Feynman-disentangling of operators [52] and applying the BCH formula $e^{A+B} = e^A e^B e^{-(1/2)[A,B]}$ we find

$$B_+^x(t) B_-^z(0) = e^{-\lambda_x^2/2 - \lambda_z^2/2} \exp\left(-\lambda_x b^\dagger e^{i\omega t} + \lambda_x b e^{-i\omega t} + \lambda_z b^\dagger - \lambda_z b \right) \tag{A.6}$$

In the interest of getting all the destruction operators on the right hand side and the creation operators on the left, the center two operators need to be exchanged

$$e^{\lambda_x b(t)} e^{\lambda_z b^\dagger} = e^{\lambda_z b^\dagger} \left[e^{-\lambda_z b^\dagger} e^{\lambda_x b^\dagger(t)} e^{\lambda_z b^\dagger} \right] \tag{A.7}$$

Applying the BCH formula to evaluate the expression

$$e^{-\lambda_z b^\dagger} b e^{\lambda_z b^\dagger} = b + \lambda_z \tag{A.8}$$

allows us to express

$$e^{\lambda_x b(t)} e^{\lambda_z b^\dagger} = e^{\lambda_z b^\dagger} \exp\left[\lambda_x e^{-i\omega t} (b + \lambda_z) \right] = e^{\lambda_z b^\dagger} e^{\lambda_x \lambda_z e^{-i\omega t}} e^{\lambda_x b(t)} \tag{A.9}$$

So this leaves us for the electron-phonon correlation function for each wavevector q

$$\begin{aligned} f_{xz}(t) =&(1-e^{-\beta\omega})\exp\left(-\frac{\lambda_x^2}{2}-\frac{\lambda_z^2}{2}+\lambda_x\lambda_z e^{-i\omega t}\right) \\ &\times\sum_{n=0}^{\infty}e^{-\beta\omega n}\exp\langle n|\left[(\lambda_z-\lambda_x e^{i\omega t})b^\dagger-(\lambda_z-\lambda_x e^{-i\omega t})b\right]|n\rangle \end{aligned} \tag{A.10}$$

defining $u=\lambda_z-\lambda_x e^{i\omega t}$, we can expand in a power series

$$e^{-ua}|n\rangle=\sum_{l=0}^{\infty}\frac{(-u)^l}{l!}a^l|n\rangle \tag{A.11}$$

Using the properties of the boson annihilation operators acting on the harmonic oscillator states gives us

$$e^{-ua}|n\rangle=\sum_{l=0}^{n}\frac{(-u)^l}{l!}\left[\frac{n!}{(n-l)!}\right]^{1/2}|n-l\rangle \tag{A.12}$$

Using the orthogonality of harmonic oscillator states and identifying the Laguerre polynomial of order n

$$\langle n|\,e^{-u^*a^\dagger}e^{-ua}|n\rangle=L_n(|u|^2) \tag{A.13}$$

Performing the summation over boson states by identifying the generating function of Laguerre polynomials [52]

$$(1-z)\sum_{n=0}^{\infty}L_n(|u|^2)z^n=e^{|u|^2z/(z-1)} \tag{A.14}$$

where $z=e^{-\beta\omega}$ and $-z/(z-1)=N=1/(e^{\beta\omega}-1)$. This leaves us with

$$f_{xz}^q(t)=\exp\left(-\lambda_x^2(1+N_q)/2-\lambda_z^2(1+N_q)/2\right)\exp\left(\lambda_x\lambda_z(1+N_q)e^{-i\omega t}+\lambda_x\lambda_z e^{i\omega t}N_q\right) \tag{A.15}$$

Therefore the full electron-phonon correlation function is the product over phonon states

$$
\begin{aligned}
F_{xz}(t) &= \prod_q f_{xz}^q(t) \\
&= \prod_q \exp\left(-u_x^2(1+N_q)/2 - u_z^2(1+N_q)/2\right) \exp\left(u_x u_z \left[e^{i\omega_q t} + N_q\left(e^{i\omega_q t} + e^{-i\omega_q t}\right)\right]\right)
\end{aligned}
\tag{A.16}
$$

which in its continuous form (see the next section B) is

$$
\begin{aligned}
F_{xz}(t) = \exp&\left(-\int_0^\infty \frac{d\omega}{2\omega^2}\big(J_x(\omega) + J_z(\omega)\big)\coth\left(\hbar\beta\omega/2\right)\right) \\
&\times \exp\left(\int_0^\infty d\omega \frac{\sqrt{J_x(\omega)J_z(\omega)}}{\omega^2}\Big(i\sin\omega t + \cos(\omega t)\coth\left(\hbar\beta\omega/2\right)\Big)\right)
\end{aligned}
\tag{A.17}
$$

which is the result we use in chapter 5.

Appendix B

Connection between continuous and discrete electron-phonon correlation function

In the text we use two different forms for the electron-phonon propagator and here make the link between the two. In the literature, the connection between the two is never made and usually the reader is expected to assume the jump between the discrete and continuous forms of the electron-phonon propagator. Here we start with the continuous form

$$\varphi(t) = \int_0^\infty d\omega \frac{J(\omega)}{\omega^2} \Big(i \sin \omega t - (1 - \cos \omega t) \coth \left(\hbar \beta \omega / 2 \right) \Big) \tag{B.1}$$

Inserting the general form of the spectral function

$$
\begin{aligned}
&2\int_0^\infty d\omega \sum_q \frac{\lambda^2}{\omega^2}\delta(\omega-\omega_q)\Big(i\sin\omega t-(1-\cos\omega t)\coth\hbar\beta\omega/2\Big)\\
&=\sum_q u_q^2\Big[e^{i\omega_q t}-e^{-i\omega_q t}+\Big(e^{i\omega_q t}+e^{-i\omega_q t}-1\Big)\coth\hbar\beta\omega_q/2\Big]\\
&=\sum_q u_q^2\Big[e^{i\omega_q t}-e^{-i\omega_q t}+\Big(e^{i\omega_q t}+e^{-i\omega_q t}-1\Big)(1+2n_q)\Big]\\
&=\sum_q u_q^2\Big[2e^{i\omega_q t}+2n_q\Big(e^{i\omega_q t}+e^{-i\omega_q t}\Big)-(1+2n_q)\Big]\\
&=\sum_q u_q^2\Big[n_q\Big(e^{i\omega_q t}-1\Big)+(1+n_q)\Big(e^{-i\omega_q t}-1\Big)\Big] \qquad \text{(B.2)}
\end{aligned}
$$

where

$$
n_q=\frac{1}{e^{\hbar\beta\omega_q}-1} \qquad \text{(B.3)}
$$

and we recognise the finally form as the discrete form of the electron-phonon propagator (see Mahan).

Appendix C

Full eigenvalues of detuned-3-site-V-system

Here we present the eigenvalue solutions to the Hamiltonian

$$H_3 = \epsilon_1 |1\rangle\langle 1| + \epsilon_2 |2\rangle\langle 2| + \epsilon_0 |0\rangle\langle 0| + \Delta_{10}(|1\rangle\langle 0| + h.c.) + \Delta_{20}(|2\rangle\langle 0| + h.c.) \tag{C.1}$$

where $\epsilon_0 = 0$ is the ground state. This Hamiltonian represents the most general case of the 3-site-V system, with the potential for detuned upper levels $\epsilon_1 \neq \epsilon_2$. We include the solutions here for the bare-3-site-V system primarily to demonstrate the complicated nature of the eigenvalues even without a bath. In the main text we mostly deal with the tuned case $\epsilon_1 = \epsilon_2$. The eigenvalues are calculated to be

$$\begin{aligned}
\lambda_1 &= \frac{\epsilon_1 + \epsilon_2}{3} - \frac{\sqrt[3]{2}}{3N}\Big[(\epsilon_1 + \epsilon_2)^2 + 3\tilde{\Omega}^2 - \epsilon_1\epsilon_2\Big] - \frac{N}{3\sqrt[3]{2}} \\
\lambda_2 &= \frac{\epsilon_1 + \epsilon_2}{3} - \frac{(1 + i\sqrt{3})}{3N}\Big[(\epsilon_1 + \epsilon_2)^2 + 3\tilde{\Omega}^2 - \epsilon_1\epsilon_2\Big] + \frac{(1 - i\sqrt{3})N}{6\sqrt[3]{2}} \\
\lambda_3 &= \frac{\epsilon_1 + \epsilon_2}{3} - \frac{(1 - i\sqrt{3})}{3N}\Big[(\epsilon_1 + \epsilon_2)^2 + 3\tilde{\Omega}^2 - \epsilon_1\epsilon_2\Big] + \frac{(1 + i\sqrt{3})N}{6\sqrt[3]{2}}
\end{aligned} \tag{C.2}$$

where

$$
\begin{aligned}
N = & \Big[-9\Delta_{10}^2\epsilon_1 + 18\Delta_{20}^2\epsilon_1 + 18\Delta_{10}^2\epsilon_2 - 9\Delta_{20}^2\epsilon_2 \\
& + \Big[4\left(-3\left(\Delta_{10}^2 + \Delta_{20}^2 - \epsilon_1\epsilon_2\right) - \left(\epsilon_1 + \epsilon_2\right)^2\right)^3 \\
& + \left(-9\Delta_{10}^2\epsilon_1 + 18\Delta_{20}^2\epsilon_1 + 18\Delta_{10}^2\epsilon_2 - 9\Delta_{20}^2\epsilon_2 - 2\epsilon_1^3 + 3\epsilon_2\epsilon_1^2 + 3\epsilon_2^2\epsilon_1 - 2\epsilon_2^3\right)^2 \Big]^{1/2} \\
& - 2\epsilon_1^3 + 3\epsilon_2\epsilon_1^2 + 3\epsilon_2^2\epsilon_1 - 2\epsilon_2^3 \Big]^{\frac{1}{3}}
\end{aligned} \tag{C.3}
$$

Appendix D

Fluctuation-dissipation theorem

The fluctuation-dissipation theory is a central feature of linear response theory and is applied in the perturbative model in the text. The theorem relates the relaxation of a weakly perturbed system to the thermal fluctuations in the environment i.e. the response of the system to a small applied force is equivalent to the response to a spontaneous fluctuation. The main result of the theory relates the power spectrum $S(\omega)$ of the fluctuations, to the Fourier transform of the susceptibility $\chi(\omega)$ (the linear response function)

$$S(\omega) = \hbar \mathrm{Im}\chi(\omega) \coth(\hbar\beta\omega/2) \tag{D.1}$$

with the random force correlation function given in the time-domain by

$$\langle \xi(t)\xi(0)\rangle = \int_0^\infty d\omega J(\omega)\Big(\coth(\beta\hbar\omega/2) - i\sin(\omega t)\Big) \tag{D.2}$$

and the power spectrum is found to be [61]

$$S(\omega) = J(\omega) \coth(\beta\hbar\omega/2) \tag{D.3}$$

Appendix E

Cubic polynomials

The central problem in this thesis involves investigating a 3-site system interacting with its environment. Intrinsic to this problem in the various areas of the parameter space of interest involves solutions to cubic polynomials which appear as the pole structure of the propagators. Here we detail the general form that these solutions take as a reference for the main section of the thesis. The formalism presented here can be easily checked against those presented in [123, 124, 125]. Consider the equation

$$x^3 + ax^2 + bx + c = 0 \tag{E.1}$$

One solves this equation with the substitution

$$x = t - \frac{a}{3} \tag{E.2}$$

which produces the solvable cubic

$$t^3 + pt + q = 0 \tag{E.3}$$

where

$$p = \frac{3b - a^2}{3} \quad , q = \frac{2a^3 - 9ab + 27c}{27} \tag{E.4}$$

Limiting cases include;

If $q = 0$ then

$$t^3 + pt = 0, \quad t = \pm\sqrt{-p} \tag{E.5}$$

and the original 3-roots are

$$x_1 = -\frac{a}{3}, \quad x_{2,3} = \pm\sqrt{-p} - \frac{a}{3} \tag{E.6}$$

If $p = 0$ then $t = \sqrt[3]{-q}$ and the 3-roots of our original equation are

$$x_1 = \sqrt[3]{-q} - \frac{a}{3}, \quad x_{2,3} = \sqrt[3]{-q}(-\frac{1}{2} \pm \sqrt{3}i/2 - \frac{a}{3} \tag{E.7}$$

Beyond the simple cases outlined above we now present the general solutions. First we must define the discriminant that determines the nature of the roots. The discriminant is

$$D = \left(\frac{q}{2}\right)^2 + \left(\frac{p}{3}\right)^3 \tag{E.8}$$

and the 3-regimes are;

If $D > 0$ then we have one real root and 2-complex conjugate roots and the solutions are

$$x_1 = u - v - \frac{a}{3}, \quad x_{2,3} = -\frac{1}{2}(u - v) \pm (u + v)\frac{\sqrt{3}}{2}i - \frac{a}{3} \tag{E.9}$$

where

$$u = \sqrt[3]{\sqrt{D} - \frac{q}{2}}, \quad v = \sqrt[3]{\sqrt{D} + \frac{q}{2}} \tag{E.10}$$

If $D < 0$ then all 3 roots are real and distinct and the solutions are obtained with the cosine substitution

$$\begin{aligned} x_1 &= 2\sqrt[3]{r}\cos\left(\frac{\phi}{3}\right) - \frac{a}{3} \\ x_2 &= 2\sqrt[3]{r}\cos\left(\frac{(\phi + 2\pi)}{3}\right) - \frac{a}{3} \\ x_3 &= 2\sqrt[3]{r}\cos\left(\frac{(\phi + 4\pi)}{3}\right) - \frac{a}{3} \end{aligned} \tag{E.11}$$

where

$$r = \sqrt{(-\frac{p}{3})^3}, \quad \phi = \arccos\left(\frac{-q}{2r}\right) \tag{E.12}$$

If $D = 0$ then all the roots are real and 2 are equal

$$x_1 = 2\sqrt[3]{-\frac{q}{2}} - \frac{a}{3}$$
$$x_{2,3} = -\sqrt[3]{-\frac{q}{2}} - \frac{a}{3} \tag{E.13}$$

Appendix F

Saddle point integration of optical phonon correlation functions

Here I present the calculation of the correlation function for an optical phonon as required in the text. The influence phase is given by

$$\varphi_{op} = iQ'_{op} + Q''_{op} = \int_0^\infty \frac{d\omega}{\omega^2} e^{-\frac{(\omega-\omega_0)^2}{\xi^2}} \cos(\omega\tau)\mathrm{csch}(\hbar\beta\omega/2) \tag{F.1}$$

This integral is divergent as it stands however the saddle-point approximation can be used to calculate it [136]. This method is valid in the limit of very large exponential arguments, which in this case corresponds to $1/\xi^2 \gg 1$. As ξ represents the full-width-half-maximum (FWHM) of the Guassian peak, this condition applies to a very narrow peak, centred around ω_0. The saddle point method evaluates real integrals of the form

$$I = \int_a^b d\omega e^{-xf(\omega)} g(\omega) \tag{F.2}$$

where x is very large. Another necessary condition for the use of the saddle-point method is for the peak to be symmetrical about its center such that $f(\omega_0) = 0$, which is valid for the Guassian lineshape used here. Expanding about ω_0

$$f(\omega) = f(\omega_0) + \frac{1}{2} f''(\omega_0)(\omega - \omega_0)^2 + ..., \quad g(\omega) = g(\omega_0) + ... \tag{F.3}$$

which inserted in to the integral equation gives

$$I = e^{-xf(\omega_0)} \int_a^b d\omega e^{-\frac{x}{2} f''(\omega_0)(\omega-\omega_0)^2} g(\omega_0) \tag{F.4}$$

Making the change of variables $\omega = \omega_0 + y\sqrt{2/f''(\omega_0)}$ such that

$$I = e^{-xf(\omega_0)}\sqrt{\frac{2}{f''(\omega_0)}}\int_{a'}^{b'} dy e^{-xy^2} g(\omega_0) \tag{F.5}$$

where $a' = (a-\omega_0)\sqrt{f''(\omega_0)/2}$ and correspondingly for b'. The parameter x is very large, so the reparameterised Guassian is also very narrow with center at $y = 0$ this time. This means we can extend the limits to infinity. Thus,

$$I = e^{-xf(\omega_0)}\sqrt{\frac{2}{f''(\omega_0)}}\int_{-\infty}^{\infty} dy e^{-xy^2} g(\omega_0) \tag{F.6}$$

Making a further change of variable $z = \sqrt{x}y$ yields

$$I = e^{-xf(\omega_0)}\sqrt{\frac{2}{xf''(\omega_0)}}\int_{-\infty}^{\infty} dz e^{-z^2} g(\omega_0) \tag{F.7}$$

and the Guassian integral can be performed to give

$$I = e^{-xf(\omega_0)}\sqrt{\frac{2\pi}{xf''(\omega_0)}} g(\omega_0) \tag{F.8}$$

which is the result we use in the text.

Appendix G

Pure dephasing dynamics in the 3-site-V system

I mention briefly in Section 3.4 of the main text how, in the limit of zero tunnelling $\Delta_{10} = \Delta_{20} = \Delta = 0$ (for the 3-site-V system), the system exhibits 'pure dephasing'. This corresponds to no change in the diagonal elements of the density matrix, but a decay in the off-diagonal elements despite the absence of tunnelling between states. This is entirely due to the fluctuating on-site energies induced by the bath, and leads to decoherence in the system without energy dissipation. As this is an exactly solvable model, with just three copies of the well known Independent-boson model, we merely comment on it in the text and do not quote the corresponding calculations for the dynamics. Instead I include them here for reference. The system is easily solved by transforming the Hamiltonian with the Lang-Firsov unitary operator $U = e^S$, where $S = -\sum_{\alpha q} u_{\alpha q}(b_q - b_q^\dagger)\,|\alpha\rangle\langle\alpha|$ and $u_{\alpha q} = \lambda_{\alpha q}/\omega_q$ such that $H \to UHU^\dagger = e^S H e^{-S}$. Physically, this represents the shifting of the boson cloud to its new equilibrium position. So S can be thought of as a shift operator. Here we find (using the Baker-Campbell-Hausdorff formula)

$$UHU^{-1} = \sum_q \omega_q b_q^\dagger b_q - \sum_q u_{\alpha q} \tag{G.1}$$

The dynamics of the coherences are thus

$$\langle P_{\alpha\beta}(t)\rangle = \mathrm{Tr}_B\left[U\rho_s \otimes \rho_B U^{-1} U P_{\alpha\beta} U^{-1}\right] \tag{G.2}$$

where we've assumed an initial spin-bath factorised state and inserted the identity $\mathbb{1} = UU^{-1}$. Defining $\Phi_\alpha = -2i\sum_q u_{\alpha q}(b_q - b_q^\dagger)$ we can apply the BCH formula again to state

$P_{\alpha\beta} = |\alpha\rangle\langle\beta|$ to evaluate

$$\begin{aligned} UP_{\alpha\beta}U^{-1} &= |\alpha\rangle\langle\beta| + \left[-i\sum_{\alpha}|\alpha\rangle\langle\alpha|\,\frac{\Phi_\alpha}{2}, |\alpha\rangle\langle\beta|\right] + ... \\ &= |\alpha\rangle\langle\beta|\left(1 + i(\Phi_\beta/2 - \Phi_\alpha/2) + ...\right) \end{aligned} \tag{G.3}$$

eventually one finds (including the biases now)

$$\begin{aligned} \langle P_{\alpha\beta}(t)\rangle &= \text{Re } e^{-i(\epsilon_\alpha - \epsilon_\beta)}e^{-Q''(t)} \\ Q''_{\alpha\beta}(t) &= \int d\omega \frac{|J_\alpha(\omega) - J_\beta(\omega)|}{\omega^2}(1 - \cos(\omega t))\coth\left(\frac{\beta\omega}{2}\right) \end{aligned} \tag{G.4}$$

where we're interested in the probability of occupancy of the off-diagonal states and so inspect the real part. We see that the bath correlation term above corresponds to the real part of the reparameterised Feynamn-Vernon influence function as discussed in the introduction. It is indeed this term that is responsible for dephasing owing to the self-interaction of the off-diagonal paths in the density matrix. The coherences are exponentially damped in this regime with the rate depending on the difference of the spectral densities corresponding to the states constituting the coherent superposition. The bath correlation function Q'' determines the rate $\Gamma_\varphi^{\alpha\beta}$, which is the pure dephasing rate: the rate at which the off-diagonal elements are suppressed without relaxation effects due to tunnelling processes. When tunnelling processes are included, the decay of the off-diagonal density matrix elements will include a combination of the pure dephasing rate and relaxation rate. For now however, without tunnelling included, the decoherence rate is equivalent to the dephasing rate.

The spectral densities are unspecified in the above but generally there will be some dependence of the coupling on the position of the wells. Since the dephasing rate is evidently dependent on the difference between spectral densities, it will also depend on the well separation and as this increases the dephasing rate does accordingly. This makes sense physically as for larger well separation we expect the overlap between wavefunctions to decrease and coherences to become less pronounced.

For the Ohmic case (s=1) we have for the spectral density $J_\alpha(\omega) = \eta_\alpha \omega e^{\omega/\omega_c}$ such that the frequency integral can be formed in the bath correlation function to get

$$Q''_{\alpha\beta}(t) = \frac{1}{2}\gamma_{\alpha\beta}\ln(1+\omega_c^2 t^2) + \gamma_{\alpha\beta}\ln\left[\frac{\beta}{\pi t}\sinh\left(\frac{\pi t}{\beta}\right)\right] \tag{G.5}$$

where $\gamma_{\alpha\beta} = (\eta_\alpha - \eta_\beta)^2/\pi\hbar$. In the various limits we find for the dynamics

$$|\langle P_{\alpha\beta}(t)\rangle| = \frac{1}{[1+(\omega_c t)^2]^{\gamma_{\alpha\beta}/2}}, \quad T = 0K \tag{G.6}$$

where for short times below the characteristic time-scale of the bath

$$|\langle P_{\alpha\beta}(t)\rangle| = 1 - \gamma_{\alpha\beta}\frac{(\omega_c t)^2}{2}, \quad \forall\ \omega_c t \ll 1, T = 0K \tag{G.7}$$

For intermediate times we observe the power-law governed dephasing

$$|\langle P_{\alpha\beta}(t)\rangle| = (\omega_c t)^{-\gamma_{\alpha\beta}} \quad \forall\ 1/\omega_c \ll t, T = 0K \tag{G.8}$$

So we see that at zero temperature we still have dephasing but at a slower than exponential rate; instead the off-diagonal elements decay algebraically. Recall that when $\gamma_\alpha = \gamma_\beta$ the bath decouples from the central system and we expect the decoherence rate in this case to go to zero. When we include non-zero temperatures

$$|\langle P_{\alpha\beta}(t)\rangle| = \frac{[(\hbar\beta/\pi t)\sinh(\pi t/\hbar\beta)]^{-\gamma_{\alpha\beta}}}{[1+(\omega_c t)^2]^{\gamma_{\alpha\beta}/2}} \tag{G.9}$$

We can once again inspect for short times. First we look at the low-T case where we expand in the dimensionless quantity $\pi t/\hbar\beta << 1$, which essentially defines the limit of small bath fluctuations relative to tunnelling energy i.e. for $t \sim 1/\Delta,\ k_B T/\hbar\Delta \ll 1$

$$\begin{aligned}
|\langle P_{\alpha\beta}(t)\rangle| &= \left[\frac{1}{[1+(\omega_c t)^2]^{\gamma_{\alpha\beta}/2}}\right]\left[\left(\frac{\pi t}{\hbar\beta}\right)^{-\gamma_{\alpha\beta}-1} - \frac{\gamma_{\alpha\beta}}{6}\left(\frac{\pi t}{\hbar\beta}\right)^{-\gamma_{\alpha\beta}+1}\right],\ \forall\ \pi t/\hbar\beta \ll 1 \\
|\langle P_{\alpha\beta}(t)\rangle| &= \left[\frac{1}{[1+(\omega_c t)^2]^{\gamma_{\alpha\beta}/2}}\right]\left(\frac{\pi t}{2\hbar\beta}\right)\exp(-\gamma_{\alpha\beta}\pi t/\hbar\beta),\ \forall\ \pi t/\hbar\beta \gg 1
\end{aligned} \tag{G.10}$$

For the super-Ohmic case (s=3) we have for the spectral density $J_\alpha(\omega) = \rho_\alpha(\omega^3/\omega_c^2)e^{\omega/\omega_c}$. Calculating the bath-correlator

$$\tilde{Q}''_{ph}(t) = \int_0^\infty d\omega\,\omega e^{-\omega/\omega_c}[1-\cos(\omega t)]\coth(\hbar\beta\omega/2) \tag{G.11}$$

we find for the zero-temperature case

$$\tilde{Q}''_{ph}(t) = \frac{\omega_c^2(\omega_c t)^2\Big[3+(\omega_c t)^2\Big]}{\Big[1+(\omega_c t)^2\Big]^2} \quad \text{for} \quad T = 0K \tag{G.12}$$

For short and long times respectively (to 2nd-order in the respective small parameters)

$$\begin{aligned}
\tilde{Q}''_{ph}(t) &= 3\omega_c^4 t^2 \quad \text{for } \forall\ T = 0K, \omega_c t \ll 1 \\
\tilde{Q}''_{ph}(t) &= \omega_c^2\left(\frac{1+(\omega_c t)^2}{(\omega_c t)^2}\right)\ \forall\ T = 0K, \omega_c t \gg 1
\end{aligned} \tag{G.13}$$

For non-zero temperatures we get a temperature dependent correction and the integral is computed to be

$$\tilde{Q}''_{ph}(t) = -\frac{\omega_c^2(\omega_c t)^2\Big[3+(\omega_c t)^2\Big]}{\Big[1+(\omega_c t)^2\Big]^2} - \frac{1}{4(\hbar\beta)^2}\left[2\psi'(1/\omega_c\hbar\beta) - \psi'\left(\frac{1-i\omega_c t}{\hbar\omega_c\beta}\right) - \psi'\left(\frac{1+i\omega_c t}{\hbar\omega_c\beta}\right)\right] \tag{G.14}$$

which still contains the small parameter $\omega_c\hbar\beta \gg 1$ intrinsic to the continuous-discrete system truncation procedure and would be inconsistent to relax it now. We find

$$\tilde{Q}''_{ph}(t) = \frac{\omega_c^2(\omega_c t)^2\Big[3+(\omega_c t)^2\Big]}{\Big[1+(\omega_c t)^2\Big]^2} + \frac{\pi^4 t^2\Big[1+(\omega_c t)^2\Big]^2}{240(\hbar\beta)^4\Big[1+(\omega_c t)^2\Big]^2} \tag{G.15}$$

We can explore the same limiting time-domains as before

$$\begin{aligned}
\tilde{Q}''_{ph}(t) &= 3\omega_c^4 t^2 + \frac{\pi^4 t^2}{240(\hbar\beta)^4} \quad \text{for } \forall\ \hbar\Delta/k_B T \gg 1, \omega_c t \ll 1 \\
\tilde{Q}''_{ph}(t) &= \omega_c^2\left(\frac{1+(\omega_c t)^2}{(\omega_c t)^2}\right) + \frac{\pi^4 t^2}{240(\hbar\beta)^4}\ \forall\ \hbar\Delta/k_B T \ll 1, \omega_c t \gg 1
\end{aligned} \tag{G.16}$$

where in both cases we obtain a temperature dependent correction that goes as T^4. So for the case of short times and low temperatures, the loss of coherence is algebraic in time

$$|\langle P_{\alpha\beta}(t)\rangle| \sim 1 - 3\gamma_{\alpha\beta}\omega_c^4 t^2 - \frac{\pi^4 \gamma_{\alpha\beta} t^2}{(\hbar\beta)^4} \tag{G.17}$$

and for long times and/or high temperatures, the loss of coherence is of course exponential in time.